Spring 2016

Automatic construction of arterial and venous vascular trees in fundus images

Qiao Hu
University of Iowa

AUTOMATIC CONSTRUCTION OF ARTERIAL AND VENOUS VASCULAR TREES IN FUNDUS IMAGES

by

Qiao Hu

A thesis submitted in partial fulfillment of the
requirements for the Doctor of Philosophy
degree in Electrical and Computer Engineering
in the Graduate College of
The University of Iowa

May 2016

Thesis Supervisors: Professor Michael D. Abràmoff
Associate Professor Mona K. Garvin

Graduate College
The University of Iowa
Iowa City, Iowa

CERTIFICATE OF APPROVAL

PH.D. THESIS

This is to certify that the Ph.D. thesis of

Qiao Hu

has been approved by the Examining Committee for the thesis requirement for the Doctor of Philosophy degree in Electrical and Computer Engineering at the May 2016 graduation.

Thesis Committee: _____
Michael Abràmoff, Thesis Supervisor

_____
Mona K. Garvin, Thesis Supervisor

_____
Joseph M. Reinhardt

_____
Todd E. Scheetz

_____
Xiaodong Wu

ACKNOWLEDGEMENTS

First of all, I would like to thank my advisors, Dr. Michael D. Abràmoff and Dr. Mona K. Garvin for their continuous support throughout my PhD study. I could not have come this far without either of their guidance. Dr. Michael Abràmoff is a great mentor who is always full of passion in his research area. He encouraged me to ask questions and to express myself. Dr. Mona Garvin has been a great advisor by always inspiring me with brilliant ideas in my research. She is always there to listen and to give advice. Her encouragement makes me feel more confident in my study.

I would like to thank the other committee members: Dr. Joseph M. Reinhardt, Dr. Todd E. Scheetz, and Dr. Xiaodong Wu for their advices on the thesis. Also thanks to Dr. Meindert Niemeijer for all the help and for always sharing his inspiring papers. Also I would like to thank all my colleagues who helped me along this road and gave me advice: Dr. Li Tang, Dr. Xiayu Xu, Dr. Mark Christopher, Dr. Bhavna Anothny, Dr. Nazli Demirkaya and Yiyue Lou. I also would like to thank to Mark for developing the iPad version of truthMarker, which facilitates the ground truth making, and in turn makes my research easier. Many thanks to my lab mates and friends who helped me, Dr. Junjie Bai, Dr. Jui-kai Wang, Dr. Saleh Miri, Dr. Yunlong Liu, Dr. Qi Song, and Dr. Kunlin Cao.

My sincere thanks goes to the department secretaries Cathy and Dina for their kind help during all the past years.

Finally, last but not least, I would like to extend a special thanks to my parents,

my family and all my friends.

This work is partially supported by the National Eye Institute (R01 EY018853), and the Department for Veterans Affairs (I01 CX000119 and Career Development Award IK2RX000728).

ABSTRACT

The retinal vasculature analysis plays an important role in the diagnosis of ophthalmological diseases, as well as general human disorders that manifest on the retina. The fundus photograph is a 2-D color image modality of the retina and is widely used in modern ophthalmology clinics due to its relatively low cost and its non-invasive access to the retina. However, due to the complexity of the retinal vasculature presented on the image and the large variation of the image quality, no automated method is able to re-construct the retinal vasculature (i.e. construct arteriovenous trees) satisfactorily, thus preventing its analysis on large-scale clinical datasets.

In this thesis, we present a systematic and complete study to automatically construct the retinal vasculature on fundus photographs and apply it to a clinical dataset. First of all, a preliminary study is conducted to detect and classify important landmarks in the retinal vasculature using a machine learning method. The evaluation of this method reveals the difficulty of identifying each landmark as an independent target. Then a novel and more global method is proposed to construct retinal arteriovenous trees (A/V trees). The strategy of the proposed method is to build an over-connected vessel network, and separate it into vascular trees, then classify them into A/V trees. Particularly, by taking advantages of specific properties of the retinal vasculature, global and local information are combined together to recognize landmarks of the vasculature. Instead of recognizing each landmark independently as other methods do, this method considers the relationship between

landmarks in a more global manner, thus recognizing them simultaneously and globally. With a special graph design, each landmark is associated with multiple possible configurations and costs, and a near optimal solution is selected by minimizing the costs of landmarks and the global property of the whole vascular network. With each landmark recognized, the A/V trees are easily inferred with a pixel classification method. By doing so, local noise in the images and local errors during pre-processing are corrected to some degree, and small vessels that are difficult to classify locally can also be recognized. The proposed method is compared with another method and the evaluation demonstrates its superiority.

To demonstrate its potential applicability, we apply the proposed method on a cohort study data of HIV-infected patients with treatment. New metrics to analyze retinal vessel width is developed based on the A/V trees built using the proposed method, and it is compared with a conventional metric. Statistical analysis reveals the advantages of the new metric and thus indicates the benefit of the proposed method and its potential application on large datasets.

PUBLIC ABSTRACT

The retinal vasculature is an important target in ophthalmology clinics because it provides insight to many ophthalmologic diseases, as well as general disorders that manifest on the retina. The fundus photograph is a 2-D color image modality of the retina and is widely used in modern ophthalmology clinics due to its relatively low cost and its non-invasive access to the retina. The analysis of the retinal vasculature is time-consuming and demands effort of human experts. Thus with limited human resources, the largely increasing clinical data collected from patients demands the automation of the analysis. However, due to the complexity of the vasculature presented on the image and the variation of the image quality, no automated method is able to re-construct arteriovenous trees satisfactorily, which is the most important step of the automatic analysis.

In this work, we conduct a systematic and complete study to automatically construct retinal arteriovenous trees (A/V trees) in fundus photographs. It requires the classification of vessels into arteries and veins, and also the detection of connections between vessels. First of all, a conventional method is conducted to automatically detect and classify an important type of structure, bifurcations in the vasculature. The result reveals the difficulty of constructing A/V trees by identifying each bifurcation independently. Then a novel and more global method is proposed. The strategy of the proposed method is to build an over-connected vessel network, separate it into vascular trees, and then classify them into A/V trees. Particularly, by

taking advantages of properties of the retinal vasculature, global and local information of retinal vessels are combined together to recognize landmarks of the vasculature. Instead of recognizing each landmark independently as conventional methods do, we consider relation between landmarks, and recognize them simultaneously and globally. After landmarks are recognized, the types of trees can be easily inferred and A/V trees are constructed. A comparison is made between the proposed method and another method and the evaluation shows its merits.

In addition, to demonstrate its applicability, we use it to analyze the changes of vessel width on HIV-infected patients under highly active antiretroviral therapy (HAART). With A/V trees constructed using the proposed method, vessel widths are analyzed using a novel method. The vessel widths calculated using the new method are compared with vessel widths calculated using a conventional method. The comparison reveals the advantages of this new method, thus indicating the potential applicability of the proposed A/V tree construction method.

TABLE OF CONTENTS

LIST OF TABLES

Table

LIST OF FIGURES

Figure

LIST OF ALGORITHMS

Algorithm

CHAPTER 1
INTRODUCTION

A color fundus photograph is a widely-used image modality in ophthalmologic clinics, which is used for the diagnosis of retinal diseases, and other ophthalmologic diseases and disorders, and some general disorders with symptoms reflected on the retina. Recently, with the increasing popularity and demands of computer-aided diagnosis (CAD), the application of such technologies on the fundus photographs has become an interesting topic. One of the key issues and important tasks is to automatically construct the arterial and venous vascular trees (A/V trees) on retinal photographs. As one of the most important and visible structures, the vascular trees reveals information about retinopathies and the health status of the human body. It also proves to be a reliable and important landmark for the detection of other structures like the optic disc and the macula, and for other image-processing tasks such as image registration and mosaicing. However due to the structural complexity of vascular trees, the automatic construction of A/V trees proves to be a very difficult task and so far there is no satisfying method. Hence in this work, a rigorous study is conducted to develop a method to automatically detect the arterial and venous trees in retinal photographs and explore its potential application.

1.1 Specific Aims

Due to the complexity of this problem, three specific aims are desgined to solve one aspect of the problem, as following:

- Aim 1: To develop and evaluate an automatic approach for the detection and localization of retinal vessel branches using a vision-machine approach.
- Aim 2: To develop and formulate a framework to solve the binary overlapping trees problem using a graph-based model, and to apply it to construct A/V trees in fundus photographs.
- Aim 3: Based on Aim 2, given the constructed A/V trees in fundus photographs, to develop metrics to measure and analyze the width of retinal vessels in a clinical dataset.

1.2 Thesis Overview

According to the aims proposed above and the work conducted, this thesis is divided into 7 chapters, each of which describes a specific aspect of the problem. Besides this chapter as Introduction, the rest is organized as following:

- Chapter 2 provides detailed background information of the entire work, including a clinical background review and a technical background review. The clinical background reviews the human eye structure, the fundus photographs, and diseases related to the retinal vasculature. The technical background reviews related image analysis technologies including the vessel segmentation, the determination of vessel connectivity, the classification of arteries and veins, and the retinal vasculature analysis.
- Chapter 3 presents a developed automatic approach of retinal vessel branch detection and localization using a vision-machine approach.

- Chapter 4 presents a developed framework to solve the binary overlapping tree problem using a special graph-based model and the application of it to construct A/V trees in fundus photographs.
- Chapter 5 presents a developed method to measure and analyze the width of A/V trees and the application of it on clinical pathological analysis.
- Chapter 6 discuss the merits and issues of the work, and also potential work for future.
- Chapter 7 summarizes and concludes the thesis.

CHAPTER 2
BACKGROUND AND LITERATURE REVIEW

2.1 Clinical Background

2.1.1 The Anatomy of Human Eye

The human eye is the visual sense organ sensitive to light and transforming it into an electrical signal. Figure 2.1 shows the brief anatomical inner structure of the eye. Anatomically the human eye is made of three layers, enclosing three transparent structures [5]. The outermost layer is composed of the cornea and sclera. The middle layer consists of the choroid, ciliary body, and iris. The innermost is the retina, which obtains its circulation from the vessels of the choroid as well as the retinal vessels, which can be seen in an ophthalmoscope, or in fundus images. Bound by these layers are the aqueous humor, the crystalline lens and the vitreous body [6].

The cornea is transparent to light and contains no blood vessels and its primary function is to transmit and focus light into to the eye. Located at the front of the eye, it is approximately 11 mm in diameter and 500 μm thick in the center, thickening to around 700 μm at the periphery [7].

The fluid that fills the anterior chamber of the eye, the area between the cornea and the front surface of the crystalline lens, is called the aqueous humor, or aqueous. Besides being part of the optical pathway of the eye, aqueous provides nutrients to the cornea and the crystalline lens. The iris is visible through the cornea and defines the "color" of the eye. The main function of the iris is to block excess light from

entering the eye. The amount of light entering the eye is controlled by the aperture of the iris or "pupil". Like the cornea, the crystalline lens is a transparent structure. It is suspended from the ciliary body by the suspensory ligament (Zonule of Zinn), made up of fine transparent fibers. Unlike the cornea, it has the ability to change its shape in order to increase or decrease the amount of refracting power applied to light coming into the eye.

Between the lens and the retina is the vitreous, also called the vitreous body or vitreous humor, which is a transparent and gelatinous material, serving to provide for light transmission through the eye and to protect the retina. About 98 - 99% of the vitreous volume is water and it contains very few cells, and no blood vessels [7].

The retina is a light sensitive tissue layer lining the interior of the posterior portion of the globe. The photosensitive cells on the retina detect light passing through the cornea and the lens. The fovea centralis (as shown in Figure 2.1), usually known as the fovea, is located in the center of the macular region on the retina, which is responsible for the sharp central vision. Approximately 50% of the nerve fibers in the optic nerve carry information from the fovea [8]. The optic disc or optic nerve head is where ganglion cell axons exit the eye. It is usually placed $3 - 4$ mm to the nasal side of the fovea [8]. The optic nerve is a bundle of more than one million nerve fibers which connect the retina to the brain. It is also the place where all retinal blood vessels originate and converge. Although it is commonly referred as arteries and veins in the retina, the vascular tree of the retina actually consists of arterioles and venules. This is because the widest part of the lumen of the retinal vessels is near

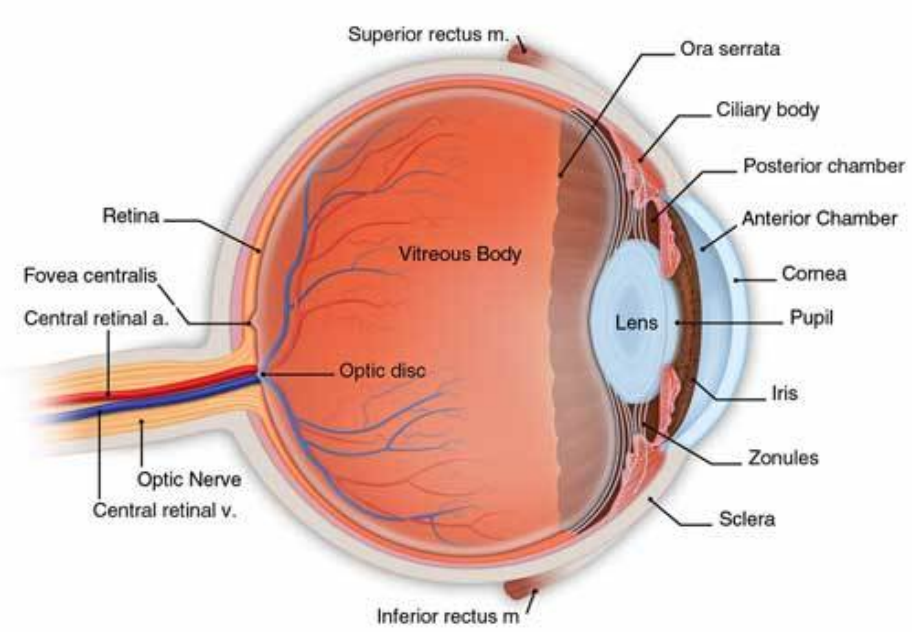

Figure 2.1: A simple illustration of eye anatomy (image courtesy of reference [1].

the optic disc with diameters of about 100 μm, with neither internal elastic lamina nor a continuous muscular coat.

The mechanism of how the human eye captures the light and transfers to electrical signal into brain is illustrated in Figure 2.2. Light entering the eye is first refracted when it pases through the cornea. It then passes through the pupil and is further refracted by the lens. Finally it reaches the retina and is converted to electrical signals by photosensitive photoreceptor in the retina. These signals are then transmitted to the brain along the optic nerve, and processed by the brain to form vision.

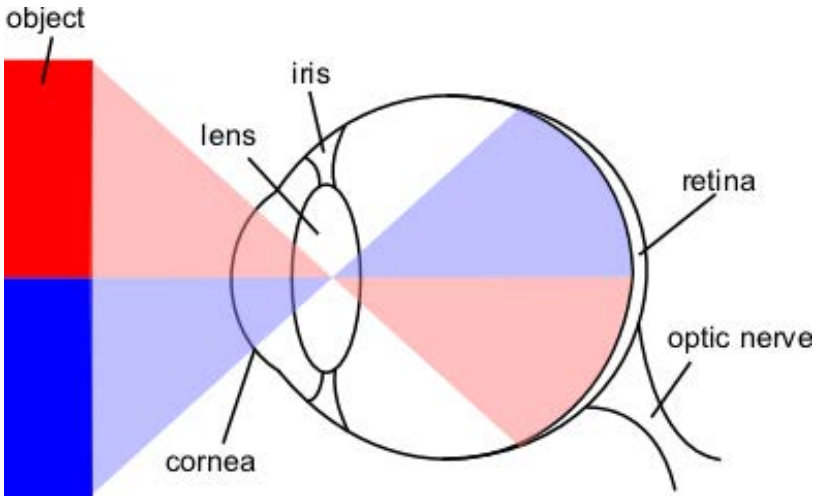

Figure 2.2: A Light path of the visual system (image courtesy of reference [2]).

2.1.2 Fundus Photography

The fundus of the eye is the interior surface of the eye, including the retina, optic disc, macula and fovea. A fundus photograph is a photograph of the fundus taken by an ophthalmoscope, or a fundus camera. The following is quoted from a review by Abramoff *et al* [9]. The first manually drawn picture of the fundus was done by the Dutch ophthalmologist van Trigt in 1853 [10]. Later photographic images of the retina which showed the blood vessels were obtained in 1891 by the German ophthalmologist Gerloff [11]. The first fundus camera was developed by Gullstrand in 1910, and the concept behind is still used to image the retina today [12].

An example of a human fundus photograph is shown in Figure 2.3(b). A typical human fundus photograph usually appears reddish. Three major structures are present in a normal human eye fundus photograph: the optic disc (or optic nerve head), the macula and blood vessels. The optic disc appears to be a bright circu-

lar region in the image, where all blood vessels appear to converge. Blood vessels are commonly darker than the retina background, but arteries are usually brighter compared to veins. The macula is a dark region where few blood vessels are present. Ophthalmologists can diagnose retinopathies by examining a presence of abnormalities of the retina on the fundus photographs such as hemorrhages, exudates, cotton wool spots, blood vessel abnormalities, and pigmentation and so forth.

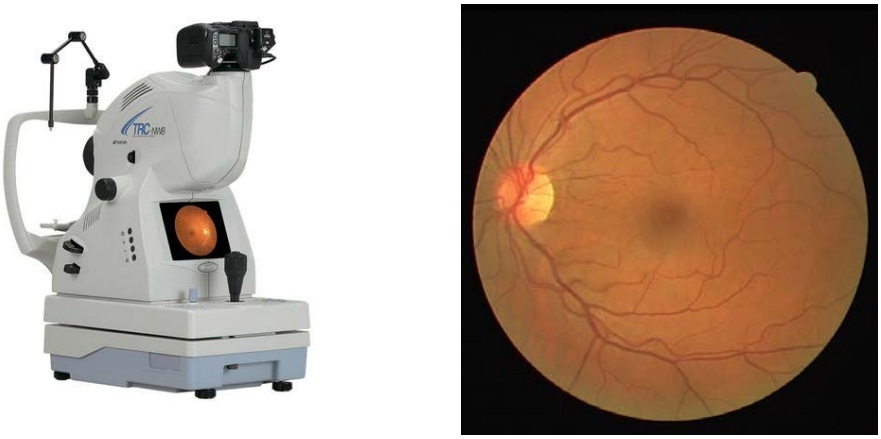

(a) (b)

Figure 2.3: Examples of a fundus camera and a fundus photograph. (a) A fundus camera (figure from reference [3]). (b) A typical fundus photograph (from DRIVE dataset [4]).

Because of its safety and cost-effectiveness at documenting retinal abnormalities, fundus photograph has been the primary image modality for the retina clinically. It is commonly used in screening programs, where the photos can be analyzed later for

diagnosis and/or to monitor the progress for many diseases. However, in a screening program, where thousands of fundus photographs are taken, it is difficult for the ophthalmologists to personally exam every photo, especially in the extremely laborious work to measure and to collect data for every structures in the image. Automated diagnosis thus is introduced to partially relieve the problem by semi-automatically or automatically detecting retinal structures, and certain diseases [13].

2.1.3 Diseases Related with Retinal Vascular Changes

As one of the most important structures in the human eye and part of human circulation, not only does the retinal vasculature reveal retinopathies, but it also indicates some general diseases and the healthy state of human beings. It has been reported that the changes in the retinal vasculature are associated with different types of diseases, disorders and abnormalities.

One type of disease associated with changes in the retinal vasculature is diabetes mellitus and its complications in the retina. According to the current definition from the World Health Organization, diabetes mellitus is typically diagnosed if a patient has a fasting plasma glucose over 7.0 mmol/L [14]. Diabetes is a prevalent disease in US. The number of patients with diabetes in the U.S. is increasing rapidly and reached 25.8 million in 2010[15]. One direct complication of diabetes mellitus is diabetic retinopathy (DR), which is the second most common cause of blindness and visual loss in the US, and the most important cause in the working age population [9]. It is an ocular manifestation of diabetes which affects up to 80 percent of all patients

who have had diabetes for 10 years or more [16].

DR is a progressive disease which can be broadly classified into two types depending on the stage of the progression and their manifestations. One is non-proliferative diabetic retinopathy (NPDR), which happens at the early stage of DR, and another is proliferative diabetic retinopathy (PDR), which is the most advanced stage of DR. NPDR develops as a result of damages to the blood vessels in the retina, which may leak fluid or blood, causing the retina to swell and/or form deposits. PDR is caused by ischemia that results in the growth of new and abnormal blood vessels that may subsequently bleed and/or cause retinal detachment. Besides, at any time during the progression of DR, diabetic macular edema (DME) may happen, which is a complication involving the retinal thickening in the macular area [17]. It occurs after the breakdown of the blood-retinal barrier due to the leakage of dilated hyperpermeable capillaries and microaneurysms.

There is abundant evidence that blindness and visual loss caused by DR can be prevented or reduced through annual screening and early diagnosis [18, 19]. The changes of the retina have been used to determine the severity of DR and a common guideline is used to grade the progression of DR [20, 21, 22] . Microaneurysms are the sign of a early onset of NPDR, and intraretinal hemorrhages and prominent intraretinal microvascular anomalies are the sign of severe NPDR. Neovascularization and vitreous or preretinal hemorrhage are the signs of PDR.

Studies show that retinal vascular changes may precede the subsequent development of overt diabetes, and thus could be used to diagnose pre-diabetes or predict

diabetes [23]. This is essential not just because of the importance of early diagnosis, but also because approximately 30% of people with diabetes in US, or 6.2 million people, are undiagnosed [24]. Studies show that smaller arteriolar caliber, or wider retinal venular caliber is a marker of chronic hyperglycemia and the pre-diabetes state and reflects the early microvascular changes that occur in the development of diabetes [25, 26, 27].

Another type of related diseases are cardiovascular diseases (CVDs) and their manifestations in the eye. CVDs are the most prevalent and most deadly diseases which remain one of the leading causes of death in the world and in the US. 17 million people died due to CVDs worldwide in 2008 [28], and the 2008 overall death rate from CVDs in the US was 244.8 per 100 000 people [29]. Cardiovascular disease manifests itself in the retina in a number of ways. It has been reported that the changes in retinal vasculature is associated with several types of CVDs and their risk factors [30, 31, 32, 33, 34]. Thinning of the arteries and widening of the veins, is associated with an increased risk of stroke [35, 36], myocardial infarction [37, 38], and carotid artery disease [39], thus may be used as markers of early subclinical cardiovascular disease.

As an important risk factor for coronary heart disease and the single most important risk factor for stroke, hypertension is associated with many changes of the retinal vasculature. Substantial evidence shows a strong association between the naorrowing of retinal arterioles and hypertension [33, 34, 37, 40, 41, 42]. In addition, an increase in the retinal arteriolar length-to-diameter ratio [43, 44], increased retinal

venular tortuosity [43], reduced branching angle at arteriole bifurcations [45], and reduced microvascular density [43, 45, 46], have been associated with hypertension. Moreover, the retinal arteriolar narrowing is associated with hypertensive retinopathy, which is referred as the pathophysiological changes in retinal vessels in response to blood pressure elevation. On the other hand, although less is known about the pathophysiological mechanisms of retinal venular caliber changes, epidemiological studies have consistently shown associations of retinal venular caliber with systemic inflammatory markers [47]. Besides, retinal venular widening is reported to be associated with risk factors including smoking, hyperglycemia, obesity, and dyslipidemia [32]. In addition, systemic vascular disease can cause arterial and venous occlusions, known as central and branch arterial occlusions (CRAO, BRAO) and central and branch venous occlusions (CRVA, BRVO) [9].

Recently, research has been conducted to study the relation between changes in the retinal vasculature and HIV-infected people. HIV is short for human immunodeficiency virus and is a significant epidemic that threatens the human race. Globally 35 million people were living with HIV and 1.6 million died from AIDS in 2012 [48]. So far there is no cure and the most common treatment to suppress HIV is the highly active anti-retroviral therapy (HAART) [49], also as known as combination anti-retroviral therapy (cART). Successful HAART can decrease the HIV burden, maintain the function of the immune system and largely suppress the incidence of opportunistic infections. However, because HAART does not restore the immune system and has cumulative toxic effects, there is a trend that HIV-infection is trans-

formed from a fatal disease into a chronic condition [50]. A series of non-AIDS related disorders are merged in HIV patients who are well-treated, including cardiovascular disease [51, 52], kidney disease [53, 54], liver disease [55], malignancy [56, 57]. As part of the micro-circulation, the retinal vasculature provides an access to examine and monitor changes and conditions related to the circulation, which can reflect physiological and metabolic changes of HIV patients. Recent studies have shown that the retinal vasculature changes as a result of HIV infection, as well as HAART treatment [58, 59], including arteriolar and venular vessel widths, the branching angle and vascular tortuosity [60, 61]. However, some of findings are inconclusive, and the cause of these changes is not established currently.

2.2 Technical Background

A lot of research has been dedicated to the segmentation of the retinal vasculature in fundus images. However, compared to the extensive study of vessel segmentation, the construction of arterial and venous vasculature in fundus images is still a difficult problem yet to be tackled. Although much of the related work has been done in recent years, most of it is only focused on partial solutions of the problem. In this section, we review the previous contributions in the area of constructing the vasculature anatomical trees in retinal images. The application of the A/V tree construction in clinics is also reviewed as the demonstration of the benefits and demands of this technology.

To better understand these related works, we review previous works by groups

based on their applications, which are the vessel segmentation, the recognition of landmarks (the determination of vessel connectivity), the distinguishing of arteries and veins, and the retinal vasculature analysis. The first three parts are related with each other and compose the problem of constructing anatomical vasculature. The vessel segmentation is the basic procedure and can be considered as the pre-processing of the other two applications. The distinguishing of arteries and veins and the recognition of landmarks are related to each other in a way that their results are mutually affected, and they can be considered as post-processing of the vessel segmentation. The last part is the application of the first three technologies, which is to analyze the retinal vasculature with some metrics and to examine, monitor, and diagnosis disease.

However, compared to the problem of vessel segmentation, the problems of recognizing landmarks and differentiating arteries and veins are more difficult and they can be viewed as a single problem in essence that is to construct the arterial and venous vascular trees. First because of the loss of information during the projection of 3-D structure of retinal vasculature onto 2-D fundus image, some bifurcations and cross points are not easily recognizable, especially when two vessels partially overlap with each other. Secondly, due to the imperfection of imaging, some segments of vessels are not present in the image, which would change the structures of the vasculature. This problem is also hardened by the current segmentation techniques which cannot render 100 percent accuracy on vessel segmentation. It means that false positives and false negatives would be generated, which would change the topology

of the retinal vasculature.

The following sections are the detail summary and review of methods in these four problems.

2.2.1 Vessel Segmentation

Vessel segmentation is generally considered the first step to construct the anatomical vasculature tree. It separates the target of vessel pixels from the background, which is essential for the construction of anatomical trees. Here we are reviewing these methods which only consider the separation of vessels pixels from non-vessel pixels. Some other similar methods which explicitly recognize arterial vessels and venous vessels from the background are reviewed in 2.2.3.

A large number of approaches have been developed to segment retinal vessels. To better review these different methods, we divide them into two broad categories, based on whether the machine learning strategy of pixel classification is adopted or not (whether a classifier is implemented or not): one is the pixel-based processing method; another is a broad group of methods called rule-based methods, which include vessel tracking approaches, mathematical morphology, matched filtering, model-based locally adaptive thresholding and deformable models, or the combination of multiple methods.

The pixel-based processing approach works by labeling every image pixel as vessel or non-vessel. Among these approaches, a number of them use adaptive filtering or unsupervised method to segment the vessels. Bhuiyan *et al.* [62] developed an

unsupervised classification method to segment vessels. First, the input color image is converted from RGB into a perceptually uniform color space. Second, texture features are extracted after contrast enhancement in the four channels selected from different color spaces. Finally, the Fuzzy C-means clustering algorithm is applied to classify the obtained feature vectors, associated with each image pixel, into vessels and background. In the method presented in [63], blood vessel-like objects were extracted by using the Laplacian operator and noisy objects were pruned according to centerlines, detected using the normalized gradient vector field.

However, as machine learning algorithms or supervised methods gain increasing popularity in computer vision fields recently, more methods are developed using the supervised methods to classify vessel pixels with different feature extraction approaches [64, 65, 4, 66, 67, 68, 69, 70, 71]. Image pixels are represented by a set of specific features and a classifier is trained using manually labeled data and used to classify vessels. Here we are reviewing supervised classification methods which combine different classifiers with different feature extraction strategies. The machine learning methods can achieve very high accuracy and they usually can detect very small vessels, under the circumstances that the features and the classifiers are well-chosen. Some of the current supervised methods can achieve very high area under the curve (AUC) of Receiver operating characteristic (ROC), but there are some drawbacks. Because they use local features to represent vessel pixels, pixels near some landmarks (i.e. bifurcations and crossing points) might be missed since they have a different appearance from normal vessel pixels. Also some discontinuity or in-

consistency would happen at some vessel pixels whose vessel features are not strong. Another drawback is that they can spend much time on classifying background pixels, which are definitely not vessel pixels.

One early pixel-based method was proposed by Gardner *et al.* [64], using a back propagation multilayer neural network (NN) for the vessel segmentation. After histogram equalization, smoothing and edge detection, the image was divided into 20 $\times$ 20 pixel squares (400 input neurons). The NN was then fed with the values of these pixel windows for classifying each pixel as vessel or non-vessel. Sinthanayothin *et al.* [65] also used a multilayer perceptron NN. Each pixel in the image was classified by using the first principal component, and the edge strength values from a 10 $\times$ 10 pixel sub-image centered on the pixel under evaluation, as input data. Diego Marin *et al.* [71] also developed an approach using a multilayer NN classifier with a 7-D feature vector, composed of gray-level-based features and moment invariants-based features. Gray-level-based features describe the intensity information of a target pixel compared to its neighbors and moment invariants-based features capture the linear shape invariant to translation, rotation and scale.

Niemeijer *et al.* [4] segmented vessels using a K-nearest neighbor (kNN) classifier with a 31-D feature vector. The feature vector was constructed with the Gaussian filter and its derivatives up to order 2 at 5 different scales, augmented with the gray-level from the green channel of the original image. Staal *et al.* [66] proposed a supervised ridge-based vessel segmentation method with a kNN classifier. Their method is based on the assumption that vessels are elongated structures. Ridges were extracted

from the image and used as primitives to form line elements. Each pixel was then assigned to its nearest line element so that the image is partitioned into patches. For every pixel, 27 features were firstly computed and sequential forward feature selection was applied to select the most distinguishing features which yielded the best result.

Soares *et al.* [67] proposed to use the Bayesian classifier with the Gaussian mixture model, trained based on features consisting of multi-scale Gabor wavelet transform responses and pixel intensity. Specifically, the gray-level of the inverted green channel and the maximum Gabor transform response over angles at four different scales were considered as pixel features. They used the expectation maximization (EM) algorithm to train the the Bayesian classifier.

Sofka *et al.* [68] developed a strategy to extract a 6-D feature vector to represent vessels by measuring the strength and confidence of vessels and edges derived from multi-scale matched filters. Then they used the likelihood ratio test based on Neyman-Pearson Lemma as the classifier in which the conditional probability density function corresponding to each feature is trained in form of a 1-D histogram.

Ricci and Pefetti [69] used a support vector machine (SVM) for the pixel classification. They used two orthogonal line detectors along with the gray-level of the target pixel and the pixel intensity to construct a 3-D feature vector.

Carmen Alina Lupascu *et al.* [70] used the adaBoost classifier to segment vessel pixels. They combined features from previous works and their own development to obtain a 41-D feature vector encoding information on the local intensity structure, spatial properties, and geometry at multiple scales. These features are responses to

Gaussian filters, model-based features used in [68], vesselness features developed in [72], Lindeberg ridges features in [73], Staal ridges feature in [66], Gabor wavelet features and other features.

Among the rule-based methods, one typical group of methods is referred to as vessel tracking/tracing, vectorial tracking approaches [74, 75, 76, 77, 78, 79]. These methods work by first locating an initial set of points established automatically or by manual labeling, and then exploiting local image properties to trace the vasculature recursively. They only process pixels close to the vasculature, avoiding the processing of every image pixel, and so are appropriately called exploratory algorithms. However, the tracing-based methods are naturally recursive greedy methods, which means that the mistake of failing to detect vessel pixels at any stage could propagate and compromise the final results.

Other methods are developed to use mathematical morphology [80, 81, 82] to benefit from a priori-known vasculature shape features, such as being piecewise linear and connected. Then, by applying morphological operators, vessels are filtered from the background for final segmentation.

Similar to the supervised pixel-classification method but without the classifier component, matched filtering techniques [83, 84, 85, 86, 87, 88] usually use a 2-D linear structural element with a Gaussian cross-profile section for blood vessel cross-profile identification (typically a Gaussian or Gaussian-derivative profile). The kernel is rotated into many different orientations (usually 8 or 12) to search for vessels with different orientations. The image is then thresholded to extract the vessel silhouette

from the background.

Besides, other methods which combine several strategies have also been developed. For example, a general framework based on a verification-based multi-threshold probing scheme was presented by Jiang *et al.* in [89]. The authors enriched this generic methodology by incorporating relevant information related to retinal vessels into the verification process with the aim of enabling its application to retinal images. Al-Diri *et al.* [90] developed a method using an active contour model to segment vessels. Deformable or snake models have been also used in [91]. A snake is an active contour model that, once placed on the image near the contour of interest, can evolve to fit the shape of the desired structure by an iterative adaption. Martinez *et al.* [92] proposed a method based upon multiscale feature extraction combined with region growing. The local maxima over scales of the gradient magnitude and the maximum principal curvature of the Hessian tensor were used in a multiple-pass region growing procedure. The growth progressively segments the blood vessels by using both feature and spatial information.

2.2.2 Determination of the Retinal Vessel Connectivity

The determination of vessel connectivity is to determine the anatomical connectivity of vessels, which is equivalent to locate and determine landmarks in the vasculature trees including bifurcations, crossing points, and end points. The 2-D retinal images are the projection image of the actual 3-D retina, thus the 3-D actual tree-like vasculature is projected onto a 2-D surface to form a complex graph-like

structure. This makes the construction of vasculature trees a special and difficult problem from a general tree construction problem. Although many works have been proposed for the vasculature construction in 3-D images, a smaller number of works have focused on the construction of the vasculature in the 2-D retinal images. To summarize the previous work, some of general methods for the vascular tree construction are reviewed first.

In 1993, Coppini *et al.* [93] proposed a bottom-up coronary artery extraction method based on angiogram edges. These edges are grouped into edge segments, which are organized to bar primitives, and ultimately linked to form artery segments. In 1993, Liu *et al.* [78] developed a three-steps recursive tracing-based method to construct 2-D vascular networks in angiograms. The first step is to segment vessels starting from a starting point with a trace-based method using direction information. Then the detected vessel pixels are deleted to preventing re-detection. The third step is to detect all branch points along these vessels by applying matched filters along both sides of the vessel. In 1996, Montesinos *et al.* [94] constructed trees by performing local to global optimization of an active contour by dynamic programming in 2-D medical and aerial images. In 2000, Yim *et al.* [95] combined an ordered region growing (ORG) algorithm and a skeleton-based algorithm to generate the vascular tree in magnetic resonance angiography (MRA). The image is represented by an acyclic graph via the ORG algorithm based on the connectivities of voxels. A seed is provided by a user to be the origin of the graph. Then the graph is skeletonized and vessel segments are extracted by tracing paths from the ends of vessel segments back to the

origin point. In 2002, Selle *et al.* [96] segmented hepatic vessels using a threshold-based region-growing method on CT images, with the threshold value automatically generated. The segmented vascular structure is skeletonized, and transformed into a vascular forest that contains a number of directed acyclic graphs, using a graph theoretical method. In 2002, Deschamps *et al.* [97] developed an algorithm that first converts a 3-D MR image of aorta to a threshold vessel potential image and performs perceptual grouping and contour completion. This fast marching algorithm identified contours as minimal paths between connected components.

Both Jomier *et al.* [98] and Bullitt *et al.* [99] both performed grouping of vessel segments using the minimum spanning tree algorithm in general 3-D image modalities based on segmentation images, but with different minimization criteria. Jomier used distance, angles, radius and radius ratio as features to classify junction using Mahalanobis distance, while Bullitt used the linear distance and image intensity as features as the cost for the minimum spanning tree. The problem is that the construction of the vasculature tree is based on the vessel segmentation. If there are errors in the segmentation procedure, they will compromise the performance of the results.

Since the retinal images are 2-D images of the projection of 3-D object, overlapping of different vessel trees occurs on the retinal fundus images, forming a complex network. Therefore general methods mentioned above are not well-suited for constructing vasculatures in retinal images. Thus special methods that can distinguish overlapping of vessels and normal bifurcations of vascular trees are needed. Among

them, a number of methods have been developed to use the local knowledge of vessels to construct the vascular trees by classifying landmarks of all kinds. Basically, these methods first segment vessels using various approaches, then they locate potential landmarks on the vessel segmentation. These landmarks are then further classified into bifurcations, crossing points and ending points. By identifying the types of landmarks, the vascular trees are constructed. Some methods also apply some post-processing procedures to rectify some mistakes during the classification to improve the accuracy.

Can *et al.* [76] developed a very simple method to extract bifurcations and crossing points. The authors first use tracing-based algorithm to obtain vessel segmentation. Then they reduce the segmented vessels to centerlines, and identify junctions as centerline intersection points. Lines are constructed from the intersection point to each of the segments, and are used to estimate the intersection angles and to distinguish branches and crossing points. Since it is very simple, this algorithm is only able to solve simple branches and crossings with no more than 3-4 segments in close proximity, but fails at complex junctions, where there are several vessel branches close together, or where segmentation has failed.

Shen *et al.* [100] and Grisan *et al.* [101] propose similar tracing algorithms to detect bifurcations and crossing points along the search of vessel points. The drawback of this type of approach is that the successful detection of bifurcations depends on the tracing algorithm. If the tracing algorithm fails to trace some vessel pixels, some bifurcations might be missed.

To obtain the properties of retinal vasculature, Martinez-Perez *et al.* [102] developed a semi-automatic method to build the retinal vasculature trees based on the vessel segmentation image. They first skeletonize the segmentation image then identify three types of significant points: bifurcation points, crossing points and terminal points. Then they track from every manually indicated root segment to iterate and form a tree. However, this method requires human intervention to prevent from failure when cases such as the following happen: 1) two close bifurcations are recognized as one cross point, 2) two vessels crossing at an acute angle cause the crossing point to be recognized as two bifurcations. Besides, this method requires human indication of arterial and venous vasculatures.

Bevilacqua *et al.* [103], Chanwimaluang *et al.* [104] and also Ardizzone *et al.* [105] propose similar techniques to detect landmarks using the neighborhood information of vessel centerline pixels after extracting a vessel centerline image. They both apply a local 3×3 neighborhood to probe for branching points and crossovers. The methods might work very well for the detection of bifurcation points, but sometimes one crossing point would be mis-classified into two bifurcations.

Tsai *et al.* [106] propose a model-based method using this strategy which iteratively traces the vessel centerline pixels using local neighborhood information, and then distinguishes bifurcations using a mathematical model which incorporates angle information.

Jung *et al.* [107] developed a method that first extracts vessel centerlines using the neighborhood information, then locates landmarks by finding cross-perpendicular

structures and Y-type structures within local neighborhoods. The drawback of this method is that it might fail to identify bifurcations and crossing points. Similarly, Bhuiyan *et al.* [108] used a classification method to segment the vessels and obtain the vessel centerlines, then detect bifurcations based on the neighborhood of each vessel centerline pixel.

Aibinu *et al.* [109] use a k-mean algorithm to segment vessels with intensity information and then to obtain vessel skeleton. Then they use multi-scale windows (3×3 and 5×5) to probe bifurcations and crossing points. Also they use a morphological dilation operation to merge near crossover points into one crossover point.

Calvo *et al.* [110] first segment vessels and use morphological processing to repair gaps in vessel segmentation. Then they locate landmarks based on an extended vessel skeleton. To classify these landmarks, they developed a two-step algorithm. The first step is to use multi-sacle neighborhoods to distinguish bifurcations and crossing points. The second step is to use topological analysis which mainly is the distance between landmarks to modify some classification results.

Azzopardi *et al.* [111] developed COSFIRE (Combination Of Shifted Filter Responses) filters to detect bifurcations based on vessel segmentation images. The COSFIRE filters are built based on the responses of Gabor filter banks and their relative locations and orientations with respect to points of interest in terms of blur and shift parameters.

Fathi *et al.* [112] proposed a mathematical model-based approach to detect landmarks based on vessel segmentation images. They used a local vessel pattern

operator to detect vessel landmarks and then to measure vessel features like the orientation, the width and the bifurcation angle. Then the vessel features are used to re-validate the landmark types. However, these methods are based on vessel segmentation images thus the errors in vessel segmentation would compromise the results. Since there is no a perfect automatic vessel segmentation technique, the performance of these methods are contolled by the vessel segmentation approaches.

Based on their previously-developed vessel segmentation method [90], Al-Diri *et al.* [113] firstly locate vessel segment ends when vessels are traced, then organize these ends into local sets, and then use self organization feature maps (SOFMs) to model cost functions for the junctions in order to resolve the configuration of local sets of segment ends, thus determining the network connectivity.

The main drawback of the methods mentioned above is that they intend to use local vessel information to detect landmarks and determine the vessel connectivity, depending on local and/or greedy decisions. Depending too much on local information make these methods are susceptible to local errors, especially for an imperfect image or an automated segmentation. Some of the following errors can easily happen for an imperfect image: (a) a crossing point is misclassified as a bifurcation when one vessel is missing or disconnected; (b) a missing part of vessels causes the disconnection of the tree; (c) spurious vessels generate false bifurcations and crossings. In addition, complex landmarks are hard to recognize with local knowledge, i.e. two overlapping vessels which would be misclassified as one vessel, and two overlapping landmarks. Although some methods have post-procedures to rectify these mistakes by checking

a larger neighborhood, in essence it does not change the local or greedy nature of these methods. Some of other methods are thus proposed which combine the global property of the vasculature to help building the vascular trees.

Lin *et al.* [114] (2009) [115] (2010) [116] (2012) developed a tracing algorithm combined a grouping method to build the vasculature tree. They first obtained a likelihood ratio vesselness (LRV) image using a learning technique. Then they use a tracing algorithm to obtain a set of disconnected vessel segments. A grouping algorithm is then applied to re-connect these vessel segments to form trees. The grouping algorithm iteratively connects ungrouped segments to grouped segments by maximizing the continuity of the vessel using an extended Kalman filter.

Rothaus *et al.* [117] proposed a structure-based method given a pre-segmentation image to separate arteries and veins. Based on a pre-segmentation image, they obtain the skeletonized vessel segments and identify bifurcation crossing points. Then they modeled the problem of labeling vessel segments arteries or veins as a satisfiability problem and propagates the labels of vessels from some initial labels. However, manual inputs are mandatory to determine the initial labels and more manual inputs are required if there are some conflicts that cannot be resolved by the algorithm.

Very recently, Estrada *et al.* [118] proposed a semi-automatic graph-based method to construct the retinal trees. They first semi-automatically extract a graph representing the vasculature from a fundus image, then separate it into arterial and venous trees by maximizing a likelihood of arterial and venous trees. Their experiment shows a good result, but the trees are semi-automatically constructed and thus the

method needs human efforts.

2.2.3 Separation of Vessels in Fundus Images into Arteries and Veins

One of the earliest work about the recognition of arteries and veins in retinal images is proposed by Grisan *et al.* [119] in 2003. They propose to divide the fundus image into four regions of interest and classify the blood vessels locally into arteries and veins based on a feature vector consisting of color properties using an unsupervised fuzzy clustering algorithm. Based on a tracking algorithm they obtain a set of disconnected vessel segments. Then they partitioned a concentric zone around the optic disc into quadrants and choose the five largest vessel segments within each region to classify. However, this method might fail at some regions which do not contain enough vessels to classify. Most importantly, this method only considers local morphological information and does not identify connectivities between vessels, which makes the error rate on secondary vessels much higher than that of the main vessels.

Later, to facilitate the automated analysis of arteries and veins in retinal images, a number of methods are proposed to distinguish the arterial and venous trees. One typical strategy of these methods are to determine the vessel connectivity first, then use machine learning methods to recognize arterial and venous trees [120, 121, 122, 123, 124]. For these methods, a vessel tracking algorithm [120, 123], or a graph-based algorithm [121, 124] are first used to construct the trees by determining vessel connectivities. Then different machine learning algorithms are used to extract the

discriminating features of arteries and veins then to classify these trees into arteries or veins. The main drawback of these methods is that the errors generated during the tree construction would greatly compromise the final result of arterial and venous tree construction.

Another typical strategy is to directly use machine learning methods to classify arteries and veins [122, 125, 126, 127, 128], and then to measure these vessels without determining the connectivity between arteries or veins since some of clinical properties of arteries and veins do not require the connectivity information. However, since these type of methods mainly use the local neighboring intensity and profile information to distinguish arteries and veins, they are not very accurate to classify small vessels, as well as vessels far away from the optic disc due to the increasing similarity between arteries and veins. This technical disadvantage would not be severe for the case when only major vessels are concerned in clinics, but it would compromise the results when the complete vessel tree analysis is necessary.

2.2.4 The Retinal Vasculature Analysis

Changes of the retinal vasculature have been associated with many diseases, disorders and health conditions, as described in section 2.1.3. To quantify and measure these changes, features are designed and methods are developed to semi-automatically or fully-automatically to collect these data from fundus photographs. Common features are the vascular tortuosity (arteriolar and venular tortuosities) [129, 130, 131, 132], branching angle at bifurcations [45], arteriolar length-to-diameter ra-

tio [44, 133], microvascular density [45, 46]. Besides these features, the retinal vessel width is one of the most important features that ophthalmologists are evaluating on the retinal vasculature, due to its strong association with many diseases mentioned before.

The most widely used measurement to quantify the retinal vessel width are central retinal artery equivalent (CRAE), central retinal vein equivalent (CRVE) and artery/vein ratio (AVR). CRAE/CRVE is aimed to estimate the metric of real interest, the diameters of the central retina artery and vein, which are invisible in ocular imaging, yet are believed to be the real biomarker of many diseases. AVR is the ratio of CRAE and CRVE. The concept of CRAE/CRVE was first introduced by Parr and coworkers [134, 135] and it is based on the assumption that visible retinal vessels originate from the central retinal artery and that all visible retinal veins flow to the central retinal vein, and also that the widths of the branches of retinal vessels have a specific mathematical relationship, called Murray's law [136], in normal subjects. Practically, the average widths of a subset of arterioles/venules around a concentric zone centered on the optic disc are estimated, and they are converted to a single number to approximate the width of the central artery/vein, thus the terms Central Retinal Artery Equivalent and Central Retinal Vein Equivalent.

The approach was further improved by Hubbard [38] and Wong [137] and later Knudtson [138] introduced a semi-automatic method called the revised Parr-Hubbard formulas that facilitates the estimation, which use scaleless equations for conversion and with a different selection strategy that only selects the six largest arteries and the

six largest veins. Since them, based on these same assumptions, various types of fully automatic methods have been developed to calculate CRAE/CRVE and AVR [120, 128], including one developed by our group [139].

Despite the wide application of CRAE/CRVE, the methods to calculate them are somewhat subjective and sensitive to inter-observer variability. In both semi-automated and fully automated versions, the decision of which vessels to include and not include in the calculation is arbitrary. The criteria of inclusion might be too specific thus introducing bias, or too general, thus introducing noise due to the mis-classification of arteries and veins by semi-automatic or automatic algorithms. Also it is ambiguous how to handle overlapping arteries and veins, which often happens in the region close to the OD.

CHAPTER 3
THE AUTOMATIC DETECTION OF RETINAL VESSEL BRANCH

3.1 Introduction

To construct anatomical vascular trees, one key component is to detect the connectivity between vessel segments, which can be transfered to the problem of detecting the important landmarks on the vessels. To complete this task, we developed the optimal filter approach to detect bifurcations. The optimal filter approach [140] is a formalized machine-learning approach that allows an unbiased, almost parameterless, automated system for object-background separation. Essentially the only input it requires to build the object detector is a limited number of expert-marked exemplar objects. The name of the optimal filters is derived from the function of the filters that maximally represent positive samples in the feature space against negative samples. It has been compared to other filterbank-based approaches for the separation of object and the background. Considering bifurcations as independent objects, we can use this method to detect them. The work in this chapter is published in SPIE Medical Imaging 2013 [141].

3.2 Methodology

In summary, the optimal filter framework consists of a training and a test stage as shown in Fig. 3.1. During the training stage, a set of fundus images $\mathcal{S}$ with expert-annotated bifurcations, indicated as in Fig. 3.2, is used to build the optimal filters, and to implicitly or explicitly build the classifier. Internally the training set

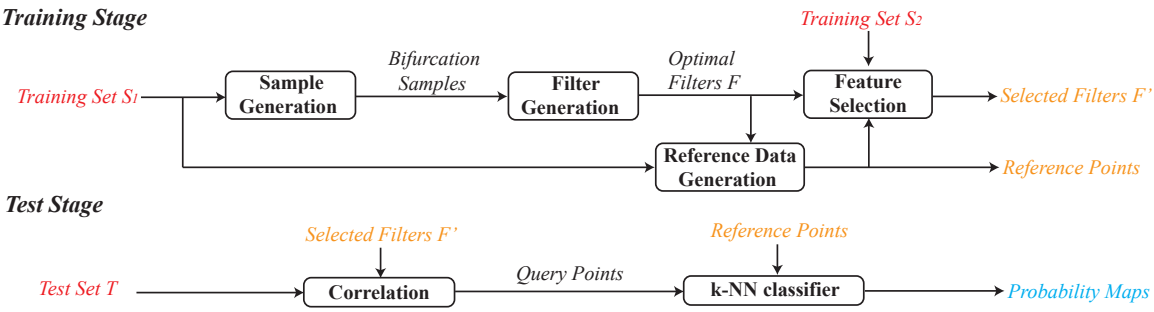

Figure 3.1: The framework of the optimal filter approach.

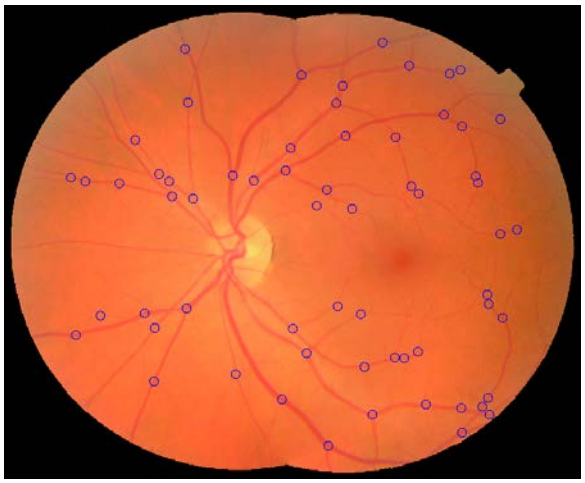

Figure 3.2: A color fundus image, with annotated bifurcations labeled by blue circles.

$\mathcal{S}$ is divided into two sets, $\mathcal{S}_1$ and $\mathcal{S}_2$. $\mathcal{S}_1$ is used to build the filter set $\mathcal{F}$, while $\mathcal{S}_2$ is used to perform feature selection on $\mathcal{F}$, resulting in selected filter set $\mathcal{F}'$, from which we form the feature space and generate reference points. Then a classifier is trained to detect bifurcations for a fundus image in terms of generating a soft-labeled map indicating the probability of every pixel being a bifurcation.

During the test stage, a probability map is generated for every test image

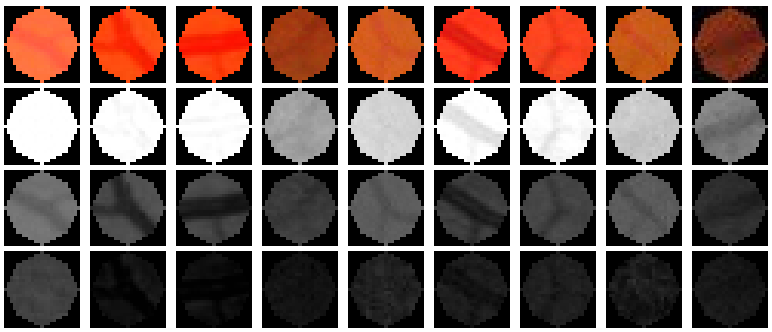

Figure 3.3: Bifurcation samples (1st row), and in red (2nd row), green (3rd row) and blue (4th row) channels.

in $\mathcal{T}$, and the bifurcation probability map is then thresholded to determine where the bifurcations are located, and the performance is evaluated and is compared to the ground truth. To maintain generality and robustness, $\mathcal{S}_1$, $\mathcal{S}_2$ and $\mathcal{T}$ are representative images from the real data that are kept entirely separated. The following parts discuss the details of the developed framework, including the sample generation, filter generation, bifurcation detection, feature selection, and the evaluation metric.

3.2.1 Sample Generation

By annotating the center of bifurcations in $\mathcal{S}_1$ and $\mathcal{S}_2$, we obtain bifurcation samples as sub-images at a specific scale σ (measured in pixels). To achieve rotational invariance, each sample is rotated by 0°, 45°, 90°, 135°, 180°, 225°, 270° and 315°. In preliminary studies, we did not find an advantage in using a higher number of orientations, though this may differ if the scales of the samples are different. To obtain a consistent sample image pattern, a circular mask is superimposed on the

rotated sample image to generate circular samples. In addition, we decompose the sample images into red, green and blue channels (Fig. 3.3), and samples in these channels are considered as independent sample sets.

3.2.2 Filter Generation

We use principal component analysis (PCA)[142] to generate the filter sets which define the feature space. PCA is an orthogonal transformation converting the original data into a new coordinate system so that they are represented by a small number of linearly uncorrelated variables called principal components (PCs). In our method, every bifurcation sample image is a single observation, and by applying PCA on the samples set for each channel, the PCs we obtain can represent any instance of that samples set. If we retain the first M PCs such that their cumulative variance (CV) is the majority of the total variance, they could be used to approximate any instance of bifurcations, and that is the reason they are called the optimal filters [140]. The optimal filters thus found span the multi-dimensional feature space into which any image pixel can be projected.

Bifurcation samples extracted from $\mathcal{S}_1$ are projected into the initial feature space by convolving them with these optimal filters for later usage. In particular, bifurcation samples in training set $\mathcal{S}_1$ are projected into the feature space to form the positive reference points. Likewise, non-bifurcations are randomly sampled in $\mathcal{S}_1$ and projected into the feature space to form the negative reference points. While all features are computed here, in the trained algorithm, this is only done with those

filters that span the final, low-dimension feature space, which results from the feature selection (3.2.4).

3.2.3 Bifurcation Detection

Once we generate the feature space with reference points, a classifier is trained for the detection of bifurcations. An image under detection is transferred into the feature space by being convolved with filters so each pixel corresponds to a query point in the feature space. A k-nearest neighbor (k-NN) algorithm is chosen here to classify these query points. Soft classification is applied so the probability of the query point p to be a bifurcation is n/k, where k is the number of neighbors considered and n is the number of positive points among these neighbors.

3.2.4 Feature Selection

The dimension of the feature space is the number of filters (i.e. PCs). Since the feature space is defined by the set of optimal filters, here features and filters are interchangeable. For efficiency we apply feature selection to lower the dimension since the initial feature space is a high-dimensional space. Here we adopt the Sequential Forward Selection (SFS)[143] approach which starts with a candidate feature pool and, for each iteration, selects out the best remaining feature according to a criterion, until the maximum number of features is reached or the criterion value starts to decline. The detailed flowchart of the feature selection process is summarized in Fig. 3.4. Training set $\mathcal{S}_2$ is used to generate the probability maps using the method described in Section 3.2.3. The probability maps are generated with selected filters

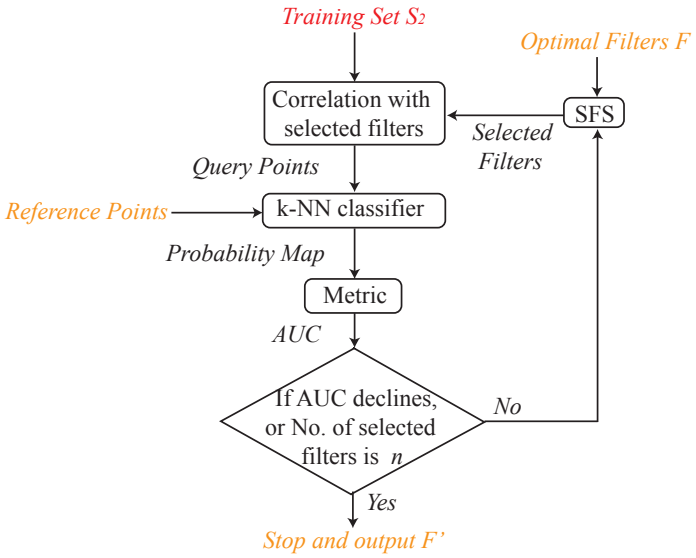

Figure 3.4: The flowchart of feature selection.

every iteration. The criterion to guide the selection is the AUC for the ROC curve for the whole set of probability maps, which will be explained later in section 3.2.5.

3.2.5 Evaluation

The metric to calculate the AUC is pixel-based. We define a bifurcation region with radius of R centered at every annotated bifurcation pixel. A bifurcation probability map is thresholded to obtain a binary image. Every pixel P of the binary image is decided as true positive (TP), false positive (FP), true negative (TN) or false

negative (FN) depending on whether they fall within bifurcation regions or outside:

$$P = \begin{cases} TP & \text{if } P \text{ is labeled and } |P - B| < D \\ FP & \text{if } P \text{ is labeled and } |P - B| > D \\ TN & \text{if } P \text{ is unlabeled and } |P - B| > D \\ FN & \text{if } P \text{ is unlabeled and } |P - B| < D \end{cases} \tag{3.1}$$

Here D is the radius of the bifurcation region, and B is an annotated bifurcation in the ground truth image. For n test images, n probability maps are generated with selected filters. The n probability maps are thresholded with different values to generate different pairs of specificities and sensitivities, so the overall ROC is plotted and the AUC is calculated.

The data is highly skewed since the number of bifurcation pixels are small compared to the number of the whole image pixels; thus the ROC is insensitive to the change of specificity. For better discriminability of ROC, we weigh positive points with a self-defined factor F larger than 1, which enhances the influence of positive points so the ROC curve is more sensitive to changes of sensitivity and specificity. Here we define F as $2 \times$ (total No. of negative/total No. of positive)$^{\frac{1}{2}}$. Assuming there are n images used for evaluation, the metric giving the AUC for the probability maps is outlined as follows:

- find the threshold values v_0, v_1, v_2, ... v_k for all probability maps
- for threshold value $i = v_0$, ... v_k
  - threshold all probability maps and obtain thresholded images m_{i1}, m_{i2},..m_{in}

  - compute TP, FP, TN and FN for m_{i1}, m_{i2},..m_{in}
  - sum all TP, FP, TN and FN together for all thresholded images
  - calculate the sensitivity and specificity for threshold value i

- compute the AUC according to the pairs of sensitivity and specificity for all threshold values.

3.3 Experiments and Results

The data we use are 80 retinal color images from 80 subjects, created by the registration of 2 separate images per patients as described in detail in the reference[144]. The size of images is approximately 800 × 650 pixels in JPEG format. The numbers of images in $\mathcal{S}_1$, $\mathcal{S}_2$ and $\mathcal{T}$ are 50, 10 and 20 respectively. To generate the ground truth, the centers of bifurcations were manually annotated by a trained reviewer and a retinal specialist reviewed the annotations for correctness.

Bifurcations are sampled at a scale σ of 25 × 25 pixels. In the training stage, 10 bifurcations are randomly sampled per image so that 500 samples are created from $\mathcal{S}_1$, and rotating them in 8 directions results in 4000 samples in total. PCA was applied separately on the samples in red, blue and green channels to generate the set of optimal filters. Figre 3.5 shows the first 12 filters in three channels. In Fig.3.5, the patterns complexity of the PCs increases as the index of the filter increases, which justifies the fact the information of bifurcation samples are concentrated in the first few number of PCs. Figre 3.6 shows the CV of PCs in three channels respectively. It indicates that the CV in the blue channel has a slower increase compared to those

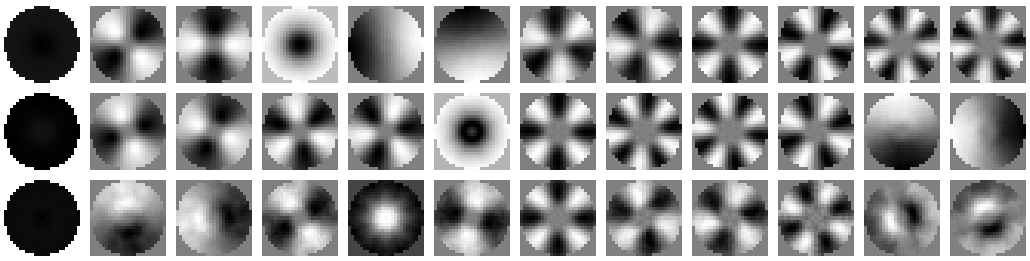

Figure 3.5: First to 12th PCs in red channel (1st row), green channel (2nd row), and blue channel (3rd row).

in the red and green channels, which is consistent with the fact that there is little information but noise in the blue channel. Thus we only use PCs in red and green channels as our optimal filters. We select the first 30 PCs of red and green channels for feature selection since the cumulative variance of first 30 PCs in the two channels is higher than 96%.

Two thousand non-bifurcation samples are randomly selected per training image, generating a total of 100000 negative points in the feature space. Ten filters were selected from the feature selection procedure to build a 10-D feature space. The radius R of the bifurcation region is $\sqrt{41}$ according to the vessel width in images. We use Approximate Nearest Neighbor (ANN)[145] to accelerate the k-NN classifier, and test on images in $\mathcal{T}$ with $k = 33$. The metric we use to evaluate the results is the same as we use in feature selection. The AUC is 0.883 and Figure 3.7 shows the ROC curve.

Figure 3.8 is a visual example. Figre 3.8 (a) is the probability map of the

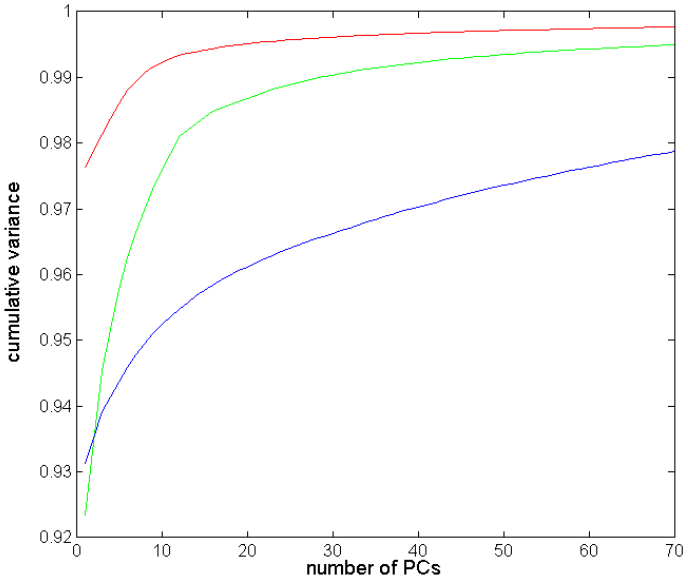

Figure 3.6: CV in three channels with respect to the number of PCs.

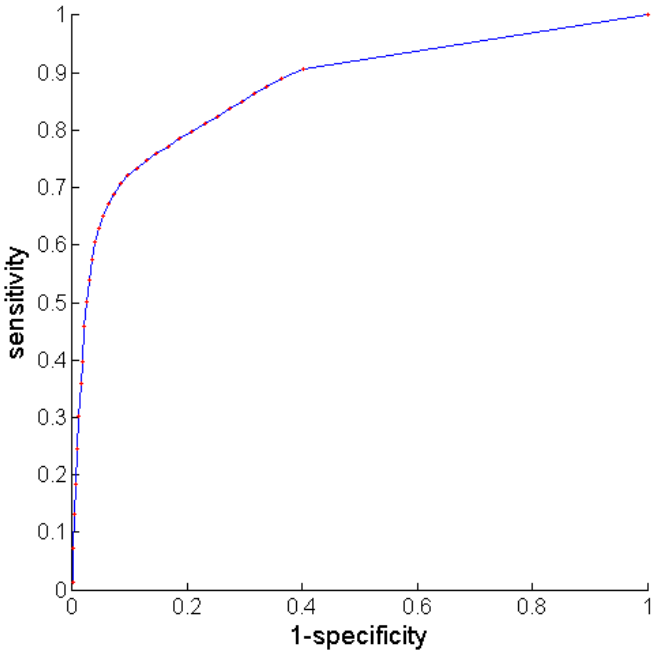

Figure 3.7: The AUC is 0.883 for test images with 10 selected features.

fundus image shown in Figre 3.2. Figre 3.8 (b) is a thresholded binary map indicating bifurcations, overlapped with the fundus image. The white pixels are TPs, and black pixels are FPs. As shown in the figure, our method can find most of the bifurcations with few false positives. Most of the false positives occur within and near the optic disc because of the similarity between the appearance of vessel pixels near or within the optic disc and that of bifurcations. Another types of false positive happens at crossing points, which are easily misclassified as two conjunctive bifurcations. Our method also misses some of small bifurcations when the radius of the retinal vessel is extremely small or with the absence of one vessel. The failures of detecting these bifurcations might be because these bifurcations have different appearance compared to normal bifurcations and the optimal filters cannot capture their morphological characteristics.

3.4 Conclusion

In this chapter, an optimal filter-based retinal bifurcation detection method is presented based on a limited number of annotated retinal images with exemplar branch point samples. Compared to other methods, this approach requires little directly morphological information about the target, and only has a few parameters: the scale σ of the sample, the numbers of positive samples and negative samples, and a classifier. Furthermore, the parameter scale σ might be eliminated if we adopt a multi-scale approach, which would be the focus of our future work. In conclusion, using the optimal filter framework, a method to automatically detect bifurcations of

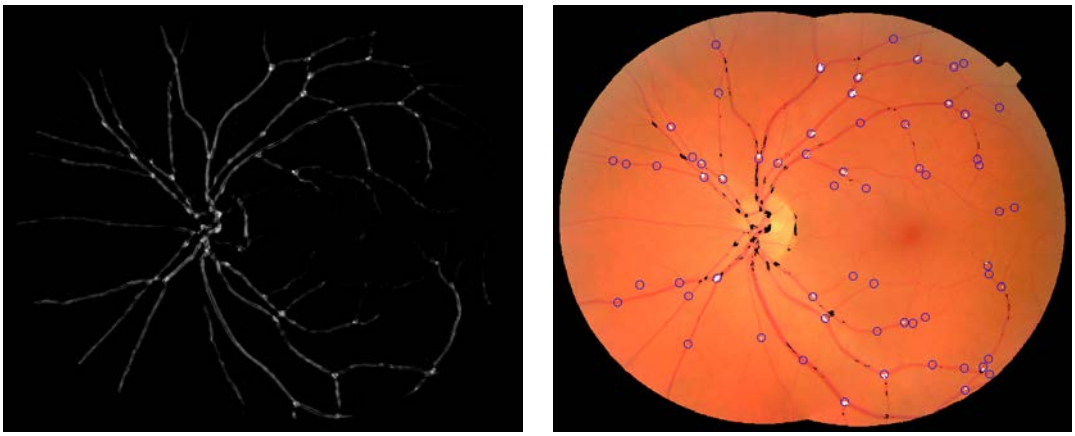

(a) (b)

Figure 3.8: An example of output. (a) The probability map (b) The binary map overlapped with the original image. Bifurcations are labeled with circles, and white pixels are TPs, and black pixels are FPs.

the retinal vasculature has been developed. It does not require feature extraction with human design, thus it only needs very little expert contribution. This method is tested on 20 fundus images, resulting in a general AUC of ROC curve of 0.883.

CHAPTER 4
THE AUTOMATIC CONSTRUCTION OF ARTERIOVENOUS VESSEL TREES IN FUNDUS PHOTOGRAPHS

4.1 Introduction

Since the retinal fundus image is a 2-D projection image of a 3-D structure, the 3-D retinal tree-like vasculature is projected on a 2-D surface to form a complex network. The purpose of the construction of vasculature is not only to identify vessels, but most importantly to determine the actual connectivity between vessels on the fundus images. As discussed in Section 2.2.2, the existing approaches for the vascular construction usually depend on local and/or greedy decisions and are correspondingly susceptible to local errors, especially for an imperfect image or an automated segmentation. Some common errors that would happen for these methods are: (a) the misclassification of a crossing point as a bifurcation when one vessel is missing or disconnected; (b) the disconnection of the vascular tree due to a missing part of a vessel; and (c) the identification of false bifurcations or crossing points due to spurious vessels. In addition, complex landmarks are difficult to recognize with local knowledge (e.g., two overlapping vessels which would be misclassified as one thick vessel, and two overlapping landmarks).

In this chapter, a novel and more global framework is presented to build the vasculature which tolerates errors introduced during imaging and image preprocessing, specifically vessel detection or vessel segmentation. The developed method takes a vessel segmentation as the input, and finds the actual connectivity between

vessels to build the vasculature. The output of the algorithm is multiple vascular trees in form of the vessel centerlines. We first introduce the procedures and basic theories of this framework. Then we present the details of the construction of the cost functions, which are essential to the framework. Then we present the experiments to test the algorithm and results of the evaluation. Work in this chapter has been published in Medical Image Computing and Computer-Assisted Intervention (MICCAI) 2013 [146] and SPIE Journal of Medical Imaging 2015 [147].

4.2 Methodology

In general, the developed framework consists of three main stages, summarized in Figure 4.1. Taking a vessel segmentation as the input, in the first stage it generates a vessel potential connectivity map (VPCM). A VPCM is an over-connected vessel network consisting of vessel segments and the potential connectivity between them. In the second stage, the VPCM is disambiguated into multiple anatomical trees with two labels. The tree disambiguation problem is modeled as a constrained optimization problem, and solved by using a special graph with a meta-heuristic optimization algorithm. To separate the VPCM, both local and global costs are calculated on the VPCM for the optimization problem. Finally in the third stage, these separated anatomical trees, as well as independent trees, are classified into A/V trees using a machine-learning method. The following text describes the details of the framework.

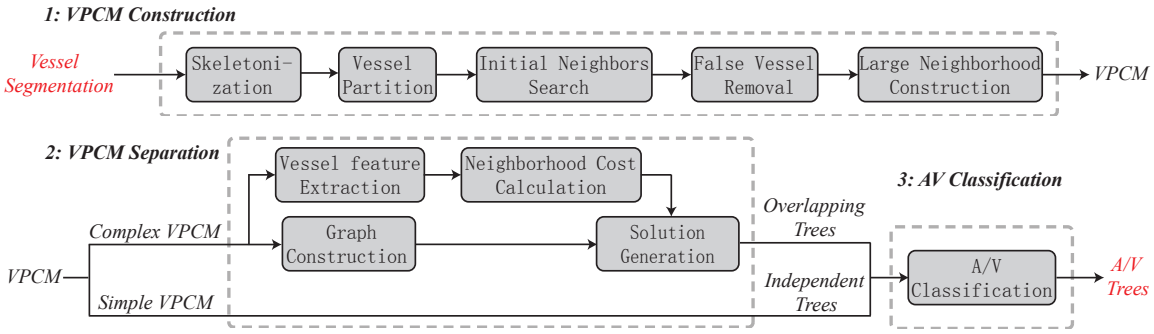

Figure 4.1: The flowchart of the developed framework.

4.2.1 The Vessel Potential Connectivity Map

Before describing the algorithm, we first introduce the concept of a Vessel Potential Connectivity Map (VPCM), which is an important notion of this method, then explain every step to build a VPCM. A VPCM is a vessel network consisting of partitioned vessel segments in terms of centerlines and their potential anatomical neighbors. For a VPCM, each segment v_i has two ends ep_{2i} and ep_{2i+1}, which are connected to the ends of neighboring vessels. A neighborhood, denoted as $\mathcal{N}_k$, is a set of end points whose segments are connected on the VPCM. If end points $ep_h, ep_g \in \mathcal{N}_k$, then they are neighbors and segments that they belong to, $v_{\lfloor h/2 \rfloor}$ and $v_{\lfloor g/2 \rfloor}$, are also neighbors. The size of a neighborhood, denoted as $|\mathcal{N}_k|$, is the number of segment ends within $\mathcal{N}_k$, or the number of segments connected within. An example is shown in Figure 4.2. Figure 4.2(b) shows a set of vessel segments, and Figure 4.2(c) shows the corresponding VPCM virtually. In this example, segment v_0 has two indexed ends ep_0 and ep_1, and ep_1 has two neighbors ep_2 and ep_4. Altogether they form a neighborhood $\mathcal{N}_1 = \{ep_1, ep_2, ep_4\}$, and therefore segments v_0, v_1 and v_2 are neighbors

as well.

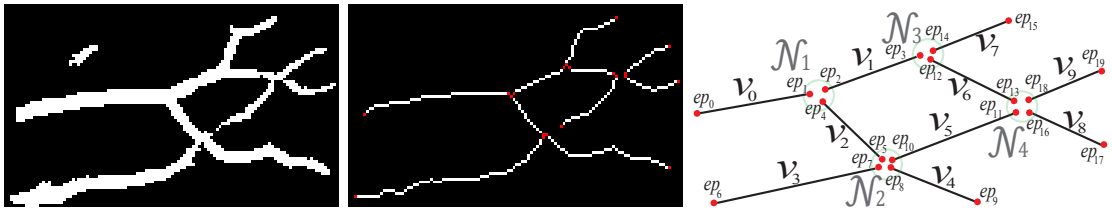

(a) (b) (c)

Figure 4.2: A VPCM example (only a portion of the image is shown). (a) The vessel segmentation. (b) Vessel segments (end points in red). (c) The virtual VPCM.

Here two assumptions about the VPCM are introduced as the prerequisite of the proposed method. The first is based on the property of the vasculature in 2-D retinal images that arteries do not cross arteries and veins do not cross veins. With this property, we assume that **within each neighborhood, segments of the same type are connected anatomically and segments of different types are not connected anatomically**. In other words, if two segments are of the same type in a neighborhood, we assume that they are connected. If they are of different types, they are not connected. Because of this constraint, for each neighborhood, determining the anatomical connectivity between segments is equivalent to determine the types (artery or vein) of the segments. The second assumption is that **the anatomical connectivity between segments is included within a neighborhood**. It means that to determine the anatomical connectivity between segments, we only need to check

whether two segments within each neighborhood are anatomically connected or not. In other words, it means that all neighborhoods cover all possible landmarks of the vasculature. With these two assumptions, to build A/V trees, we only need to determine the anatomical connectivities of segments (ends) within every neighborhood, which is equivalent to determining the segment types within every neighborhood. Neighborhoods cannot be too small which will violate the second assumption and pre-exclude the true anatomical neighbors, and cannot be too large which will violate the first assumption, and may cause two segments of the same type not anatomically connected to be included within one neighborhood.

4.2.2 The Construction of VPCM

Assuming we have a vessel segmentation, either manually or automatically generated, we first extract the vessel centerlines using a general skeletonization algorithm [148], and then we separate the vessel skeleton into disconnected segments. This is done by finding two ending pixels for each segment. First we check the 3×3 neighborhood for all centerline pixels and classify them into normal points and special points. Normal points are centerline pixels which have 2 neighboring centerline pixels; special points are centerline pixels which have either 1 or more than 2 neighboring centerline pixels. Then, we divide the centerlines into segments by finding pairs of special points. The details are referred in Appendix A, since it is less relevant to the main algorithm in the work.

After separating the skeleton into segments, we over-connect them to build

the VPCM in two steps. The first step is to initially find neighboring segments for both end points of each segment in a small region. The shape and direction of the region is defined as shown in Figure 4.3. For an end point of ep_{2i} from segment v_i (red pixel in Figure 4.3), if there is an end point ep_m from other segment $v_{\lfloor m/2 \rfloor}$ within its search region (dark gray pixels in Figure 4.3), ep_m is connected with ep_{2i} and $v_{\lfloor m/2 \rfloor}$ is a neighbor of v_i.

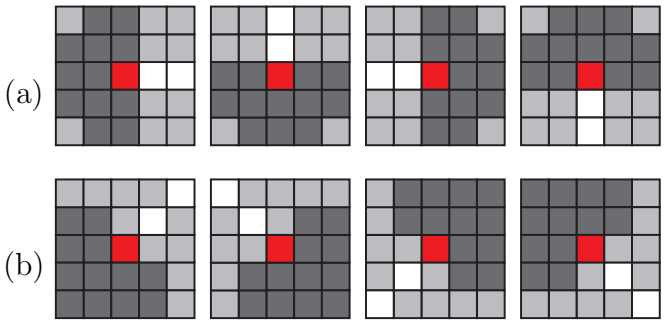

Figure 4.3: Two types of search region, which are shown in dark gray and the end point is in red and vessel centerlines in white. (a) The vessel direction is in either horizontal or vertical direction. (b) The vessel direction is in a diagonal direction.

After the initial neighborhood construction, short isolated segments less than 12 pixels are removed because the majority of them are false positives, and the rest are of little clinical significance.

Meanwhile, the centers of the optic disc and the fovea (if there is one) are detected for later usage of further neighbor searching. Here a pixel-based classification

algorithm is developed based on the work of Niemeijer et al. [149]. A circular template (Figure 4.4) that iterates over all pixels is designed to extract features. The template is separated as four quadrants, as well as the inner and the outer sections, with radius $R_t = 45$. The features for the OD and fovea are calculated based on different regions of the template, listed in Table 4.1. Samples points are obtained in 50 images for both the OD and the fovea. Two SVM classifiers are trained separately for the OD and the fovea detection. The algorithm generates an OD probability map and a fovea probability map, which are thresholded to binary images. Then the largest connected components are selected out in the binary images, and the geometrical centers are the center of the OD and the fovea. In addition, because the vessels within the OD is difficult to detect and trivial due to their messiness, the OD is masked out by approximating the radius of the OD, based on the assumption that the OD is in a circular shape. Assuming the images are processed under a similar scale, the radius of the OD is considered as a number between between 40 and 90 pixels, and maximizing the overlapping edge responses from the Gaussian-derivative-filtered OD probability map over the size of the OD.

The next step is to find additional potential neighbors for vessel segments in a larger region using a two-step algorithm. The first step is to explore neighbors for segment ends having no neighbors by artificially extending the segment. The extension is defined as a region theoretically similar to a circular sector whose radius is r and central angle is $\theta = 30°$. Figure 4.5(a) shows the shape in the continuous domain, and Figure 4.5(b) shows the shape in the digital image domain. The extension region

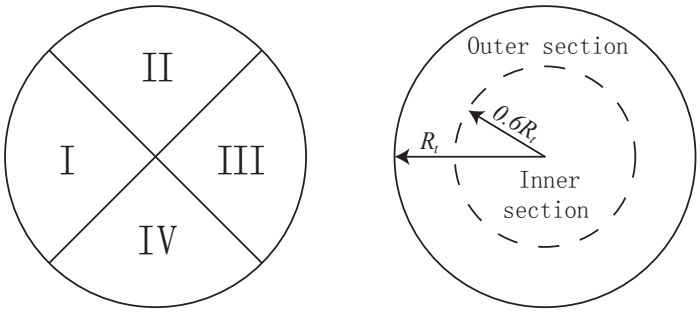

(a) (b)

Figure 4.4: The template with two forms of region separation. (a) The template with four quadrants. (b) The template with inner and outer sections.

Table 4.1: Feature summary for the detection of OD and the fovea.

Feature No.	Feature Description	for OD	for fovea
1-4	The number of vessels pixels in four quadrants		*
5-8	The average width of vessels in four quadrants		*
9	The number of vessel pixels in the whole template	*	*
10-15	The mean and std. of intensities in R,G,B channels in the inner section	*	*
16-21	The mean and std. of intensities in R,G,B channels in the outer section		*
22-25	The average of the orientation of vessel segments on the border of the four quadrants	*	*
26-29	The number of vessel segments going through the border of the four quadrants	*	

is iteratively grown by increasing r until a neighboring segment is found, or r reaches a limit r_l. Here r_l (Eq. (4.1)) is determined by a function of the vessel length l, the vessel tortuosity t [150], and an arc weight r_a (Eq. (4.2)):

$$r_l = \begin{cases} a/t + r_a & \text{if } l < l_a \\ (a + 0.1 \times (l - l_a))/t + r_a & \text{if } l_a \leq l < l_b \\ b/t + r_a & \text{if } l_b \leq l \end{cases} \tag{4.1}$$

$$r_a = \begin{cases} 0 & \text{if } d_a > 30 \\ 1000 \cos^3 \delta / d_a & \text{otherwise} \end{cases} \tag{4.2}$$

In our experiment, $a = 8$, $b = 10.4$, $l_a = 16$, $l_b = 40$. The arc weight encourages segment ends that are near and aligned with major vessels to have a greater maximum extension. The major vessels are the two largest vessels on a fundus image. They are obtained by downsampling the vessel segmentation, thresholding and skeletonizing it, and then finding the two largest connected components. Then these two major vessel arcs are represented by 2nd degree curves (Figure 4.6). In the arc weight equation given by Eq. 4.2 above, d_a is the nearest distance between a segment end and an arc and δ is the angle between the direction of the segment end and the tangent line of the nearest point on the arc.

The extension region finds a neighbor using Algorithm 4.1. Examples of the extension region with different connection cases are shown in Figure 4.7.

The second step is to merge close neighborhoods. A boundary is defined for

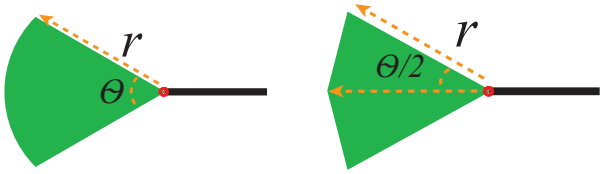

(a) (b)

Figure 4.5: The shape of the extension region.

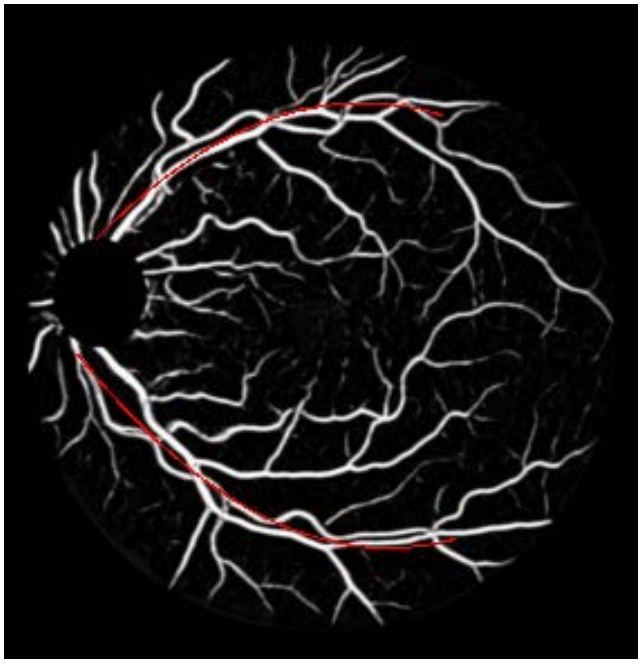

Figure 4.6: An example of downsampled vessel segmentation with major vessel arcs in red.

Algorithm 4.1 The algorithm to link neighboring segments

for each end ep_j which has no neighbors **do**

while ep_j has no neighbor and $r < r_l$ **do**

increase r and construct the region R_j

if R_j meets an end point ep_k of another segment **then**

connect ep_j to ep_k and ep_k's neighbors if there are any (Fig. 4.7 (a))

else if R_j meets a vessel centerline p **then**

break vessel at p into two segments, which generates two new end points ep_l and ep_m, form ep_j, ep_l and ep_m as a neighborhood (Fig. 4.7 (b))

else if R_j meets another extension R_k from end ep_k **then**

connect ep_j to ep_k and ep_k's neighbors if there are any (Fig. 4.7 (c))

end if

end while

end for

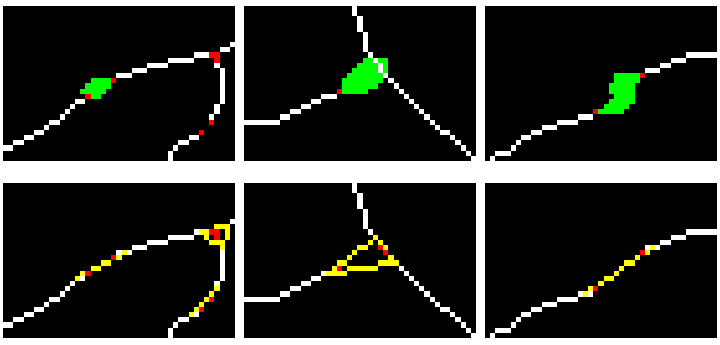

(a) (b) (c)

Figure 4.7: First row: Three different cases of finding a neighbor. Second row: The corresponding neighborhood constructed.

each neighborhood $\mathcal{N}_k$, and a neighborhood will merge with others if their boundaries contact. The boundary is a polygon whose shape is defined according to $|\mathcal{N}_k|$.

When $|\mathcal{N}_k| = 1$, the boundary is an extending segment of length $l_x = r_l$ from the vessel end.

When $|\mathcal{N}_k| = 2$, the boundary is a quadrangle (see Figure 4.8(a)). Two of the crests P_1 and P_2 of the quadrangle are on the segments whose distance to their respective end points is d, which is controlled by the width of the two segments. Another two crests P_3 and P_4 are defined using Eq. (4.3), where θ is the angle between the directions of the two segments; r is a constant, which is set as 7 in our experiment; $\mathbf{d_1}$ and $\mathbf{d_2}$ are the directions of the two segments. C is the centroid of ep_i and ep_j.

$$\begin{aligned} P_3 &= C + r(\cos\theta + 1)\mathbf{d} \\ P_4 &= C - 0.5r(\cos\theta + 1)\mathbf{d} \\ \text{where, } C &= ep_i + ep_j, \mathbf{d} = \frac{\mathbf{d_1} + \mathbf{d_2}}{|\mathbf{d_1} + \mathbf{d_2}|} \end{aligned} \tag{4.3}$$

An example of the boundary on the image domain is shown in Figure 4.8(b) and Figure 4.8(c).

When $|\mathcal{N}_k| = 3$, the boundary is a triangle. The three crests of the triangle are on the segments whose distances to their respective end points are d_i. Assume θ_1, θ_2 and θ_3 are the three angles between directions of segments in a neighborhood. If they are all larger than 110°, $d_i = 3$ (see Figure 4.9(a)); Otherwise, $d_i = 3$ for segments whose directions form the smallest angle, and $d_i = r_3 \cos\theta_{min}$, where r_3 is a constant, which is set as 12 in our experiment, and θ_{min} is the smallest angle (see Figure 4.9(c)). An example of each of the cases in actual digital image space is shown

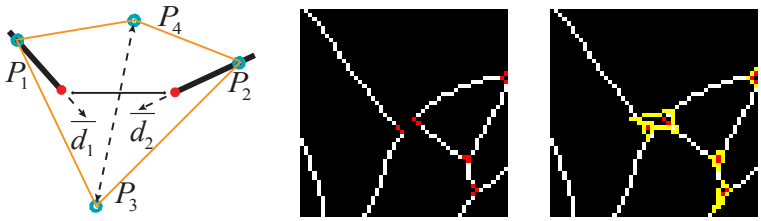

(a) (b) (c)

Figure 4.8: The boundary illustration for neighborhood with size of 2. (a) The theoretical geometry of the boundary. (b) The vessel segments with two 2-pt neighborhoods in the center. (c) The corresponding boundaries shown in yellow.

in Figure 4.9(b) and Figure 4.9(d).

When $|\mathcal{N}_k| > 3$, the boundary is a polygon whose vertices are the vessel pixels p_i such that $|p_i - v_i| = 3$, where $v_i \in \mathcal{N}_k$. Examples of the boundaries for neighborhoods with different sizes is shown in Figure 4.10.

We also limit the size of neighborhoods smaller than 7, based on the observation that the overlapping of three landmarks (bifurcations or crossing points) is extremely rare. Therefore if a merged neighborhood is larger than 6, we undo the merge. When neighborhoods are merged, if both ends of a segment are within the new neighborhood, the segment is removed.

After the construction of neighborhoods, a VPCM is complete which presents the vessel segments and their potential neighbors in term of local neighborhoods. Figure 4.11 (e) shows vessels and their neighborhoods before the merge; Figure 4.11 (f) shows them after the merge. The regions in the red circles show three separate

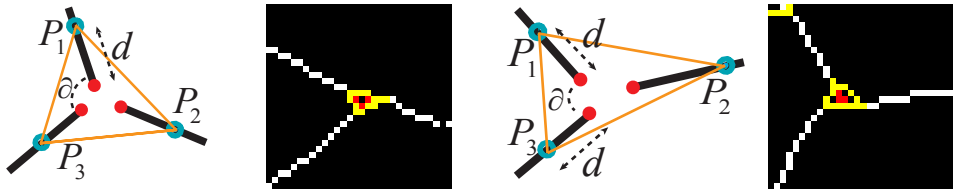

(a) (b) (c) (d)

Figure 4.9: The boundary illustration for neighborhood with size of 3. (a) The first case of boundary construction on theoretical geometric domain. (b) An example of the boundary on the image domain for the first case. (c) The second case of boundary construction on theoretical geometric domain. (d) An example of the boundary on image domain for the second case.

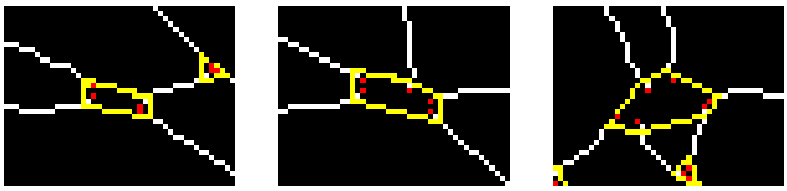

Figure 4.10: Examples of the boundary for neighborhoods with size of 4, 5 and 6 respectively.

neighborhoods, and the corresponding merged 5-pt neighborhood in the final VPCM.

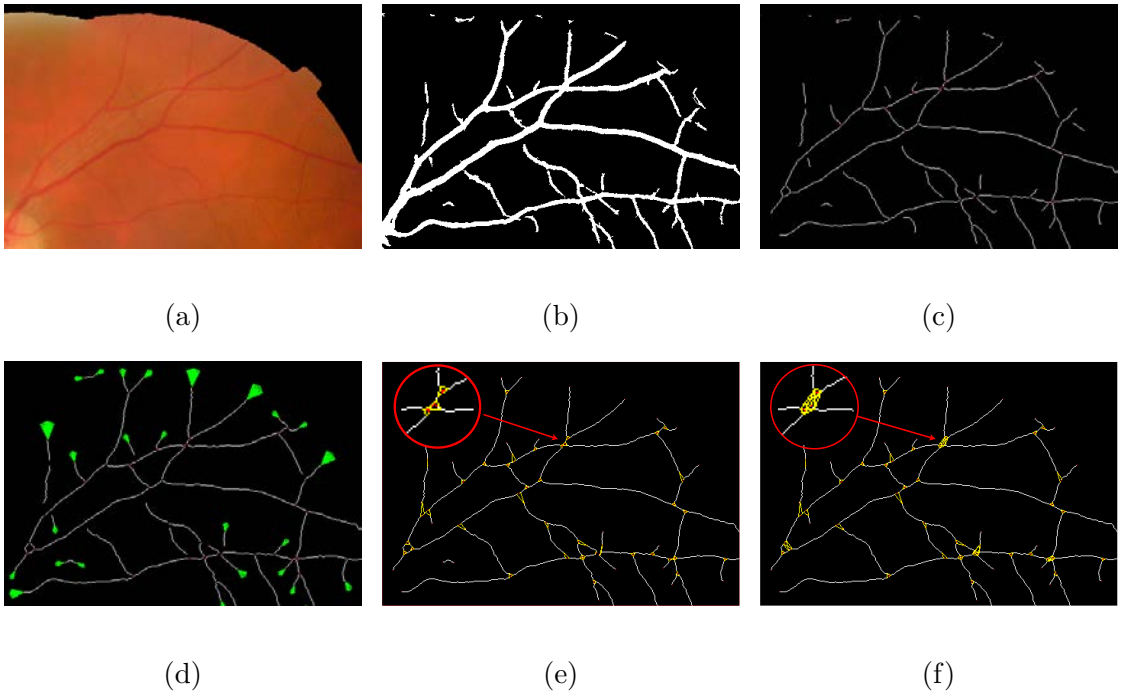

(a) (b) (c)

(d) (e) (f)

Figure 4.11: The construction of VPCM. (a) A portion of fundus image. (b) The vessel segmentation. (c) The vessel skeleton with likely false positive removed. (d) The vessel segments with their extensions in green. (e) The VPCM before the merging of neighborhoods (neighborhoods indicated with yellow boundaries. The enlarged in red circle shows 3 neighborhoods.) (f) The final VPCM (The enlarged in red circle shows 1 neighborhood).

4.2.3 The Separation of the VPCM

4.2.3.1 The Optimization Problem

After we obtain the VPCM, the next stage is to disambiguate this over-connected vessel network into multiple trees with binary labels by finding the true anatomical connectivity between segments. As explained in the beginning of Section 4.2.1, with the two properties of the VPCM, determining the anatomical connectivity within each neighborhood is equivalent to determining the segment types. Here we define a configuration of a neighborhood as a combination of connectivity between segments within the neighborhood, or a combination of segment labels within it, due to the actual equivalence of these two terms. In practice, a neighborhood is a potential landmark, and the configuration is a possible landmark type (i.e., a bifurcation, a crossing point or others).

For each neighborhood, we can locally determine their possible configurations but it is difficult to determine exactly which one is the correct one with only local information. Figure 4.12 shows neighborhoods of size 4 and 5, with some valid potential configurations, and their retinal image equivalents, which shows the difficulty of determining the exact types with local information. However, the global property of the retinal vasculature constrains the choices of the potential configurations; thus we determine types of all landmarks simultaneously using both local and global information. Let $\vec{L}$ denote the labels for all segments in a VPCM. The problem of separating the VPCM is to determine $\vec{L}$ that minimizes Eq. (4.4) with an additional global constraint that the constructed trees contain no cycles. Here a cycle is a set of

connected segments starting and ending at the same segment, with no repetition of other segments.

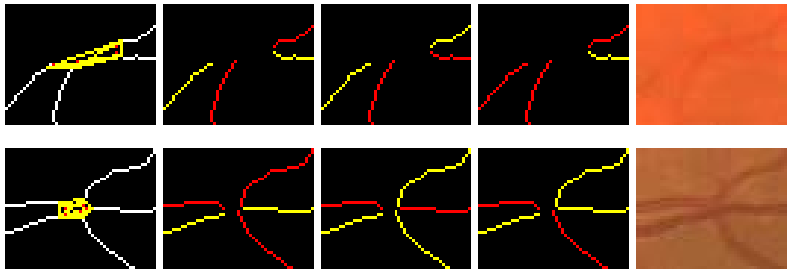

(a) (b) (c) (d) (e)

Figure 4.12: (a) Neighborhoods of size 4 and 5. (b)-(d) Possible configurations. (e) The retinal image parts.

$$E(\vec{L}) = \sum_{k=0}^{K-1} E_{\mathcal{N}}(\vec{l}_{\mathcal{N}_k}) + \beta F(G) \ , \tag{4.4}$$

$$\text{where } E_{\mathcal{N}}(\vec{l}_{\mathcal{N}_k}) = \frac{1}{P(\vec{l}_{\mathcal{N}_k} | \mathcal{N}_k, A_{\mathcal{N}_k})} \tag{4.5}$$

The first term of Eq. (4.4) represents the configuration cost for all neighborhoods, and thus is the local cost. Let l_i reflect the label of segment v_i ($l_i \in [0, 1]$, $l_i = l(v_i) = l(ep_{2i}) = l(ep_{2i+1})$), then $\vec{l}_{\mathcal{N}_k}$ represents the configuration, or the segment labels for the neighborhood $\mathcal{N}_k$. The second term of Eq. (4.4) is a weighted global term which evaluates the topological properties of constructed trees G after segment labels are determined.

For each neighborhood there are multiple possible configurations, and the corresponding cost is computed generally as the reciprocal of its probability, expressed in a general matrix as $A_{\mathcal{N}_k}$ in Eq. (4.5). While we keep the general form of the terms here for describing the overall algorithm, we present the details of how to compute $P(\vec{l}_{\mathcal{N}_k}|\mathcal{N}_k, A_{\mathcal{N}_k})$ and $F(G)$ in Section 4.2.4.

The optimization model is designed not only to choose the best configurations from all possible configurations in a local point of view (the first term), but also to obey the global property of the retinal vasculature (the second term and the global constraint). To solve this problem, we divide the VPCM for an image into several independent sub-VPCMs to solve them individually, without loss of generality. Since the OD is masked out, separation into sub-VPCMs is easily done with breadth-first search (BFS). Small sub-VPCMs which are far away from the OD (i.e., trees with fewer than 40 centerline pixels and for which the nearest distance to the OD is larger than than twice of the OD radius) are removed from further analysis due to their insignificance in clinics. The difficulty of the optimization problem stems from the global constraint, which is related to the complexity of a VPCM, and thus we categorize VPCMs into three types:

- A simple VPCM: a VPCM which has one segment (see Figure 4.13(b)).
- An acyclic VPCM: a VPCM which has more than one segment, but without cycles (see Figure 4.13(c)).
- A cyclic VPCM: a VPCM which has one or more cycles (see Figure 4.13(d)).

The simple VPCM is only a single segment so we only need to focus on the

other two, altogether referred as complex VPCMs. Because of the difficulty of this problem with cyclic VPCMs, we design a graph-based algorithm to approximate an optimal solution. We first transfer a complex VPCM into a special graph which incorporates the global constraint, and we use it to find candidate solutions with low costs of the first term of Eq. (4.4). These candidate solutions are then evaluated to generate the final solution by combining the global cost $F(G)$, which is the second term of Eq. (4.4).

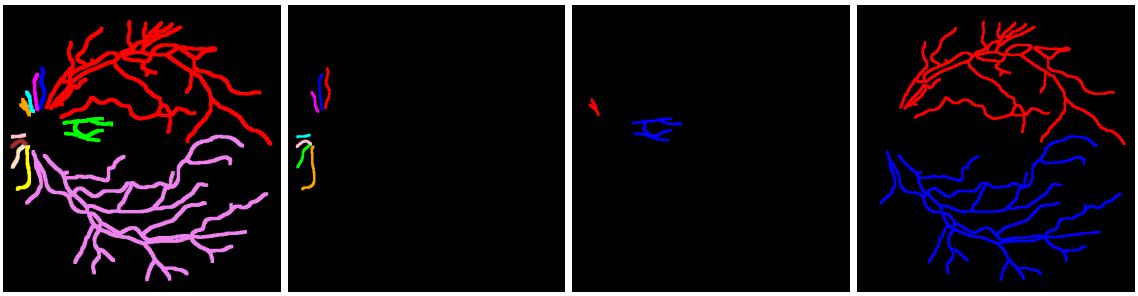

(a) (b) (c) (d)

Figure 4.13: (a) Independent VPCMs in different colors. (b) Simple VPCMs in different colors. (c) Acyclic VPCMs in different colors. (d) Cyclic VPCMs in different colors (All centerlines are thickened for better visualization).

4.2.3.2 The Graph Model

In the proposed graph model, each vertex n_i represents a segment v_i, and each edge e_{ij} represents a relation between segments v_i and v_j within a neighborhood. For

each neighborhood, with $|\mathcal{N}| = n$, $n-1$ edges are built to connect the n vertices as a linear tree such that the starting and ending vertices have degree of 1, and other interior vertices have degree of 2. Here the concept of a cluster $\mathcal{C}_k$ is introduced in the graph corresponding to the neighborhood $\mathcal{N}_k$ on the VPCM, which is a set of edges generated by the vessel ends within one neighborhood. If in the image domain, $ep_i, ep_j \in \mathcal{N}_k$, and there is an edge e_{ij} constructed in graph domain, then $e_{\lfloor i/2 \rfloor \lfloor j/2 \rfloor} \in \mathcal{C}_k$. Figure 4.14(a) shows an example of how a 3-pt $\mathcal{N}$ and a 4-pt $\mathcal{N}$ are transformed to clusters in the graph domain respectively. Using this cluster-based transformation, a VPCM is transferred into a planar graph. Figure 4.14(b) shows a virtual VPCM with four neighborhoods transferred to a graph. In this example, four neighborhoods in the image domain correspond to the four clusters in the graph, whose edges are labeled in different colors. Figure 4.15 shows the transferred graph from the VPCM in Figure 4.11.

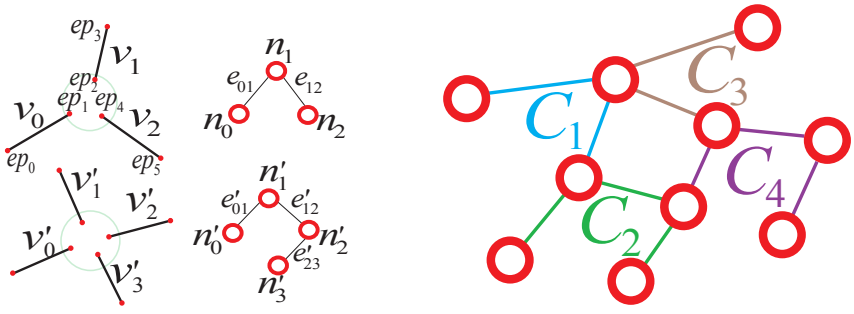

(a) (b)

Figure 4.14: (a) Neighborhoods transferred into clusters. (b) A graph transferred from the VPCM in Figure 4.2.

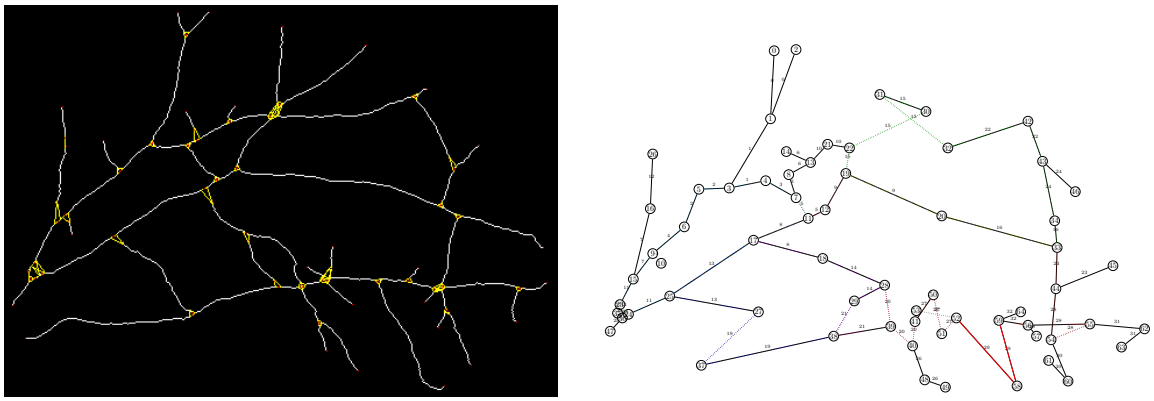

(a) (b)

Figure 4.15: (a) The VPCM from Figure 4.11. (b) The corresponding graph.

In the graph, each vertex needs to be labeled in one of two colors, corresponding to a vessel segment being assigned one of two types; each edge is associated with one of two constraints: equality or inequality, which simulates the connectivity between segments on image domain. The equality constraint dictates the two vertices connected by the edge must be in the same color; the inequality constraint dictates they must be in different colors. Within each cluster, a combination of edge constraints is equivalent to a two-color scheme on vertices, which corresponds to a configuration for the neighborhood. Also the costs of configurations for each neighborhood are attached to the corresponding combinations of edge constraints for clusters.

Corresponding to the VPCM, vertex labelings and edge constraints for one cluster is mutually inferable. Figure 4.16 shows the cluster and its edge constraints and vertex labelings, corresponding to the neighborhood of size 4 in Figure 4.12.

Specifically, Figure 4.16(a) shows the segments with local indexes and Figure 4.16(b) shows its corresponding cluster. Figure 4.16(c)-(e) show the three configurations in the graph corresponding to those on the VPCM. Figure 4.16(c) indicates v_0 and v_2 are the same type and thus connected, v_1 and v_3 are the other type, meaning the neighborhood represents a crossing point. Figure 4.16(d) indicates v_0 and v_1 are the same type thus connected, v_2 and v_3 are the other type, meaning the neighborhood represents the case of two vessels being close. Figure 4.16(e) indicates v_0, v_1 and v_2 are the same type and connected, v_3 is another type and disconnected with them, meaning v_0 v_1 and v_2 form a bifurcation, and v_3 is falsely connected to it.

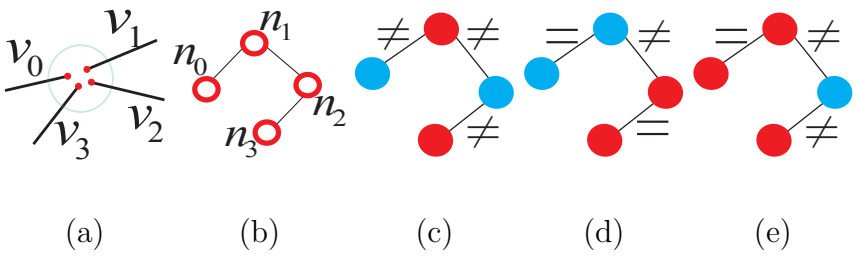

Figure 4.16: (a) The neighborhood with local indexes of segments. (b) The cluster. (c) - (e) Three configurations corresponding to three landmark types for the neighborhood of size 4 in Figure 4.12.

By this transformation, the optimization problem in the VPCM then can be transferred on the graph to the following problem: find a combination of edge constraints for each cluster, which also equals to the vertex color assignment, under three

conditions, and meanwhile have the minimal cost in Eq. (4.4). The three conditions are:

1. The number of inequality edges on each cycle must be even.
2. The number of inequality edges on each cycle must be larger than zero.
3. The inequality edges on each cycle cannot come only from one cluster.

Here a cycle on the graph is a set of connected vertices starting and ending at the same vertex, and without repetition of other vertices. The first condition guarantees that there is a feasible edge assignment on the graph such that vertices can be colored using two colors. The second and third conditions guarantee that the solution on the graph can be transferred to a feasible solution in the VPCM, which are multiple trees with binary labels.

We define a conflict cycle when the edges on the cycle violate any of the three conditions, and a solution on the graph without a conflict cycle as a feasible solution, and a solution with conflict cycles as an infeasible solution. To find the optimal solution, besides the feasibility, we also need the cost in Eq. (4.4) to be minimal.

Due to the difficulty of this problem when there are cycles in the graph, we propose a meta-heuristic algorithm to find a near-globally optimal solution, illustrated in Figure 4.17. Meta-heuristic algorithms are a type of common algorithms in the optimization field which give a near-optimal solution for difficult problems within a reasonable amount of time. The first step of the algorithm is to find a set of feasible candidate solutions with low costs of the first term of Eq. (4.4). Then these candidate solutions are evaluated with the second term of Eq. (4.4) and the one

with the minimum cost of Eq. (4.4) is the final solution. At the first step, we develop different algorithms to generate the candidate solutions depending on whether a graph has cycles or not. If there is no cycle, which only happens when the graph is small, all solutions are feasible; thus we consider all solutions as candidate solutions. If there is at least one cycle, which is the core of the problem, we use a heuristic algorithm to generate feasible solutions with low costs of the first term of Eq. (4.4), which is explained in detail in the following section.

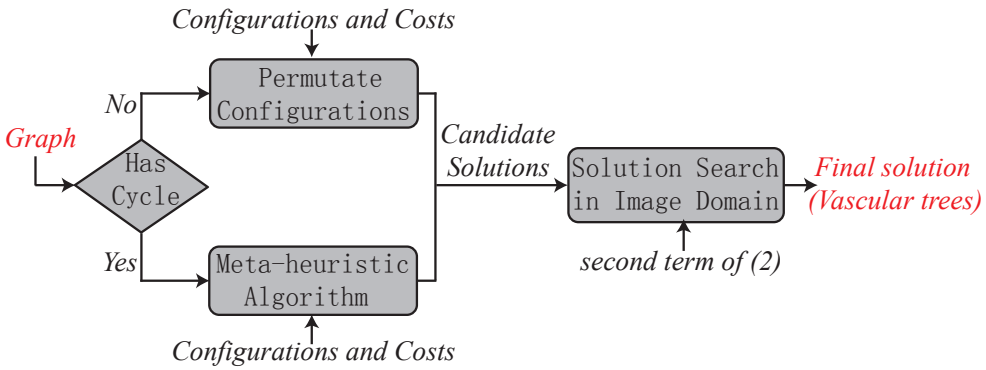

Figure 4.17: A concise flowchart of the meta-heuristic algorithm.

4.2.3.3 The Heuristic Algorithm

Here we denote a solution on the graph domain i.e., the choices of edge constraints, as s. As is common in many meta-heuristic algorithms, the overall idea is to maintain a candidate solution pool, with candidate solutions generated as in Algorithm 4.2. If there are conflict cycles, the algorithm permutes the edge constraints

to reduce them. The solution pool is updated during every conflict cycle reduction to reduce at least one conflict cycle. The algorithm stops when enough feasible solutions are generated, or the iteration number reaches the maximum limit.

To avoid the trap of local optima, we generate different seed solutions to feed into Algorithm 4.2. Seed solutions are generated from the solution with the lowest local cost, which might not be feasible in most cases, with random permutation of configurations of random clusters. For each seed solution, Algorithm 4.2 outputs a pool of candidate solutions, and the final candidates are the union of all pools.

For Algorithm 4.2, it starts from a seed solution, and checks for conflict cycles first. This is done by detecting a cycle basis first and then checking each cycle of the basis. A cycle basis is a minimal set of cycles that any cycle can be written as a union of the cycles in the basis [151]. A cycle basis is found using BFS, and the conflict cycles are detected by checking the three conditions in Section 4.2.3.2 (implemented as FindConflictCycle(s, B) in Algorithm 4.2). If a solution contains conflict cycles, the algorithm randomly chooses a conflict cycle to resolve. If there are adjacent conflict cycles, they have a higher priority to be chosen.

Within Algorithm 4.2, permutateEdgeConstraint(s, C, m) (Algorithm 4.3) is the component to permute the edge constraints of clusters to remove conflict cycles, and to generate offspring solutions. The algorithm iterates edges on the conflict cycle and finds their corresponding clusters. All the potential configurations of these clusters are sorted based on their costs. A random Gaussian noise is added during the sorting to enlarge the search region and prevent being trapped in local minima. The

Algorithm 4.2 Algorithm for finding candidate solutions, given a graph G with cycle basis B, l (number of feasible solutions required), m, initial sol t, and $iter$ (maximum iteration number)

Initialize sol pool $\mathcal{S}$ with t, initialize feasible sol pool $\mathcal{F} \leftarrow \emptyset$

while $|F| < l$ & $i < iter$ **do**

Initialize sol pool $\mathcal{S}'$

for each solution $s \in \mathcal{S}$ **do**

$C \leftarrow$ FindConflictCycle(s, B)

if $|C| = 0$ **then**

put s into $\mathcal{F}$ if $s \notin \mathcal{F}$

else

sol pool $\mathcal{N} \leftarrow$ permutateEdgeConstraint(s, C, m) (see Algorithm 4.3)

for each solution n in $\mathcal{N}$ **do**

put n in $\mathcal{F}$ if it is feasible; otherwise put n in $\mathcal{S}'$ if $n \notin \mathcal{S}'$

end for

end if

end for

$\mathcal{S}' \leftarrow \mathcal{S}'$, $i \leftarrow i + 1$

end while

if $|\mathcal{F}| = 0$ **then**

$\mathcal{F} \leftarrow \mathcal{S}'$

end if

return $\mathcal{F}$

algorithm starts by changing the configuration based on their costs one at a time, and proceeds to check if the number of conflict cycles are reduced. Here m is the number of offspring required, and j controls the relaxation of the cycle reducing criteria. If there are only a couple of solutions with less cycles, this indicates that the algorithm might meet a local minimum. To escape from the local minimum and increase the search space, the algorithm needs to generate offspring that have more cycles than the current solution.

When Algorithm 4.2 cannot generate enough feasible solutions, it stops when the iteration number hits the limit. In an extreme case, there might not be feasible solutions. This might happen when there are false vessels in the VPCM that form a false cycle, or when vessels of the same type form a cycle mistakenly in the fundus images. In these cases the algorithm generates the most favorable infeasible solutions, which are solutions with the least number of cycles and lower costs.

Besides the algorithm designed for the normal case, we also propose a back-up algorithm for abnormal cases when Algorithm 4.2 fails to find a feasible solution. This would happen when some assumptions of the VPCM are violated during the construction. For example when there are false vessels in the VPCM, a cycle might be inevitable in the vasculature, thus in the graph. Also if a neighborhood is over-expanded, it might include vessels with the same type that should not be connected anatomically. If these cases happen, the retinal vasculatures generated inevitably contain cycles, which cannot be considered as trees. To deal with the inevitability of infeasible solution on the graph, a back-up algorithm is proposed based on Algo-

Algorithm 4.3 permutateEdgeConstraint given s, C, m

Initialize sol pool $\mathcal{S} \leftarrow \emptyset$, $i \leftarrow 0$

while $|\mathcal{S}| < m$ **do**

$c \leftarrow$ CycleSelection(C)

find clusters on c, $k \leftarrow 0$, $l \leftarrow 0$

for $j \leftarrow 0$; $j < m/|C|$ **do**

select a configuration $config$ based on costs added with random noise

$s' \leftarrow$ UpdateSolution(s, $config$)

$C' \leftarrow$ FindConflictCycle(s', B)

if $C' = C$ or $|C'| \geq |C| + l$ **then**

disregard s', $k \leftarrow k + 1$

else

put s' in $\mathcal{S}$ if $s \notin \mathcal{S}$

$j \leftarrow j + 1$, $k \leftarrow 0$

end if

if $k \geq |m|$ **then**

$k \leftarrow 0$, $l \leftarrow l + 1$

end if

end for

$i \leftarrow i + 1$

end while

return $\mathcal{S}$

rithm 4.2 which tolerates the conflict cycles in the graph. The back-up algorithm is summarized in Algorithm 4.4. Basically we modify Algorithm 4.2 to allow the final solution having a certain number of conflict cycles, which is controlled by the parameter l_c. The backup algorithm (Algorithm 4.4) takes this modified Algorithm 4.2 as a kernel to generate a pool of solutions. If there is no solution generated, the the parameter l_c is iteratively increased until there are solutions generated.

Algorithm 4.4 Back-up algorithm to generate solutions, given a graph G with cycle basis B, l (number of feasible solutions required), m, initial sol t, and $iter$ (maximum iteration number)

---

initialize feasible sol pool $\mathcal{F} \leftarrow \emptyset$

while $|F| < 1$ **do**

$F \leftarrow$ GenerateSolutionPool(G, B, l, m, t, $iter$, l_c)(Algo. 4.5)

$l_c \leftarrow l_c + 1$

end while

return $\mathcal{F}$

4.2.4 Cost Function Design

The costs represented by Eq. (4.4) is essential for the proposed algorithm. The first term reflects the costs of various possible configurations for each neighborhood, which are calculated by using local vessel features and some global features. The

Algorithm 4.5 GenerateSolutionPool, given a graph G with cycle basis B, l (number of feasible solutions required), m, initial sol t, and $iter$ (maximum iteration number), conflict cycle limit l_c

Initialize sol pool $\mathcal{S}$ with t, initialize feasible sol pool $\mathcal{F} \leftarrow \emptyset$

while $|F| < l$ & $i < iter$ **do**

Initialize sol pool $\mathcal{S}'$

for each solution $s \in \mathcal{S}$ **do**

$C \leftarrow$ FindConflictCycle(s, B)

if $|C| \leq l_c$ **then**

put s into $\mathcal{F}$ if $s \notin \mathcal{F}$

else

sol pool $\mathcal{N} \leftarrow$ permutateEdgeConstraint(s, C, m)(Algo. 4.3)

for each solution n in $\mathcal{N}$ **do**

put n in $\mathcal{F}$ if it is feasible; otherwise put n in $\mathcal{S}'$

end for

end if

end for

$\mathcal{S}' \leftarrow \mathcal{S}'$, $i \leftarrow i + 1$

end while

return $\mathcal{F}$

second term reflects the costs of the constructed trees, which is calculated after the candidate trees are generated.

4.2.4.1 Feature Extraction

First we introduce the types of vessel features which are used to calculate the costs, which are:

- the vessel end point direction,
- the vessel width,
- the vessel profile intensities, and
- the vessel dominant orientation.

The vessel end point direction is a pair of directions along the segment at both end points, with the positive direction being away from the segment, represented as a pair of unit vectors. Principal Component Analysis (PCA) is used to calculate the direction with the first $n = 15$ pixels starting from each end of the segment.

The feature of vessel width includes the absolute width and the relative width, which are the average vessel width of a segment and its relative average width compared to others. The absolute width is calculated using Xu's method [152] and the relative width is a 4-scale integer representing the vessel width compared to the quartiles of the vessel widths from the whole image.

The vessel profile intensities are a set of average intensities along the vessel cross section on a set of color channels. To reduce the effect of potential errors introduced during the measurement of vessel width, we use the average intensity within

the center half of the vessel width. Intensities are collected in six channels, including red, green and blue in RGB, intensity channel (I) in HSI, and L and b channels in Lab space. Before the calculation, to remove the luminance imbalance, single-channel images are subtracted by their background images and then normalized. The background image is obtained by filtering the original image with a large mean filter. An example of the balanced images is shown in Figure 4.18, and for the fundus image in Figure 4.20.

The vessel dominant orientation is the expected direction of the blood flowing via a vessel segment, based on its geometric and topological properties. Although the blood flows in reversed directions in arteries and veins, for the purpose of this feature, we define all dominant orientations using an arterial convention where blood flows from the OD to the periphery of an image and the fovea. A binary status $flow_i$ is attached to each segment v_i, representing if the dominant orientation is determined for v_i or not. Appendix B contains the details of the computations to determine the vessel dominant orientation. Then the dominant orientation feature is transferred to the end point level by giving one of three labels to each point: head (h), tail (t) or unknown (u). These labels of end points are used to calculate costs for potential configurations of each neighborhood. If the dominant orientation is determined for v_i, its end points are labeled as a h and a t, representing the head and the tail of v_i. The head and the tail for a segment are determined in a way that blood flows from the tail to the head. If the dominant orientation cannot be determined, both end points are labeled as u, which means end points are unknown. In the following,

head, tail and unknown are indicated by the symbols h, t and u respectively. With this rule and the two assumptions about the neighborhood defined at the beginning of Section 4.2, some constraints can be inferred within each neighborhood:

- For any neighborhoods, blood cannot flow from a h to another h.
- For any neighborhoods larger than 2, there must be at least one h and at most 2 h.

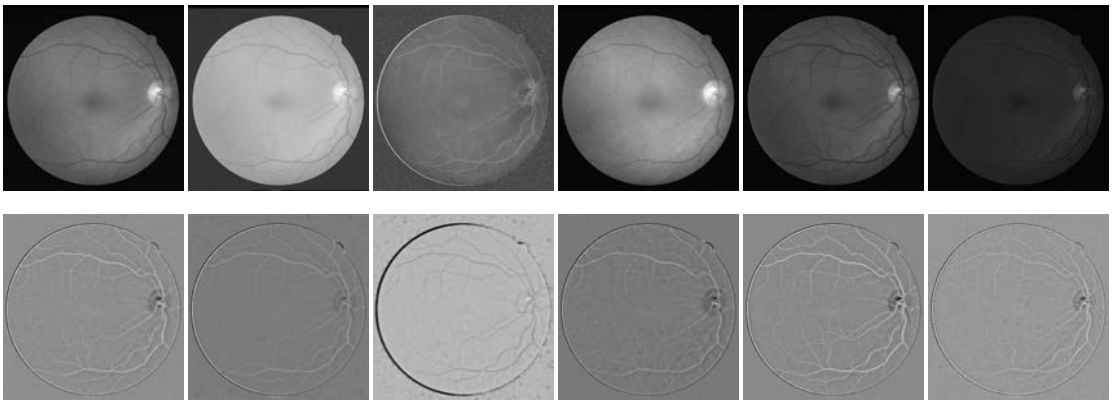

Figure 4.18: First row: images in R, G, B, I, L and b channels. Second row: images after the imbalance removal and intensity normalization.

4.2.4.2 Configurations and Costs of Local Neighborhoods

A configuration for a neighborhood, denoted as ϕ, represents the separation of end points within the neighborhood into two categories. Denoting all the possible configurations for a neighborhood as $|\Phi|$, and the number of neighborhoods in a VPCM as l, then the solution space is $O(|\Phi|^l)$. It is very expensive to locate the

optima in such a big space thus we shrink the solution space by decreasing $|\Phi|$.

Logically $|\Phi| = 2^{|\mathcal{N}_k|-1}$, with the constraint that $1 < |\mathcal{N}_k| < 7$. however when $|\mathcal{N}_k| > 3$, many configurations can be pre-excluded by checking the labels of end points. Specifically when $|\mathcal{N}_k| = 5$, we require that there must be 2 heads and 3 tails; when $|\mathcal{N}_k| = 6$, there must be 2 heads and 4 tails. With the constraints that heads have to be separated, and 1 head cannot connect to more than 3 tails, when $|\mathcal{N}_k| = 5$, $|\Phi| = 8$; and when $|\mathcal{N}_k| = 6$, $|\Phi| = 14$. Then the probabilities or costs of all possible configurations are calculated using different algorithms designed for neighborhoods of different sizes using features explained in Section 4.2.4.1.

First, for better description, we use the labels of end points to denote the members of one neighborhood. For example, a neighborhood with one head, two tails, and one unknown is denoted as $\mathcal{N}_k = \{h, t_1, t_2, u\}$. And a configuration is denoted as a subset of connected end points. So in the case of $\mathcal{N}_k = \{h, t_1, t_2, u\}$, a configuration of the head being connected with both tails is denoted as $\phi = \{h, t_1, t_2\}$. And due to the duality of the connection or the labels, it can also be expressed using the complementary subset, thus $\phi = \{h, t_1, t_2\} = \{u\}$.

When $|\mathcal{N}_k| = 2$, there are two configurations, two end points are either connected, or disconnected. The vessel dominant orientation and the vessel end point direction are used to determine the costs of them. First, if both end points are heads or tails, there is only one configuration, that they are disconnected, and the cost is set to be an extremely small number, here -3.0; Otherwise, end point directions are used to determine the configurations and costs. The cost of them being connected

is calculated by Eq. (4.6) and the cost of them being disconnected is calculated by Eq. (4.7), where $\mathbf{o_1}$ and $\mathbf{o_2}$ are the directions of the two end points.

$$c_0 = -0.1 \times (1 - \frac{\cos\alpha + 1}{2}) \tag{4.6}$$

$$c_1 = -0.1 \times \frac{\cos\alpha + 1}{2} \tag{4.7}$$

$$\text{where, } \cos\alpha = \frac{\mathbf{o_1} \cdot \mathbf{o_2}}{|\mathbf{o_1}| \cdot |\mathbf{o_2}|} \tag{4.8}$$

When $|\mathcal{N}_k| = 3$, there are four potential configurations logically. Here vessel dominant orientations and end point directions are used. Specifically after the determination of vessel dominant orientations, there are only three cases of how many heads, tails or unknowns in the neighborhoods, and different algorithms are designed to generate possible configurations and corresponding costs.

1. For the case of one head and two tails ($\mathcal{N}_k = \{h, t_1, t_2\}$): we limit the potential configurations to only three cases, $\Phi = \{\phi_1, \phi_2, \phi_3\}$, where $\phi_1 = \{h, t_1, t_2\}$, $\phi_2 = \{h, t_1\}$ and $\phi_3 = \{h, t_2\}$. The costs are calculated using the end point direction vectors. For ϕ_2 and ϕ_3, their costs are the cosines of the angles between the direction vectors of two connected end points. For ϕ_1, the cost is the sum of the two cosines of the angles between the direction vectors of the head and two tails.

2. For the case of two heads and one tail ($\mathcal{N}_k = \{h_1, h_2, t\}$): we limit the potential configurations to only two cases. $\Phi = \{\phi_1, \phi_2\}$, where $\phi_1 = \{h_1, t\}$, $\phi_2 = \{h_2, t\}$. The costs for ϕ_1 and ϕ_2 are the cosines of the angles between the directions of

two connected end points.

3. For the case of one head, one tail and one unknown ($\mathcal{N}_k = \{h, t, u\}$): four cases are allowed, $\Phi = \{\phi_1, \phi_2, \phi_3, \phi_4\}$, where $\phi_1 = \{h, t, u\}$, $\phi_2 = \{h, t\}$, $\phi_3 = \{h, u\}$ and $\phi_4 = \{u, t\}$. The costs for ϕ_2, ϕ_3 and ϕ_4 are the cosines of the angles between the directions of two connected end points. For ϕ_1, the cost is the sum of the two cosines of the angles between the direction vectors of the head and the tail, and the head and the unknown.

We next introduce how to calculate the costs for configurations when $|\mathcal{N}_k| = 5,\ 6$ (the costs for $|\mathcal{N}_k| = 4$ will be discussed last). When $|\mathcal{N}_k| = 5,\ 6$, since there are 2 heads and the rest are tails, the same strategy is adapted. For all the configurations, three types of costs are calculated independently using the vessel width, profile intensities and end point directions respectively, denoted as P_w, P_i and P_d. Then they are combined together to obtain the final cost P_ϕ. Specifically, it is the negative of the multiplication of the three costs in Eq. (4.9). Then configurations with the first 6 lowest costs are preserved for $|\mathcal{N}_k| = 5$, and configurations with the first 8 lowest costs are preserved for $|\mathcal{N}_k| = 6$.

$$P_\phi = -P_w P_i P_d \tag{4.9}$$

For P_w, we utilize the fact that the width of parent segment is larger than the width of any children segments. First we use the relative width to eliminate some impossible configurations if $q_p - q_c < -1$, where q_p is the relative width of the parent segment (one providing the head), and q_c is the relative width of the thickest child

segment (one providing the tail). Then we calculate P_w using Eq. (4.10), where w_p and w_c are the absolute widths of the parent and child segments respectively introduced in Section 4.2.4.1.

$$P_w = \log(w_p - w_c + 1.5) \tag{4.10}$$

For P_i, we evaluate the cost of every child segment being connected to one parent over another parent using intensity information. Specifically, for child segment v_c, the cost p_c is calculated using Eq. (4.11), where $\vec{I_c}$ is its intensity vector, $\vec{I_{pc}}$ is the intensity vector of the parent it connects, and $\vec{I_{pd}}$ is the intensity vector of the parent it disconnects. For a configuration, the P_i is the multiplication of the p_c of three child segments.

$$p_c = |\vec{I_c} - \vec{I_{pd}}|/|\vec{I_c} - \vec{I_{pc}}| \tag{4.11}$$

For P_d, we make three rules to model the angles between the parent segment and its children segments. If a parent segment has only one child, then the two segments should be as aligned as possible. If a parent segment has two children, then the two children segments should also be connected to the parent in a balanced way. If a parent segment has three children, also the three children segments should be connected to the parent in a balanced way.

When $|\mathcal{N}_k| = 4$, there are eight potential configurations logically. Since there might be unknowns in this type of neighborhood, three different algorithms are designed for different cases. The first case is when there are 2 heads and 2 tails. In this case there are only 4 possible configurations, and we use the same method for

$|\mathcal{N}_k| = 5,\ 6$ to calculate the costs for them.

The second case is when there is 1 head and 3 tails. In this case 3 tails are supposed to connect to the head, unless the neighborhood is near the OD. When it is near the OD, we assume 1 tail should be a root, which should be separated from the head. Thus there are 4 configurations: $\Phi = \{\phi_1, \phi_2, \phi_3, \phi_4\}$, where $\phi_1 = \{h, t_1, t_2, t_3\}$, $\phi_2 = \{h, t_1\}$, $\phi_3 = \{h, t_2\}$, and $\phi_4 = \{h, t_3\}$. The cost of ϕ_1 is given in Eq. (4.12), where p_D is a distance factor, v_d is the distance of segment centroid to the OD and r_{OD} is the radius of the OD. The cost of three other cases is given in Eq. (4.13), where $I_{ri}, i \in 1, 2, 3$ is the difference of mean intensity between the only separated segment and the three connected segments; $I_{ij}, i, j \in 1, 2, 3$ and $i \neq j$ is the difference of mean intensity between the three connected segments.

$$p_\phi = p_D - 3 \text{ where, } p_D = \frac{r_{OD}}{2 \times v_d} \tag{4.12}$$

$$p_\phi = p_D \frac{I_{r1} I_{r2} I_{r3}}{I_{12} I_{13} I_{23}} - 3 \tag{4.13}$$

The third case is when there is only 1 head, and the number of unknowns is larger than 0. In this case we first determine if there is another head. If there is not, then it belongs to the second case; if there is another head, then it belongs to the first case. Here end point directions are used to determine if there is another head. Generally if the direction of the segment with an unknown has a small angle with the direction of the segment of the determined head, and the segment with the unknown aligns well with another segment that is not the head, then this unknown is a head.

4.2.4.3 The Global Costs

The candidate solutions generated by Algorithm 4.2 might not fit the topology of the retinal vasculature since it only uses the first term of Eq. (4.4). A set of global costs are thus imposed to select the optimal solution which fit the topology of the vasculature best, which is composed of three components in Eq. (4.14). For our experiment β in Eq. (4.4) is set as 1.

$$F(G) = D(G) + B(G) + C(G) \tag{4.14}$$

The first term is the sum of the distances of every constructed tree t to the OD in Eq. (4.15), which is the Euclidean distance from the nearest pixel of a tree to the center of OD.

$$D(G) = \sum_{t \in G} d(t) \tag{4.15}$$

The second term is the bifurcation evaluator at each bifurcation in Eq. (4.16). Here b represents each bifurcation; θ_1 and θ_2 are the angles between two children vessels and the parent vessel for each bifurcation; and l_1 and l_2 are lengths of children vessels.

$$B(G) = \sum_{t \in G} \sum_{b \in t} h(b) \text{ where, } h(b) = l_1 e^{\frac{\pi}{2} - \theta_1} + l_2 e^{\frac{\pi}{2} - \theta_2} \tag{4.16}$$

The third term $C(G)$ is the consistency of the vessel dominant orientation. After trees are constructed from the VPCM, the vessel dominant orientations are

determined for all segments, and a penalty is imposed for the segments whose dominant orientations are opposite compared to the VPCM. The penalty is the sum of the lengths of these segments.

4.2.5 A/V Classification

After separating complex VPCMs into multiple trees of two types, with each separated tree being referred to as an overlapping tree, the next step is to determine which trees (including those from simple VPCMs) are arterial and which are venous. For overlapping trees, the most difficult part is completed as part of the separation of complex VPCM into trees with two types, so we now are able to rely on relative differences between the overlapping trees to help in the final A/V classification. However, for simple VPCMs (each of which is a single tree, by definition), we need to decide its A/V category independently, which can to be more difficult. Here, for consistency, the simple VPCMs are referred to as independent trees, compared to the overlapping trees which are generated from complex VPCMs. In both cases, we use a pixel-based classification method to help make the arterial/venous determination.

In particular, the probability of each centerline pixel being arterial or venous is obtained first. The algorithm is similar to the machine-learning method proposed by Niemeijer et al. [126]. Briefly, 31 features regarding vessel intensity are extracted and 19 features are selected as the final features. The 19 features include the vessel width and 18 intensity-related features on the 6 channels mentioned in Section 4.2.4.1: the average and standard deviation of vessel intensity transectionally, and the ratio of

intensities inside and outside of the vessel profile. The intensity inside is the average vessel intensity, and the intensity outside is the average intensity between the vessel boundary and twice the width away from the boundary. Here a Support Vector Machine (SVM) with the radial basis function kernel is used as the classifier, which is trained on the data of 48 images from our previous work [146]. The dataset is evenly separated into two subsets to select these final features.

After each centerline pixel is classified, overlapping trees and independent trees are classified into A/V trees using different strategies.

4.2.5.1 Overlapping Tree Classification

For overlapping trees from each VPCM, the probability of each type of trees being arterial and venous are the normalized summation of all its centerline pixel probabilities. Since they are already separated into two types, the one with higher arterial probability is defined as the arterial tree and the other is defined as venous tree.

4.2.5.2 Independent Tree Classification

For each independent tree, two algorithms are developed to determine the types of trees. The first one is to only use the probability by the pixel classification. The second one is to use the pixel classification combined with geometric information. For the first one, a probability is obtained for each tree as the normalized summation of its centerline pixel probabilities. If the tree probability is larger than 0.5, it is defined as arterial; otherwise it is defined as venous.

For the second algorithm, geometric information is combined with the probability obtained in the first algorithm. The geometric information is based on the general rule that arteries and veins tend to appear alternatively around the OD. This phenomenon is especially strong in the region on the opposite of the fovea with respect to the OD, where most of independent trees appear (see Figure 4.19). To utilize this phenomenon, we first assume that there are overlapping trees and they are classified into A/V trees. We use these classified A/V trees as neighbors to constrain the types for these independent trees.

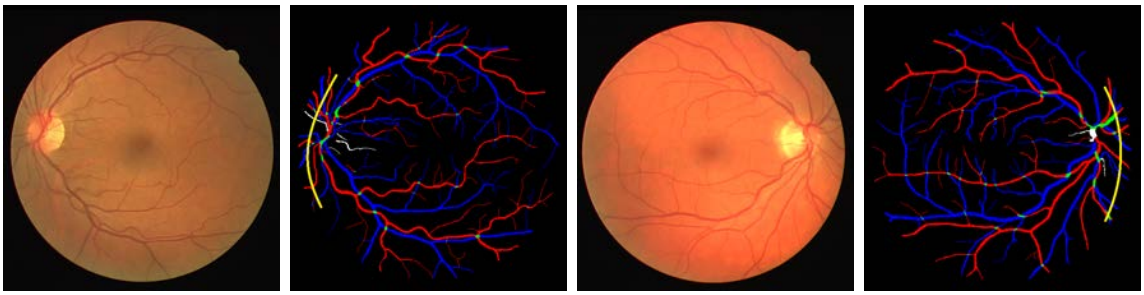

(a) (b) (c) (d)

Figure 4.19: (a) A fundus image. (b) The A/V ground truth of (a). (c) A fundus image. (d) The A/V ground truth of (c). Arteries and veins typically alternate along the yellow curve.

First of all, we calculate an angle for each tree representing the polar position with respect to the OD. The angle is the average of angles of vessel centerlines with respect to the OD. Then all trees are ranked and sorted using their angles and the

independent trees are separated into groups such that for each group there are no classified A/V trees between any two independent trees. In each group, we find the closest A/V trees on both end of each group of independent trees, named as the lower neighboring A/V tree and the upper neighboring A/V tree. Each group of independent trees are classified together with the information of neighboring A/V trees, which is modeled as an optimization problem. Here we assume there are n independent trees in a group, denoted as $T_1...T_n$, with the lower neighboring tree and the upper neighboring tree denoted as O and U respectively. So the optimization is to find the labels of each tree $l_i = \{0, 1\}$, which minimizes the cost C given by Eq. 4.17.

$$\begin{aligned} C(\vec{L}) = & \sum_{i=1}^{n} \frac{1}{P(T_i|l_i)} - \sum_{i=1}^{n-1} D(T_i, T_{i+1})(l_i - l_{i+1})^2 \\ & - D(T_1, L)(l_1 - l_L)^2 - D(T_n, U)(l_n - l_U)^2 \\ \text{where } D(T_i, T_{i+1}) = & \sum_{c \in T_i} \sum_{p \in T_{i+1}} \frac{1}{E(c,p)^2} \end{aligned} \tag{4.17}$$

Here l_i represent the independent tree T_i being either artery or vein; $P(T_i|l_i)$ is the probability of tree T_i being artery or vein given by the pixel-classification method. Besides the first term, the rest three terms describe the phenomenon that two close trees are of different types. $D(T_i, T_{i+1})$ is a weight factor represented by a function of the distance between two trees. Here $E(c, p)$ is the Euclidean distance between two vessel centerline pixels.

So solve this problem, since usually n is small, usually around 3, and seldom larger than 5, the optimal solution can be easily obtained by simply iterating through all combinations of the labels of trees.

4.3 Experiments and Results

4.3.1 Data

Two datasets are used to test the performance for the proposed method. First a dataset RITE (Retinal Images vessel Tree Extraction) is generated and made public which is based on a well-known public available dataset DRIVE [4]. To build the dataset, two experts corrected the vessel reference standard on nine images from DRIVE, and then added arterial and venous labels. The RITE contains 40 sets of images, equally divided into a test subset and a training subset, as the DRIVE does. Each set contains a fundus images, inherited from DRIVE, a vessel reference standard and a A/V reference standard. For the test subset, the vessel reference standard is the vessel reference standard named 2nd_manual in DRIVE. For the training subset, the vessel reference standard is a modified version of the vessel reference standard named 1st_manual in DRIVE. The A/V reference standard is generated by labeling each vessel pixel, with one of four labels on the vessel reference standard: artery (A), vein (V), overlap (O), and uncertain (U), encoded by four colors, respectively: red, blue, green, and white. An example of a RITE fundus image, its vessel reference standard and A/V reference standard are shown in Figure 4.20. RITE is available at http://www.medicine.uiowa.edu/eye/RITE/.

Another dataset is 48 color mosaiced fundus images, referred as the Mosaic dataset in this thesis, which is used in our previous work [146] (Figure 4.21(a)). Since there is no vessel reference for this dataset, the A/V reference is generated by manually labeling the generated VPCM image into a A/V skeleton image (Figure 4.21(c)).

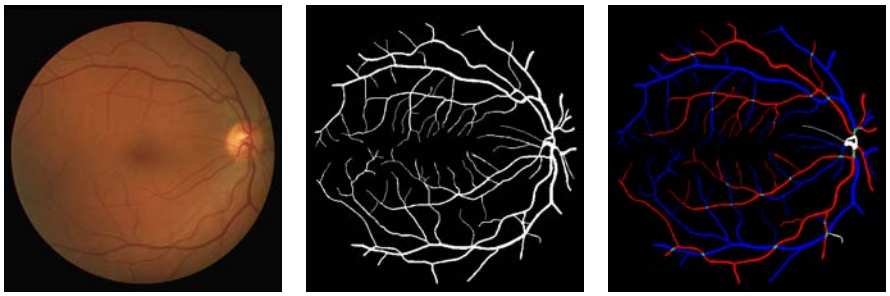

(a) (b) (c)

Figure 4.20: (a) A RITE fundus image. (b) The vessel reference standard. (c) The A/V reference standard.

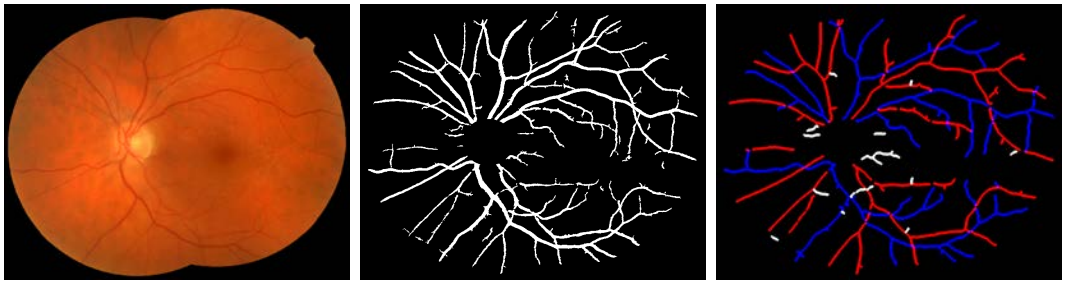

(a) (b) (c)

Figure 4.21: An example of result from the Mosaic dataset. (a) A fundus image. (b) The vessel segmentation. (c) The A/V reference (skeleton images are thickened for better visualization).

4.3.2 Evaluation Methods

The direct output of our algorithm is the labeled A/V vessel centerlines. For the RITE dataset, we evaluate the A/V vessels with respect to the A/V reference standard using the coverage rate and the accuracy. The coverage rate is the ratio of classified vessel pixels over all of the vessel pixels defined in the RITE reference standard, excluding pixels labeled as U or O. The accuracy is the ratio of correctly classified pixels over all classified pixels. Here two types of accuracies are used, referred to as the pixel-wise accuracy and the centerline-wise accuracy. The pixel-wise accuracy considers all vessel pixels, and the centerline-wise accuracy considers all vessel centerline pixels.

To calculate the pixel-wise accuracy and the coverage rate, a post-processing step is conducted to dilate the result of A/V centerlines into A/V vessel images, using the vessel reference standard as a mask. This results in a new image with each vessel pixel in the original vessel reference standard being labeled as A,V, or unclassified, based on the label of the corresponding centerline pixel in the algorithmic result. An unclassified vessel pixel occurs when no corresponding vessel is present in the input vessel segmentation or when the vessel segment has been removed during the VPCM construction.

Then this recovered pixel-based A/V vessel image is compared to the A/V reference standard. To calculate the centerline accuracy, the A/V reference standard is skeletonized first and then is compared with the result. During the measurement of the accuracy, all U is excluded, and all O is considered as correctly classified if classi-

Table 4.2: Evaluation Matrix

	A/V reference			
A/V algorithm result	A	V	Overlapping	Uncertain
A	TA	FA	TA_g	/
V	FV	TV	TV_g	/
Un-labeled	U			/

fied. The comparison is summarized in the matrix in Table 4.2 and the measurements are summarized in Eq. (4.18) and Eq. (4.19).

$$\text{CoverageRate} = \frac{TA + FA + TA_g + FA + TV + TV_g}{TA + FA + TA_g + FA + TV + TV_g + U} \tag{4.18}$$

$$\text{Accuracy} = \frac{TA + TA_g + TV + TV_g}{TA + FA + TA_g + FA + TV + TV_g} \tag{4.19}$$

4.3.3 Experiments on Effects of Global Functions

First of all, to investigate the effects of global functions on the optimization problem of separating VPCM into binary trees and classifying them into A/V trees, the developed methods with different forms of global functions are tested on RITE dataset. Since the approach is about the disambiguation of arterial and venous trees from a given vessel segmentation, both manual and automatic vessel segmentation are used as the input of the algorithm.

For the manual segmentation, since many very thin vessels are often of little

clinical interest, they are removed after we obtain partitioned vessel segments. In the experiment, the segments with width smaller than 1.5 pixels are removed, given the fact the the median vessel width is around 4-5 pixels and vessels narrower than 1.5 are very difficult to recognize even for humans (see Figure 4.22).

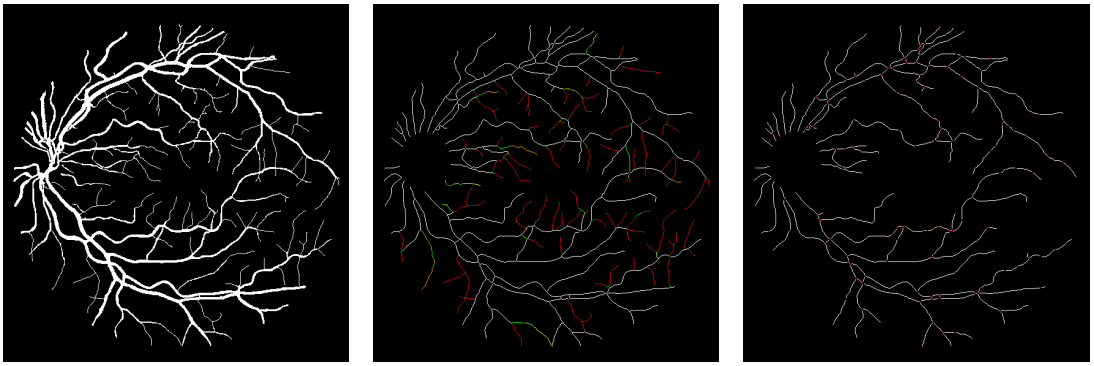

(a) (b) (c)

Figure 4.22: (a) The manual vessel segmentation. (b) The vessel segments with thin vessels in red. (c) The vessel segments after thin vessels removed.

For the automatic vessel segmentation, a vessel probability map is first generated using a method previously developed in our group [4]. And then the hysteresis threshold is used to threshold the probability map to obtain the vessel segmentation.

The notations of global cost functions are defined in Section 4.2.4.3, and the methods with different forms of global functions are summarized in Table 4.3. Since the global functions are only aimed to separate complex VPCMs that generate overlapping trees, only overlapping trees classification are evaluated in this experiment.

Table 4.3: Summary of methods using different forms of global functions.

	local cost	Tree Distance $D(G)$	Bifurcation Evaluator $B(G)$	Orientation Consistency $C(G)$
Method 1	*			
Method 2	*	*	*	*
Method 3	*	*		
Method 4	*		*	
Method 5	*			*
Method 6	*	*		*
Method 7	*	*	*	

In this case, the VPCMs for these methods are the same, thus the coverage rates are the same. Therefore accuracy is the only criteria used here. Since both centerline-wise and pixel-wise accuracies are very similar, the centerline-wise accuracy is used. The summary of the result for both the manual segmentation as the input and the automatic segmentation as the input are in Table 4.4 and Table 4.5. An example of results of different global functions is in Figure 4.23.

From Table 4.4 and Table 4.5, method 2 (the method using all three forms of the global functions) have the highest mean accuracy for both the manual and automatic vessel segmentations; And method 5 (the method using only the bifurcation evaluator term) has the lowest mean value for both segmentations. Two-tail pair-wise t-tests are conducted to compare method 2 with every other method. For the manual

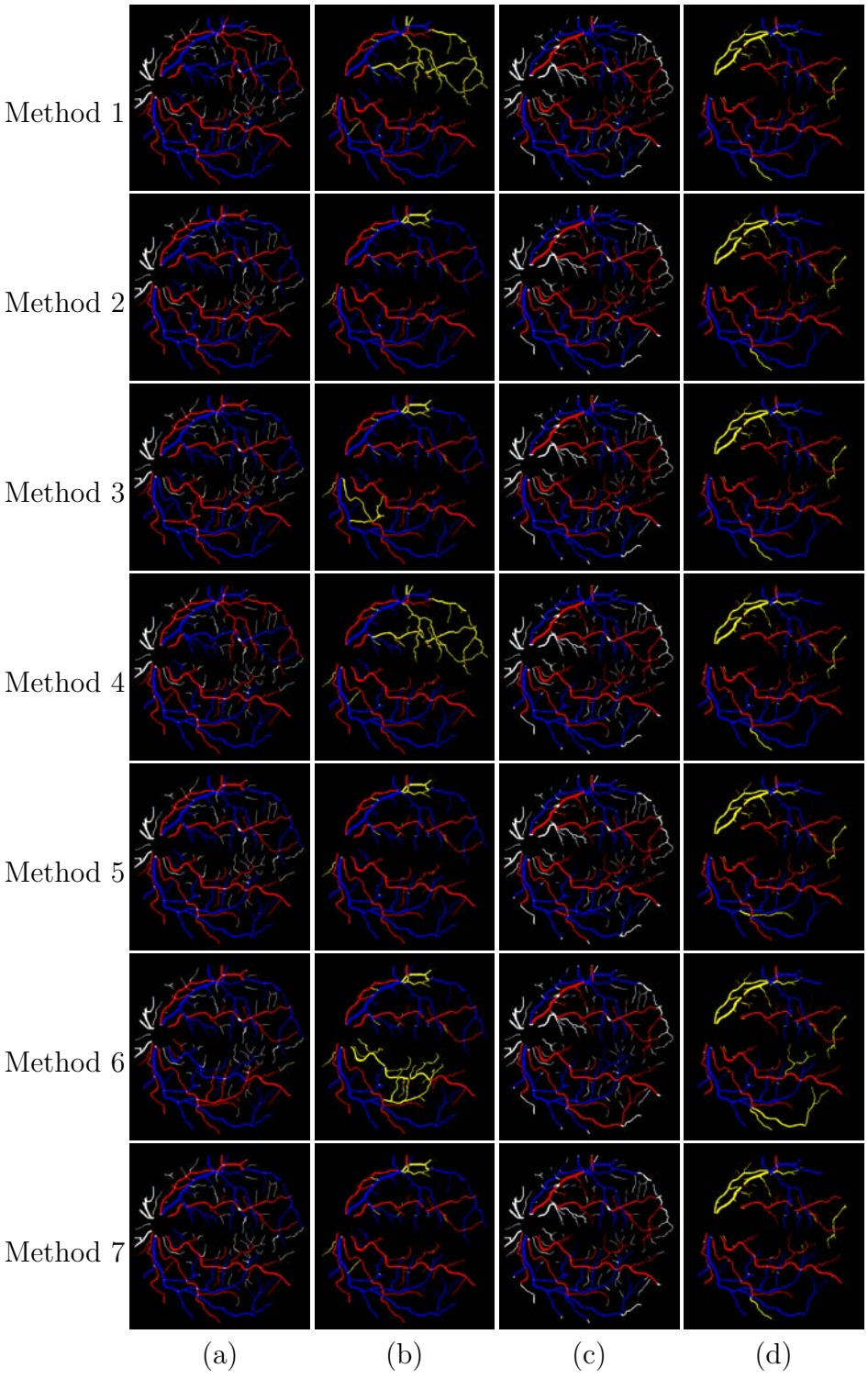

Figure 4.23: Examples of results for different global functions. (a) Result for manual vessel segmentation. (b) Result with error indicated in yellow for manual segmentation. (a) Result for automatic vessel segmentation. (b) Result with error indicated in yellow for automatic segmentation.

Table 4.4: Centerline-wise accuracies of methods using different forms of global functions when the manual vessel segmentation is the input.

	Mean & std. (%)	Min. (%)	Max. (%)	pairwise P-value
Method 1	86.56±11.01	63.27	99.92	0.061
Method 2	**88.76±9.85**	66.50	99.92	/
Method 3	85.31±12.81	52.17	99.23	**0.006**
Method 4	86.75±11.72	55.85	99.92	0.094
Method 5	85.60±13.01	49.50	99.92	**0.024**
Method 6	87.26±11.30	52.17	99.92	0.093
Method 7	86.51±12.54	51.94	99.23	**0.024**

Table 4.5: Centerline-wise accuracies of methods using different forms of global functions when the automatic vessel segmentation is the input.

	Mean & std. (%)	Min. (%)	Max. (%)	pairwise P-value
Method 1	84.91±10.91	59.81	99.44	0.089
Method 2	**87.34±9.46**	63.17	99.44	/
Method 3	85.29±11.47	58.97	99.44	0.076
Method 4	84.87±11.34	57.64	99.44	0.098
Method 5	83.89±11.06	59.62	99.44	**0.012**
Method 6	86.39±9.99	62.65	99.44	0.095
Method 7	85.35±11.48	58.97	99.44	0.059

vessel segmentation, method 2 is significantly better than method 3, method 5 and method 7. For the automatic vessel segmentation, method 2 is significantly better than method 5. Although method 2 does not have significantly better results than method 1, method 4 nor method 6, it has slightly better result than any of them. Due to this reason, the global functions in method 2 are selected as the final form of the global function and are used in all of the later experiments.

4.3.4 Experiments on the Influence of Vessel Segmentation

The second experiment is conducted to investigate the influence of different vessel segmentations on the performance of the algorithm to separate complex VPCMs and classify generated overlapping trees into A/V trees. The experiment is conducted on RITE dataset. To simulate different vessel segmentations, hysteresis thresholds with different parameters are applied to the vessel probability map used in the first experiment to yields different vessel segmentations. In this experiment, the two thresholding parameters of the hysteresis threshold (the lower bound I_l and the higher bound I_h) are controlled by Otsu's Thresholding value I_o (see Eq. 4.20). Here 8 pairs of T_l and T_h are setup to simulate 8 different vessel segmentations. The 8 pairs of values are (0.5, 1.1), (0.6, 1.1), (0.7, 1.1), (0.8, 1.1), (0.9, 1.2), (1.0, 1.3), (1.1, 1.4) and (1.2, 1.5), and their vessel segmentation are referred as input 1 to input 8. Among them the first generates the most segmentation, and the the last generates the least segmentation. An example of vessel segmentations of an fundus image with noise is in Figure 4.24.

$$I_l = I_o * T_l$$
$$I_h = I_o * T_h \tag{4.20}$$

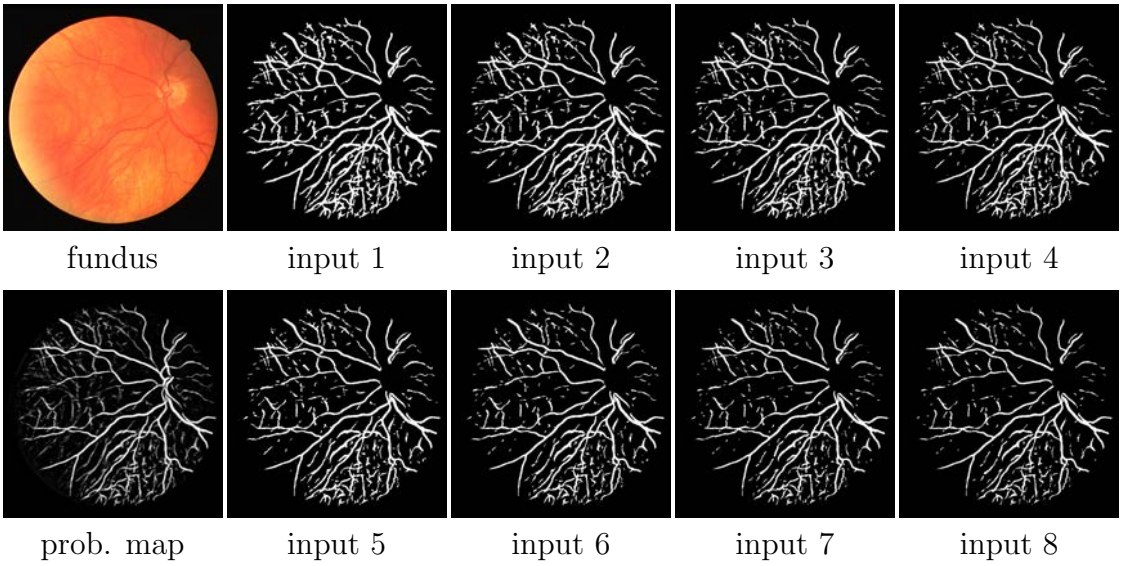

Figure 4.24: An example of a fundus image with a large amount of noise and different vessel segmentations.

The performance of the algorithm on the 8 vessel segmentations of RITE dataset is summarized in Table 4.6. The coverage rates and accuracies are plotted in Figure 4.25. It shows that the coverage rate decreases as the vessel segmentation includes less vessel pixels. The accuracies fluctuate over different vessel segmentations, but in general they increase as the vessel segmentation includes less vessel pixels. Besides, it is noteworthy that the algorithm fails on one or two images for the first 4 inputs. This implies that when the thresholds are low so the vessels are over-

Table 4.6: The results of A/V tree construction trees using overlapping trees on 8 different automatic vessel segmentation.

	Coverage Rate(%)	Pixel-wise Accuracy(%)	Centerline-wise Accuracy(%)	No. of failed images
Input 1	79.68±4.42	85.54±10.78	85.81±10.65	2
Input 2	78.90±5.04	86.01±8.92	86.15±9.23	2
Input 3	77.40±6.17	84.70±10.92	84.72±11.29	2
Input 4	76.44±6.58	86.97±7.84	87.36±8.15	1
Input 5	76.14±6.91	85.14±9.61	85.26±9.96	0
Input 6	75.58±9.27	85.32±10.62	85.48±11.22	0
Input 7	74.04±7.92	86.99±9.59	87.72±10.13	0
Input 8	71.07±11.37	86.59±10.31	87.46±10.40	0

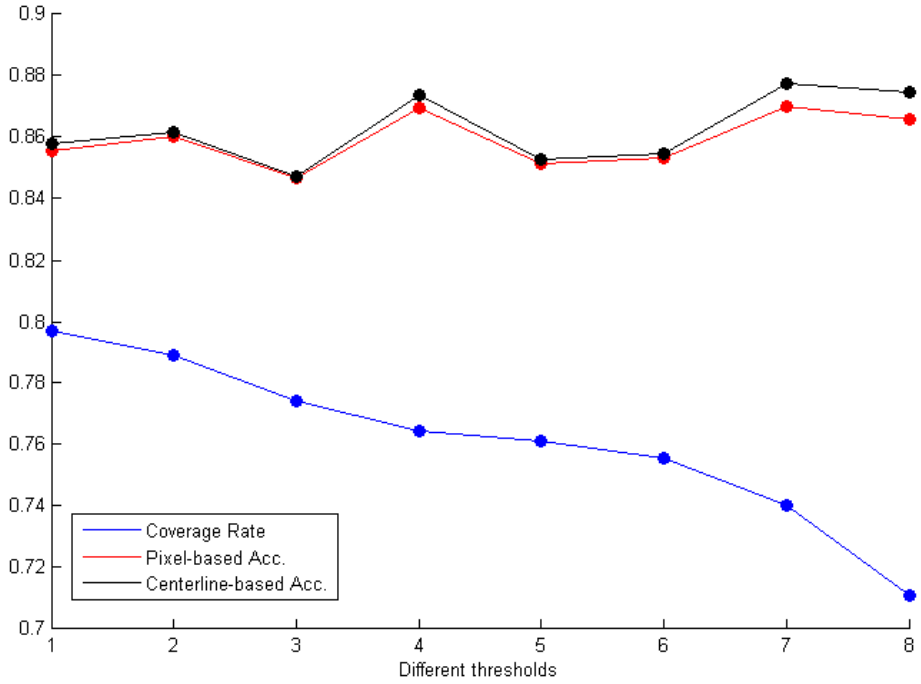

Figure 4.25: The coverage rates and accuracies for different vessel segmentations.

segmented and too many false-positives are included, the algorithm might fail. The failures happen because during the construction of the VPCM, false-positives disturb the vessel neighborhood searching thus a VPCM with too many cycles are generated thus unable to be separated. An example of the failed images with different outputs are shown in Figure 4.26. The fundus image and the vessel segmentations are shown in Figure 4.24. For this fundus image, the first three input are badly over-segmented thus the algorithm fails to generate binary overlapping trees. Although the remaining five inputs still contain a fair amount of false positives and noise, the developed algorithm manages to construct the VPCM and separate it into binary overlapping trees. The result of this experiment implies that in order to obtain a satisfying result,

Table 4.7: A/V classification results for independent trees on RITE.

	Manual		Automatic	
	Pixel-wise Accuracy(%)	Centerline Accuracy(%)	Pixel-wise Accuracy(%)	Centerline Accuracy(%)
Pixel-classification	88.61 ± 10.11	74.45 ± 20.05	85.91 ± 8.81	75.49 ± 20.67
Pixel-classification with geometric constraint	80.15 ± 17.50	78.05 ± 20.30	72.48 ± 22.13	74.01 ± 22.38

the vessel segmentation has to be of a certain quality. The results from input 5 to input 8 indicates that for different vessel segmentations with a satisfying quality, the algorithm has similar performance. However there is a trade off between the coverage rate and accuracies. This is understandable since the higher coverage rate indicates more small vessels are classified, thus the accuracies would be impaired.

4.3.5 Experiments on Independent Tree Classification

The two methods for independent tree classification is evaluated on the RITE dataset and the result is shown in Table 4.7. From the table we see that the pure pixel-classification algorithm works better than the pixel-classification with geometric constraint, for both the manual vessel and automatic vessel segmentations as the input. For this reason, only the pixel-classification algorithm is used as the method for independent tree classification in any later experiments.

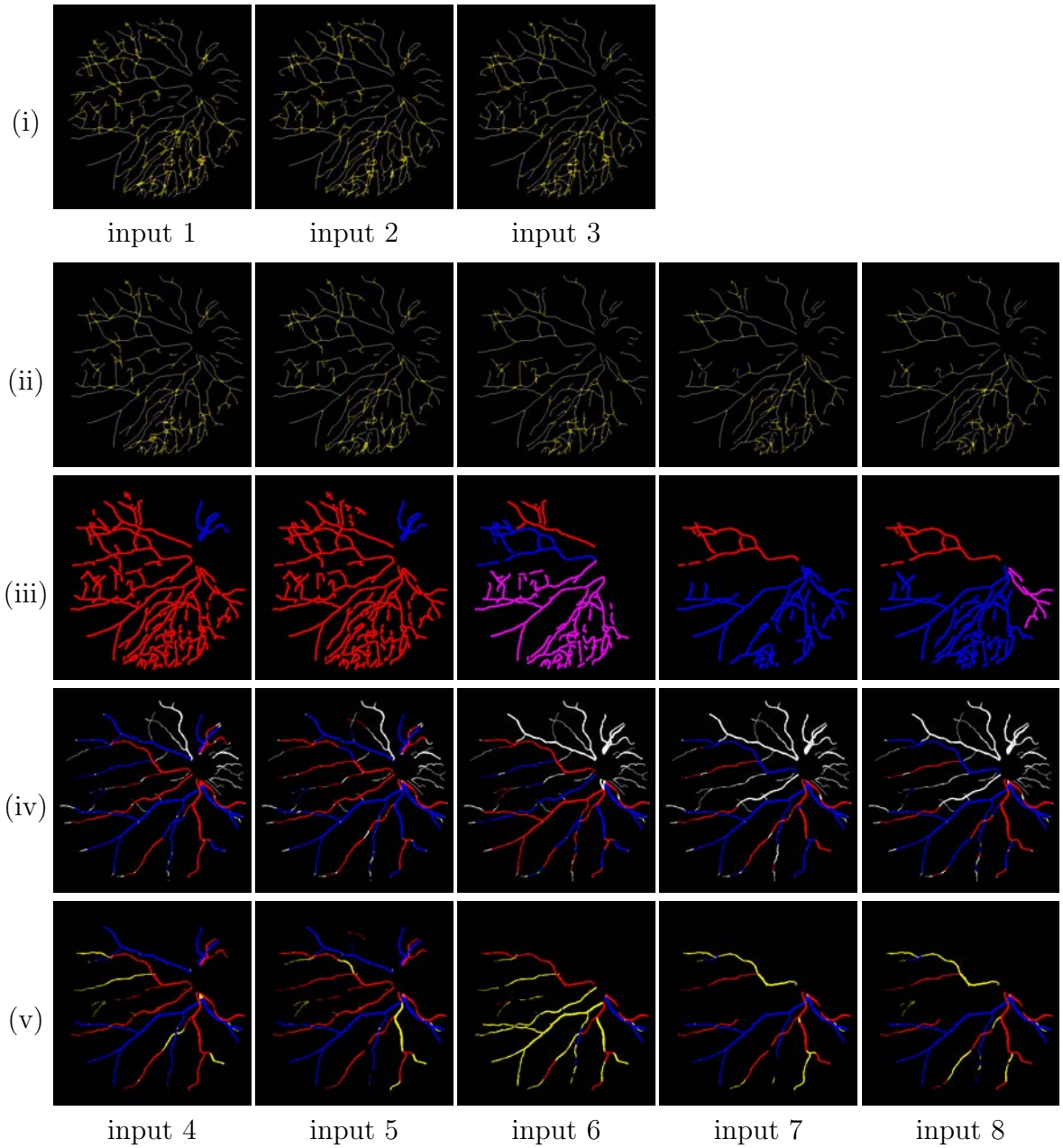

Figure 4.26: An example of results with failure for different vessel segmentations as the input. Row (i): The VPCMs for the first three vessel segmentations that fails to be separated into overlapping trees. Row (ii): The VPCMs for the rest five vessel segmentations that yields overlapping tree results. Row (iii): The complex VPCMs to be separated for the rest five vessel segmentations. Row (iv): The A/V classification of overlapping trees overlapped with vessel reference standard. Row (v): The A/V classification of overlapping trees with errors indicated in yellow.

4.3.6 Overall Performance

The overall results performed on RITE dataset for the manual vessel segmentation input and the automatic vessel segmentation input are presented in Table 4.8 and Table 4.9 respectively, with the classification for the overlapping trees, the independent trees and all trees. An example of results for both inputs is shown in Figure 4.27.

From the two tables, we see that the results for manual vessel segmentation are better than those for automatic vessel segmentation, which have both higher coverage rate and accuracies. This is reasonable since the manual vessel segmentation has higher quality than the automatic one. However, the difference of accuracies is not large, showing that the proposed method can process vessel segmentations with different qualities. Also the classification accuracies for overlapping trees are better than those for independent trees, especially the centerline accuracy.

For the Mosaic dataset, only the centerline accuracy is measured. The result is shown in Table 4.10, along with the result of previous version [146], which only worked on overlapping trees, but ignored independent trees. The higher accuracy of our current approach indicates a cost function combining vessel width, intensity, direction and dominant orientation is advantageous, since the previous one only used vessel directions. Example results are shown in Figure 4.28.

Table 4.8: A/V classification results for manual vessel inputs on RITE.

	Coverage Rate (%)	Pixel-wise Accuracy (%)	Centerline-wise Accuracy (%)
Overlap. Trees	80.38 ± 9.15	89.38 ± 9.15	88.72 ± 9.62
Indep. Trees	7.66 ± 7.50	88.61 ± 10.11	74.45 ± 20.05
All Trees	88.04 ± 4.95	88.15 ± 8.68	87.13 ± 9.14

Table 4.9: A/V classification results for automatic vessel inputs on RITE.

	Coverage Rate (%)	Pixel-wise Accuracy (%)	Centerline-wise Accuracy (%)
Overlap. Trees	74.48 ± 12.85	86.85 ± 8.21	86.76 ± 7.77
Indep. Trees	9.07 ± 9.07	85.91 ± 8.81	75.49 ± 20.67
All Trees	83.55 ± 5.35	86.11 ± 7.64	85.91 ± 7.39

Table 4.10: A/V classification results for automatic vessel inputs on Mosaic.

	Overlapping Trees	Indep. Trees	All trees	Previous method [146]
Centerline Accuracy(%)	87.25 ± 8.32	63.38 ± 33.98	85.32 ± 8.23	84.00 ± 9.00

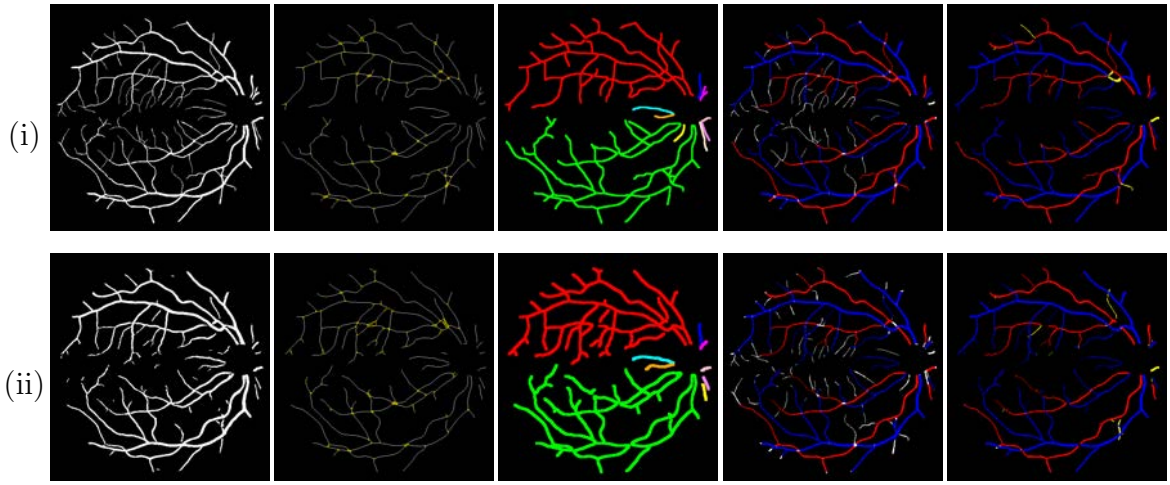

Figure 4.27: Examples of results from the fundus image in Figure 4.20(a). Row (i): results from the manual input. Row (ii): results from the automatic input. (a) Vessel segmentation. (b) VPCM with neighborhood indicated in yellow boundary. (c) Independent VPCMs in different colors (centerlines thickened for better visualization) (d) A/V results overlapped with vessel segmentation ground truth (red for A, blue for V). (e) A/V results with errors in yellow.

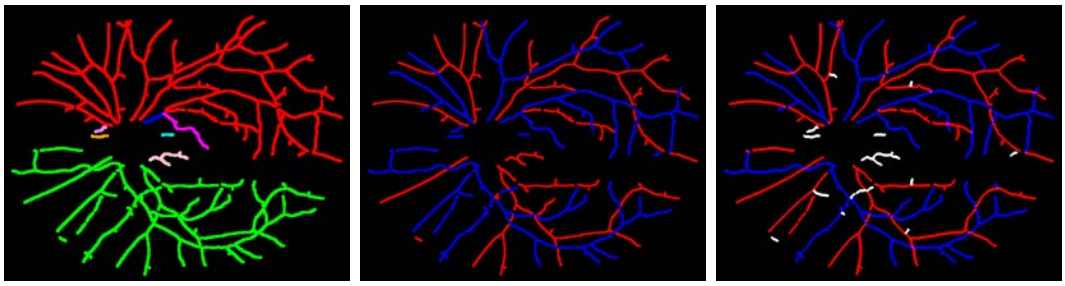

(a) (b) (c)

Figure 4.28: The result from the example from Mosaic dataset shown in figure 4.21. (a) The VPCMs. (b) The A/V result. (c) The A/V reference (skeleton images are thickened for better visualization).

4.4 Discussion

A novel method to construct the arterial and venous vasculature from retinal images is proposed in this chapter. Using the topological property of the retinal vessels, the developed algorithm is able to use both local and global information to recognize the landmarks of the vessel network thus to construct the anatomical trees. The general strategy is to build an over-connected vessel network first, a VPCM, and then separate it into multiple trees with binary labels. During the construction of the VPCM, neighborhoods are properly constructed to represent potential landmarks. Then separating the VPCM is modeled as an optimization problem and solved using a special graph-based meta-heuristic algorithm. The major merit of the method is that it avoids being trapped at local optima due to local errors (image noise, vessel segmentation and pre-processing errors), because it utilizes a variety of features both

locally and globally. The proposed method also can recognize some small vessels which are difficult to classify using only local knowledge.

To demonstrate its performance, a publicly available dataset RITE is built which is based on the well-known dataset DRIVE. RITE and another previously built dataset MOSAIC are used to evaluate the performance of this developed algorithm. The result from RITE indicates that this method performs well on both manual and automatic vessel segmentation inputs. The reported results are also comparable with recent work by Dashtbozorg *et al.* [153], who tested on half of DRIVE (DRIVE test set of 20 images). In particular, using the images from the DRIVE test set with the automatic vessel segmentation as the input (half of the images reported in the experiments), the developed method obtains mean and std. of the pixel-wise accuracy as $87.09\% \pm 9.18$ for the overlapping trees, and $85.68\% \pm 8.34$ for all trees. Using a different automated vessel segmentation as input and an A/V reference standard defined by different experts, Dashtbozorg's algorithm obtained a pixel-wise accuracy of 87.4%. However, Dashtbozorg *et al.* only classified the main vessels (vessels with a width larger than 3 pixels). While they did not provide a reported coverage rate, it is reasonable to assume that since the developed method included classification of smaller vessels, our coverage rate is likely higher. In addition, the accuracy is of course also dependent on the input vessel segmentation as evident by the fact that the accuracy increased when using a manual vessel segmentation as input. For DRIVE test set with manual vessel input, the developed method achieves mean and std. of pixel-wise accuracy as $90.5\% \pm 8.98$ for the overlapping trees and $88.76\% \pm 8.83$ for

all trees. Note that not all methods would necessarily perform better when using a manual vessel segmentation as input, given the additional vessels to classify, as indicated in our pixel-classification-only results in the next paragraph.

The performance of the developed method is also comparable to a method developed by Joshi *et al.* [124], which was tested on a randomly generated subset of the MOSAIC data. Tested on 13 randomly selected images, Joshi's method yields an average pixel-wise accuracy of 88.28%, comparing with a ground truth generated by their group. The developed algorithm yields an average centerline-wise accuracy of 87.25%, which is very close to that of Joshi's method.

It is also interesting to note that the results from both datasets indicate that the core part of the developed method, which involves the separation and classification of overlapping trees, performs better than the pixel-based classification of independent trees. To further explore the potential advantage of including the tree separation component in final classification results, pure pixel-based classification method is compared (i.e., determining the label of each vessel segment based only on the majority-vote for all classified centerline pixels within the segment) on all trees for images from RITE. Generating the same coverage rate, the pixel-classification-only approach obtained a mean pixel-wise accuracy and centerline accuracy of $81.90\% \pm 6.17$ and $79.37\% \pm 6.60$ for automatic vessel segmentation as input (which is smaller than the $86.11\% \pm 7.64$ and $85.91\% \pm 7.64$ accuracies obtained by the full approach); for manual vessel segmentation as input, it obtained a mean pixel-wise accuracy and centerline accuracy of $79.27\% \pm 6.09$ and $74.91\% \pm 6.39$ (which, again, is smaller than the

$88.15\% \pm 8.68$ and $87.13\% \pm 9.14$ accuracies obtained by the full approach). The fact that using an automatic vessel segmentation as input yields higher accuracy for the pixel-classification-only approach when compared to using a manual vessel segmentation as input is likely because automatic vessel segmentation has fewer thin vessels than the manual vessel segmentation, which are difficult to classify merely using local information.

The algorithm is implemented in C++ and runs on a common Linux computer (AMD Opteron Processor 8439 SE). The median of total running time is 175 seconds, with the maximum case of 573 seconds. For RITE dataset, the median of the running time for solving the overlapping tree is 26.9 seconds, with the maximum case of 385 seconds. Since images in RITE are mostly fovea-centered, most of them contain two major complex VPCMs, with several exceptions containing one, three or four complex VPCMs. A graph transferred by a major complex VPCM normally has around 80 nodes and 100 edges, and 10 cycles. The largest graph contains 248 nodes and 284 edges, with 37 cycles, which corresponds to the image with the maximum running time. It happens for image 13_test in RITE with the manual vessel segmentation as input (Figure 4.29). This is the only graph that the heuristic algorithm cannot find a feasible solution and the solution generated contains cycles.

4.5 Conclusion

In this chapter, a novel framework is presented to automatically construct the arterial and venous vascular trees in retinal images given a vessel segmentation.

(a) (b) (c) (d) (e)

Figure 4.29: The image with the largest graph. (a) The fundus image. (b) The vessel ground truth. (c) Independent VPCMs in different colors. (d) A/V result overlapping with the vessel segmentation. (e) A/V result with errors in yellow.

The presented framework repairs connectivity between vessels by building a strongly connected network and the vessel network is separated into overlapping binary trees by using a graph-based algorithm. Then a pixel-based classification method is used to distinguish these overlapping binary trees, as well as other independent trees into A/V trees. The presented approach is tested on a public dataset and a private dataset. Experiments show that the presented method constructs A/V trees with high accuracies and high coverage rate, for both manual vessel segmentation and different automatic vessel segmentations. This demonstrates its robustness and high accuracy. Thus the promising results indicate its reliable performance and potential applicability to large-scale datasets for further analysis of the retinal vasculature.

CHAPTER 5
THE ANALYSIS OF THE RETINAL VASCULATURE IN A CLINICAL SETTING

5.1 Introduction

The changes of the retinal vasculature are used to monitor and examine the health status of human beings. One of the widely used features is the vessel width, which can be measured and represented as the central retinal arterial equivalent (CRAE), central retinal venous equivalent (CRVE) and artery-vein ratio (AVR). Previous studies have found that changes in CRAE/CRVE and AVR are associated with many diseases, disorders and abnormalities (see Section 2.1.3 for details).

Despite their wide application, the current methods to calculate CRAE/CRVE and AVR have the disadvantages in that they are subjective and sensitive to inter-observer variability. CRAE and CRVE are calculated by estimating central artery and vein diameters, which cannot be imaged with current methods, from their daughter branches recursively, based on the relationship between the diameter of parent and daughter vessels, known as Murray's law [136]. The first problem is that the choices of vessels to include is subjective and sensitive to inter-observer variability. The decision of which vessels to include and not include in the calculation is arbitrary. Another issue is that overlapping of arterioles and venules close to the optic disc makes it hard to decide the vessel type for both human experts and algorithms, and thus introduces uncertainty.

In this chapter, based on the algorithm developed in chapter 4, modified meth-

ods are introduced to calculate CRAE/CRVE by using the topological properties provided by the constructed A/V trees. By taking advantage of the topological information, the proposed tree-based CRAE/CRVE is expected to be more objective and unbiased. To evaluate it, new methods are applied on a cohort study of human immunodeficiency virus-infected (HIV-infected) patients under highly active anti-retroviral therapy (HAART) and are compared with the conventional CRAE/CRVE method which is based on determining arterial and venous vessel widths in a ring around the optic disc. Statistical analysis is conducted to determine the merits of the proposed method, as well as changes related to HIV-infection and HAART treatment.

The rest of this chapter is organized as follows. First, the data is described in Section 5.2. Then the new methods to calculate CRAE/CRVE are presented followed by a brief review of the traditional method in Section 5.3. Then the experiment to calculate CRAE/CRVE using different methods and the comparison among them is presented in Section 5.4. The results are presented in Section 5.5 and the discussion of merits of the methods and new findings are presented in Section 5.6. A brief conclusion is in Section 5.7.

5.2 Data

In this cohort study, 76 HIV-1-infected participants were recruited at the HIV outpatient clinic of the Academic Medical Center in Amsterdam, The Netherlands, and 58 HIV-uninfected case-matched controls were selected from the ongoing Amsterdam Cohort Studies on HIV/AIDS and among persons attending the sexual health

clinic of the Amsterdam Public Health Service (details have been described in a previous publication) [154]. Participants are all males with ages larger than 45. For the HIV-infected group, inclusion criteria is sustained suppression of HIV viremia on antiretroviral treatment (plasma HIV-RNA $<$ 40 copies/mL) for a period of time $\geq$ 12 months. Images for participants were taken at two visits. The first is at the initial treatment of the HIV-infection, and the second at the follow-up around two years after. The time of visits for the control group are taken around a similar time to match with the patient group.

At each visit, fundus photographs are obtained for both eyes of each participant with a Topcon TRC- 50DX/IA camera. Several missing visits occurred for some individuals from both groups. The total number of images from the patient group is 276 and from the control group is 212. Each image has a size of 3000 x 2672, with a 50-degree field of view, and is fovea-centered. Before any image processing, these photographs are rescaled first to a size of 750 x 668, in order to obtain a good performance for the vessel segmentation and the A/V tree construction. Institutional Review Board approval was obtained and informed consent was given.

In general, previous studies show some changes in CRAE and CRVE in HIV-infected patients in HAART treatment. The work in [59] shows that male patients have significantly narrower venlues than controls. It also shows that there is a significant trend of both narrower arteriolar and venular diameters with increasing age in the HIV-infected group. It shows that a longer duration of HAART is associated with narrowing of arterioles. Similar findings are claimed by another study [58] indi-

cating that smaller CRAE and larger CRVE are associated with a history of HAART. However this finding is not backed by the study [60], which states that there is no association between the length of HAART and the decrease in CRAE from their data.

5.3 Methods

5.3.1 Conventional CRAE/CRVE and AVR

The most popular conventional method, developed by Kundtson [138], is to use the widths of vessels around a region close to the OD to estimate the widths of retinal artery/vein. Specifically, denoting the diameter of the OD as D, then a concentric ring centered at the OD, with an inner radius of D, and a outer radius of $1.5D$ is defined as the region for vessels to be measured (zone A in the example of Figure 5.1). The width of each vessel that falls within this region is measured and the average width for each vessel is calculated. Then the six largest widths of arterioles/venules are converted into a single width, which is CRAE/CRVE. The conversion is conducted in an iterative manner. In each iteration, widths are sorted and every two widths are paired together such that the largest is paired with the smallest, and the second largest is paired with the second smallest and so on. Every pair of widths is converted into one width according to Eq. 5.1. Here w_1 and w_2 are a pair of widths, and W_c is the new width which replaces the pair in the next iteration. Arterioles and venules use different parameters because they are known to have different relationships at the bifurcation. Each iteration decreases the number of widths by half. If the number of widths is odd, the medium width is simply saved

in next iteration. The conversion continues until there is only one width, which is CRAE/CRVE. Then AVR is calculated as the ratio of CRAE and CRVE.

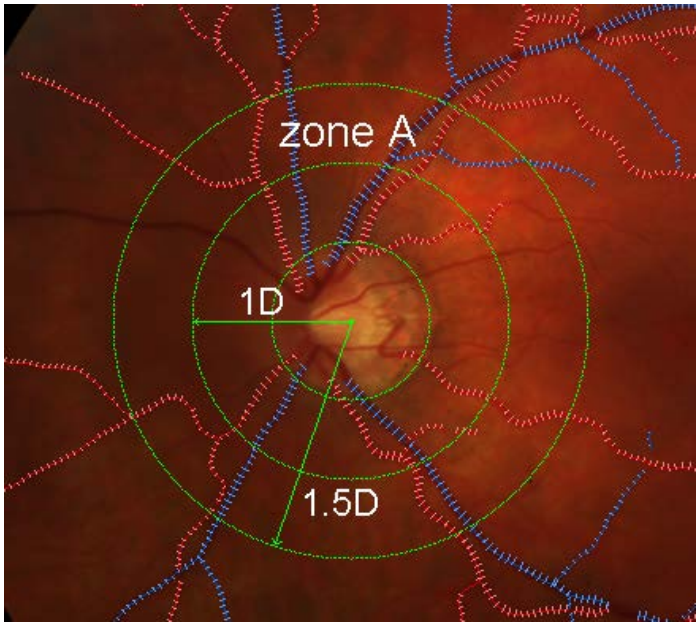

Figure 5.1: An illustration of the region (zone A) used by the conventional method to measure widths of vessels for the calculation of CRAE/CRVE.

$$\begin{aligned} \text{Arterioles: } W_c &= 0.88 \times (w_1^2 + w_2^2)^{1/2} \\ \text{Venules: } W_c &= 0.95 \times (w_1^2 + w_2^2)^{1/2} \end{aligned} \tag{5.1}$$

5.3.2 Topologies of Constructed A/V Trees

The A/V trees constructed by the developed algorithm in Chapter 4 provide topological information that can be used to calculate the vessel width. First of all, the vessel network provides a pair relationship between intertwined A/V trees. A

typical fundus would contain one or two major VPCMs (the ones in green and red in Figure 5.2(a)). A/V trees that are generated from the same major VPCM share some topological similarities and thus they provide good comparing reference. This comparison is typically useful when AVR is calculated that involves the relative width between the arteries and veins. In addition to this inter-network topology, each tree itself contains some topological information. In normal cases each tree starts from a root vessel that is closest to the OD (see Figure 5.3). Then the root vessel bifurcates into its children vessels and they further bifurcate into next layer and this process continues until it reaches the end of the tree. The vessels at the end of trees are defined as leaf vessels.

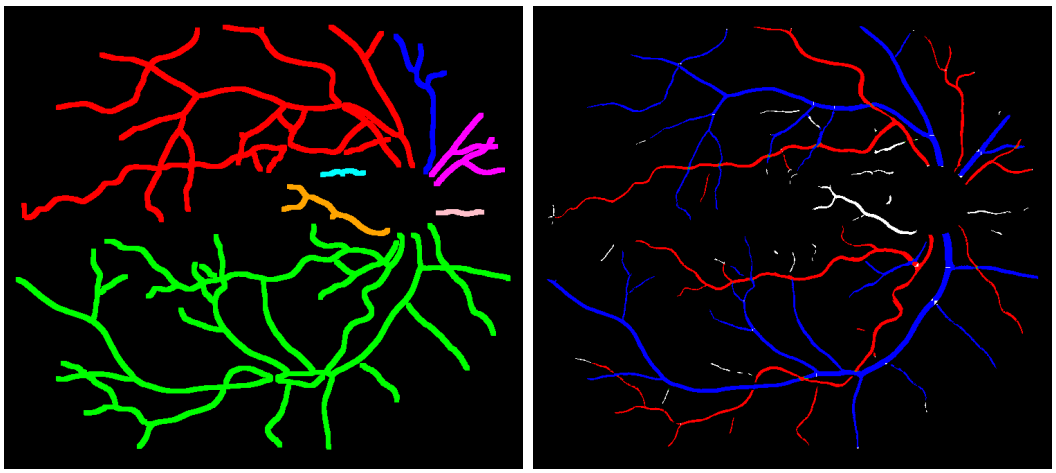

(a) (b)

Figure 5.2: An example of the topological information provided by the constructed A/V trees (a) VPCMs in different colors during the construction of A/V trees. (b) The result of A/V trees (arteries in red and veins in blue).

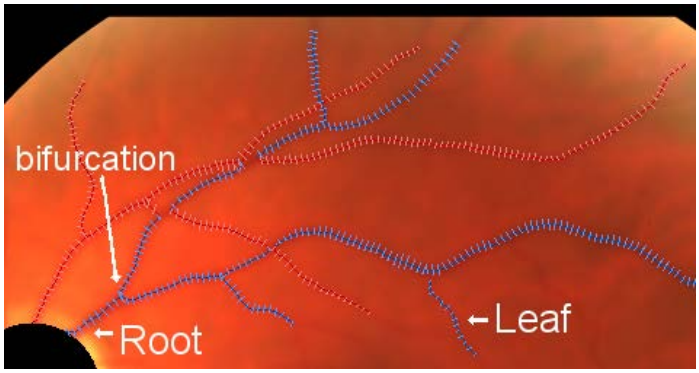

Figure 5.3: The topology of a single tree.

5.3.3 Root-based CRAE/CRVE

In this method, a root width is calculated first to represent the width for each tree. The root width is the average width of the root vessel within a circular zone denoted as A, which is centered at the OD, whose radius is 1.5 of the diameter of the OD. If any part of the root vessel falls outside of the zone, the widths of that part is not considered in the averaged width. An example is shown in Figure 5.4. If the length of a root vessel is shorter than 20 pixels, the children vessels of the root vessel are considered. Particularly, the averaged widths of children vessels that are within zone A are calculated first. And then they are merged into one width using Eq. 5.1. The merged width W_c then is averaged with the width of the root vessel to represent the root width of the tree.

After the root width of each tree is obtained, we use them to calculate CRAE and CRVE in a way similar to the conventional method. The only modification is

that instead using the six largest vessel widths, we use all root widths of arterial and venous trees.

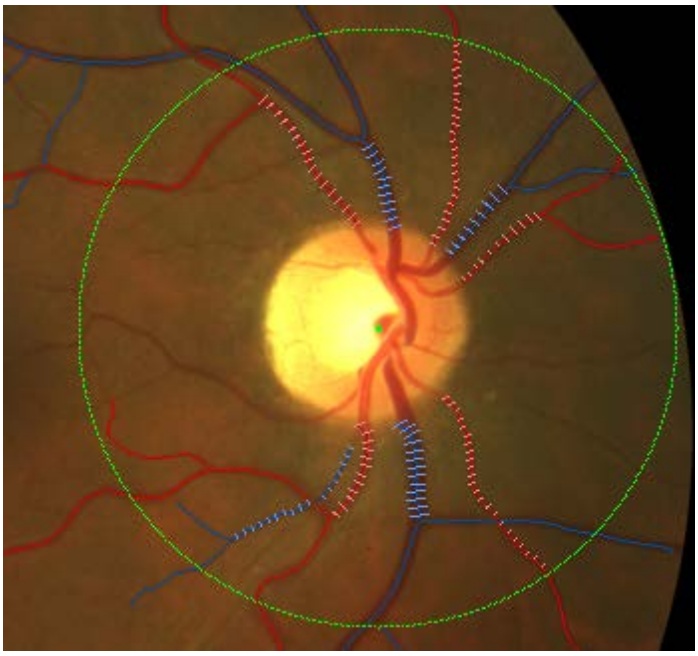

Figure 5.4: An example of measurement of vessel width using the root-based CRAE/CRVE method.

5.3.4 Tree-based CRAE/CRVE

In the second method, instead of using the root widths, we use the widths of the whole A/V trees . In this method, a tree width W_t is generated for each tree first and then W_t is used to obtain the CRAE/CRVE. To generate W_t, widths along all vessel centerlines are first measured and they are averaged for each vessel. Then the average width of each vessel is merged in an iterative manner. The iteration takes

place at the leaf vessels, which are the children vessels of the last layer of bifurcations. Specifically, widths of leaf vessels of the same bifurcation are merged using Eq. 5.1. Then the merged width W_c is averaged of the width of the parent vessel W_p, to obtain the new width of the parent vessel W_p' (See Eq. 5.2, where l_p is the length of the parent vessel, and l_c is the average length of the two children vessels).

$$W_p' = (W_c * l_c + W_p * l_p)/(l_c + l_p) \tag{5.2}$$

In the next iteration, parent vessels become children vessels for the bifurcations of upper layer, and their widths are merged in the same manner to update the width of their parent vessel. The width of vessel is iteratively updated from the lowest layer until the procedures reaches the root vessel. When it comes to the bifurcation whose parent vessel is the root vessel, W_t is obtained by merging the widths of two children vessels using Eq. 5.1. At this point, we do not use Eq. 5.2 to average it with the width of the root tree is because the arterioles and venules are often overlapped near the OD and it is difficult to separate them either manually or automatically.

After W_t is obtained for each tree, we use it to calculate CRAE/CRVE. Due to the fact that our A/V tree construction algorithm has higher accuracy among the major vessel networks compared to single independent vessel trees, only trees from the two largest vessel networks are considered, or in some cases one major vessel network, if the two of them are intertwined.

5.4 Experiments

To examine the possibility of automatic calculation of CRAE/CRVE, two versions of A/V tree constructed are acquired. The first one is referred as the automatic A/V trees which are constructed using the algorithm introduced in Chapter 4. The second one is referred as the manual A/V trees, which is generated by manually correcting the errors in the automatic A/V trees. These two versions of A/V trees are used to calculate CRAE/CRVE and AVR. The two proposed methods are compared with the conventional method. The root-based method and the tree-based method are calculated based on the automatic A/V trees, denoted as Method 1 and Method 2 respectively. And the conventional method is calculated based on the automatic A/V trees and the manual A/V trees, denoted as Method 3 and Method 4 respectively. We are interested in if any of Method 1, Method 2 and Method 3 is as good as Method 4 or better.

5.4.1 Human Intervention of A/V Tree Construction

A Matlab GUI is developed to facilitate the manual inspection and correction of A/V trees. The average time to correct a result with errors is around 3 minutes. Among 488 total images, 246 are manually corrected, which yields the correction rate of 49.6%. An example of A/V trees before the correction (the automatic A/V trees) and after the correction (the manual A/V trees) is shown in figure 5.5.

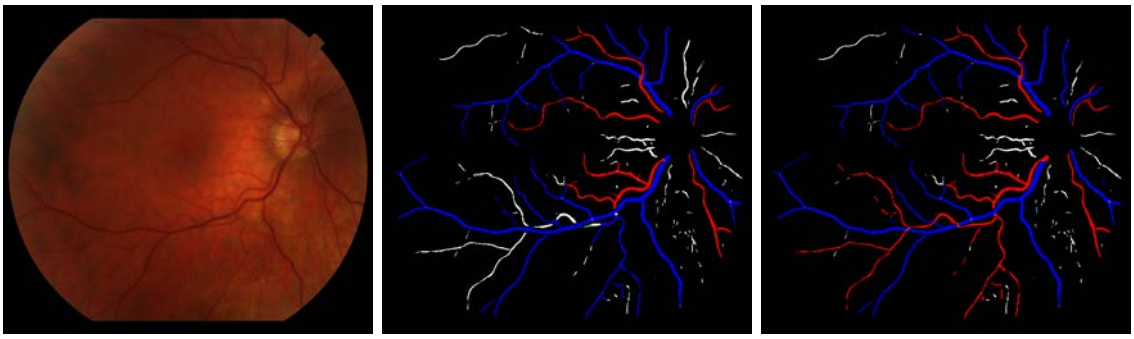

(a) (b) (c)

Figure 5.5: An example of the automatic and manual A/V trees. (a) The fundus image. (b) The automatic A/V trees (arteries in red and veins in blue). (b) The manual A/V trees.

5.4.2 Statistical Analysis

To investigate the effects of different methods on indicating the changes of vessel widths between two visits among patients and controls, and on indicating the effect of age, generalized linear mixed-effect models (GLMMs) are used to model the effects of these variables on CRAE, CRVE and AVR. For each of them, three type of values are analyzed separately: the value at Visit 1, the value at Visit 2 and the difference between Visit 1 and Visit 2 (Visit 2 - Visit 1). Thus 9 types of values are analyzed in this experiment. These 9 values are analyzed using the same GLMM model. Besides variables of method type, subject type and age, the model also considers the interaction between the method type and the subject type, and the interaction between the method type and age. To probe the performance of new

methods compared to the conventional method, Method 4 is the reference method and the rest three methods are compared with it. For the variable of subject type, control is the reference. All statistical analyses is performed using Statistical Analysis Software.

5.5 Results

The descriptive measure of the data without any adjustment is summarized in Table 5.1. The unit of CRAE/CRVE is pixel and AVR is without unit. Pair-wise t-tests are conducted between the controls and the patients for each visit and each method. Without any adjustment, from this table there is no difference between controls and patients in CRAE, CRVE and AVR. Specifically, for CRAE, patients have similar CRAE compared to controls at Visit 1 (V1). At Visit 2 (V2), patients have smaller CRAE, but not significantly. For CRVE, patients have higher values compared to controls at V1. Although it is not significant, the difference is close to being significant (P-value is 0.094 for Method 1, 0.075 for Method 3, 0.063 for method 4, and 0.257 for Method 2). At V2, patients and controls have similar CRVE for method 1, method 3 and method 4. However method 2 shows patients have slightly higher value than controls with P-value being 0.093. For AVR, at V1, patients have smaller values than controls, but not significantly. At V2, patients have larger values than controls from method 1 and method 3, with P-values close to 0.05. In general, without adjustment, the basic statistical analysis reveals that there is no significant difference in CRAE/CRVE and AVR between the patient and the control groups.

Table 5.1: Statistical summary of four methods on patient and control groups of both visits for CRAE, CRVE and AVR.

	Method	Visit	Control (mean±std.)	Patient (mean±std.)	t-test P-value
CRAE	Method 1	1	7.062±1.127	7.124±0.913	0.745
		2	6.954±0.803	6.773±0.904	0.290
	Method 2	1	6.956±0.960	7.087±0.955	0.458
		2	6.444±0.868	6.648±0.826	0.187
	Method 3	1	7.105±1.075	7.165±0.889	0.745
		2	7.023±0.782	6.842±0.891	0.228
	Method 4	1	6.975±1.038	7.243±1.113	0.276
		2	6.972±0.731	6.953±0.940	0.899
CRVE	Method 1	1	9.671±1.500	10.098±1.173	0.094
		2	9.608±1.185	9.817±1.123	0.321
	Method 2	1	9.736±1.529	10.042±1.353	0.257
		2	9.282±1.090	9.636±1.249	0.093
	Method 3	1	9.658±1.480	10.121±1.286	0.075
		2	9.695±1.284	9.784±1.023	0.674
	Method 4	1	9.888±1.259	10.325±1.270	0.063
		2	10.088±1.220	10.004±0.985	0.702
AVR	Method 1	1	0.746±0.137	0.715±0.1008	0.168
		2	0.734±0.087	0.703±0.103	0.075
	Method 2	1	0.724±0.082	0.713±0.080	0.439
		2	0.701±0.095	0.696±0.069	0.749
	Method 3	1	0.750±0.119	0.716±0.098	0.106
		2	0.738±0.102	0.706±0.086	0.062
	Method 4	1	0.715±0.097	0.697±0.079	0.614
		2	0.699±0.078	0.707±0.091	0.887

The fixed effects of GLMMs for CRAE at two visits and the difference between them are summarized in Table 5.2. In this table, Estimate is the parameter of each variable that explains the predicted value. P-value reflects the significance of the parameter, thus the significance of the variable or the interaction of two variables. CRAE of patients and controls measured by these four methods at V1, V2 and V2-V1 are in Figures 5.6, 5.7 and 5.8. To be noted that the lines in these figures show the differences between patients and controls at different points of time, instead of changes of subjects over the timeline.

Table 5.2 shows that for CRAE, with adjustment there is no significant difference between patients and controls on V1, V2 and V2-V1 in general. However, different opinions are drawn about the vessel difference of V2 and V1 between patients and controls from Method 2 and Method 4(P-value of 0.021). It indicates that for CRAE measured using Method 2, controls decrease more than patients from V1 to V2, yet controls decrease less than patients using Method 4 (see Figure 5.8). As a matter of fact, only Method 2 shows that controls decrease more than patients, and the rest of three methods indicate controls decrease less. However, none of these methods show a significant difference between controls and patients. Table 5.3 shows the difference of the decrease of CRAE between patients and controls measured by four methods, as well as the significance of the difference. Among all variables, age is the most influential factor of CRAE at both V1 and V2. It indicates that CRAE decreases as age increases at both V1 and V2. However, age does not effect the vessel changes between V1 and V2. It is probably because it is only two years between the

Table 5.2: Fixed effects of three linear mixed effect models on CRAE at visit 1, visit 2, and the difference between the two visits (Method 1 = the root-based method, Method 2 = the tree-based, Method 3 (M 3) = the conventional method on automatic A/V trees and Method 4 (M 4) = the conventional method on manual A/V trees).

	Visit 1		Visit 2		Visit 2 - Visit 1	
	Estimate (95% CI)	P-value	Estimate (95% CI)	P-value	Estimate (95% CI)	P-value
Intercept	8.368 (7.047,9.688)	$< .0001$	8.5546 (7.506,9.603)	$< .0001$	-0.05190 (-1.466,1.362)	0.942
Method 1 (Ref = M 4)	0.198 (-0.788,1.183)	0.693	0.119 (-0.698,0.936)	0.774	0.148 (-0.977,1.275)	0.795
Method 2 (Ref = M 4)	0.681 (-0.304,1.667)	0.175	0.276 (-0.541,1.093)	0.506	-0.360 (-1.486,0.766)	0.529
Method 3 (Ref = M 4)	-0.036 (-1.021,0.950)	0.943	0.466 (-0.350,1.284)	0.262	0.715 (-1.486,0.766)	0.212
Patient (Ref=control)	0.259 (-0.100,0.619)	0.157	0.002 (-0.285,0.289)	0.989	-0.231 (-0.621,0.157)	0.243
Patient∗ Method 1	-0.213 (-0.483,0.058)	0.123	-0.172 (-0.395,0.050)	0.129	0.032 (-0.280,0.344)	0.841
Patient∗ Method 2	-0.157 (-0.427,0.113)	0.254	0.213 (-0.009,0.437)	0.060	0.369 (0.057,0.682)	**0.021**
Patient∗ Method 3	-0.209 (-0.479,0.062)	0.130	-0.166 (-0.389,0.056)	0.143	0.017 (-0.294,0.330)	0.910
Age	-0.025 (-0.048,-0.001)	**0.033**	-0.028 (-0.046,-0.010)	**0.002**	0.001 (-0.023,0.025)	0.942
Age∗ Method 1	-0.002 (-0.019,0.015)	0.821	-0.002 (-0.016,0.011)	0.736	-0.004 (-0.024,0.015)	0.651
Age∗ Method 2	-0.013 (-0.030,0.004)	0.154	-0.014 (-0.028,0.000)	**0.049**	-0.003 (-0.023,0.016)	0.745
Age∗ Method 3	0.003 (-0.014,0.020)	0.734	-0.007 (-0.021,0.0067)	0.308	-0.014 (-0.034,0.005)	0.163

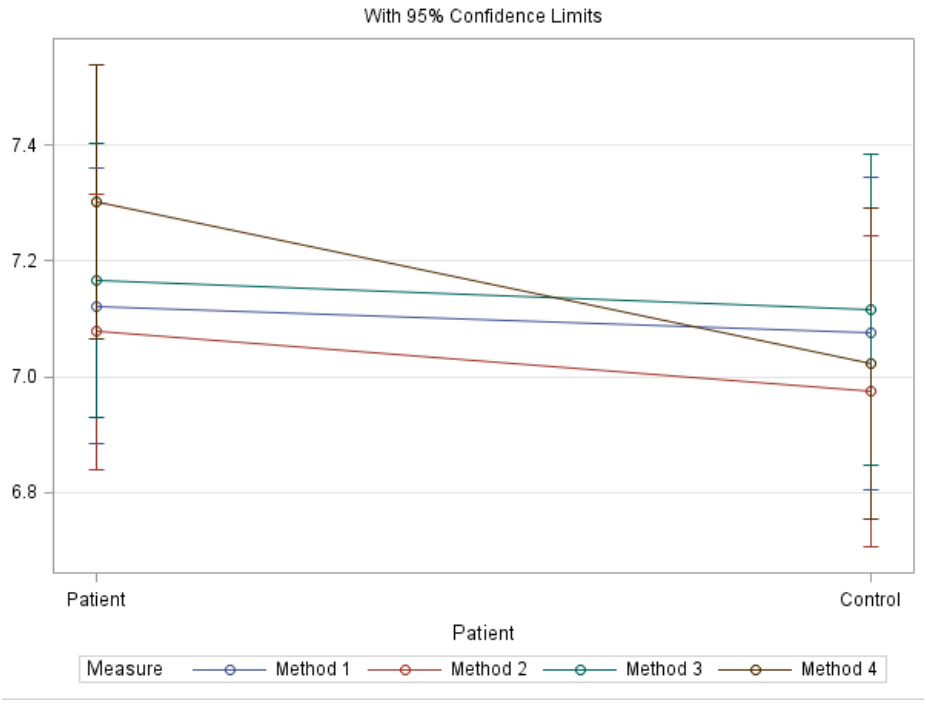

Figure 5.6: The mean CRAE of patients and controls at Visit 1 (Method 1 = the root-based method, Method 2 = the tree-based method, Method 3 = the conventional method based on automatic A/V trees, and Method 4 = the conventional method based on manually corrected A/V trees).

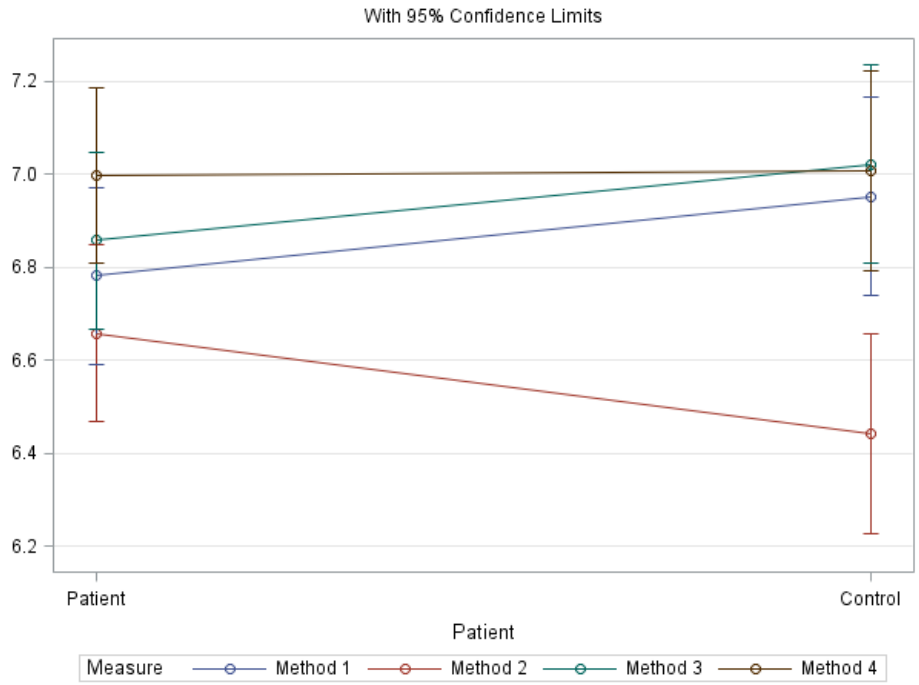

Figure 5.7: The mean CRAE of patients and controls at Visit 2.

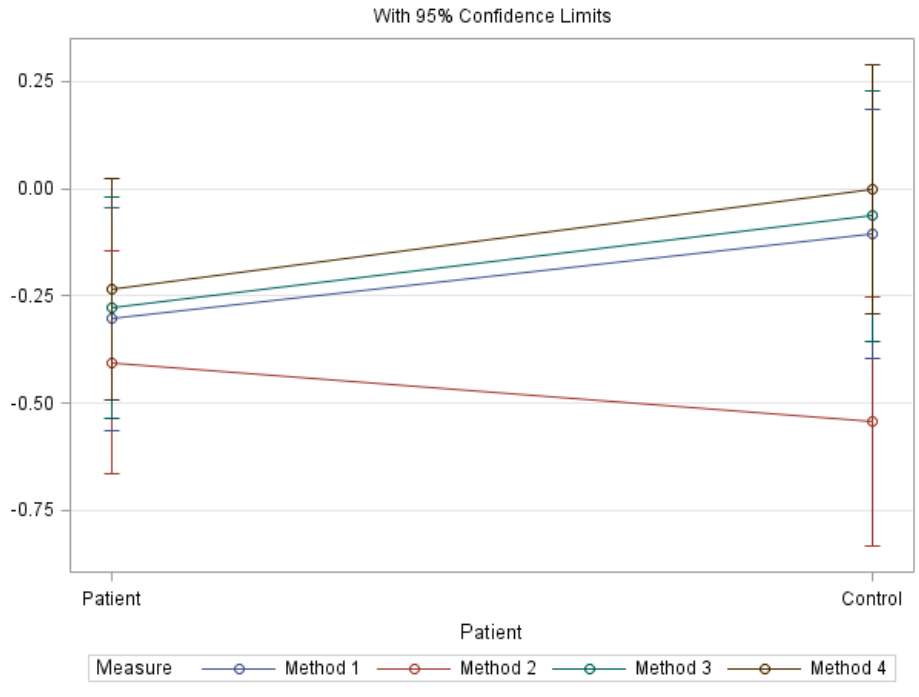

Figure 5.8: The difference of CRAE between V 2 and V 1 for patients and controls.

two visits. It is also noteworthy that Method 2 shows the influence of age better among other three methods, with P-values of 0.154 at V1 and 0.049 at V2 being better than Method 4.

Table 5.3: The difference of CRAE changes via two visits (Visit 2 minus Visit 1) between patients and controls (patients minus controls), measured by four methods.

	Method 1	Method 2	Method 3	Method 4
Estimate	−0.200	0.137	−0.214	−0.256
P-value	0.316	0.490	0.284	0.199

The fixed effects of GLMMs for CRVE at two visits and the difference between them are summarized in Table 5.4. CRVE of patients and controls measured by these four methods at V1, V2 and V2-V1 are in Figures 5.9, 5.10 and 5.11.

Table 5.4 shows that with adjustment for CRVE there is no significant difference between patients and controls at Visit 1 from four methods. Patients have slightly larger CRVE, but not significantly (P-value of 0.088). At Visit 2, patients and controls have similar values from Method 1, Method 3 and Method 4. However from Method 2, patients have larger CRVE than controls (P-Value of 0.009). It also shows that different conclusions about the changes of CRVE from V1 to V2 for patients and controls can be drawn based on different methods. Method 1, 3 and 4

Table 5.4: Fixed effects of three linear mixed effect models on CRVE at visit 1, visit 2, and the difference between the two visits (Method 1 = the root-based method, Method 2 = the tree-based, Method 3 (M 3) = the conventional method on automatic A/V trees and Method 4 (M 4) = the conventional method on manual A/V trees)

	Visit 1		Visit 2		Visit 2 - Visit 1	
	Estimate (95% CI)	P-value	Estimate (95% CI)	P-value	Estimate (95% CI)	P-value
Intercept	11.028 (9.231,12.825)	< .0001	11.436 (9.971,12.901)	< .0001	-0.009 (-2.012,1.994)	0.993
Method 1 (Ref = M 4)	-0.189 (-1.581,1.201)	0.788	-0.363 (-1.491,0.765)	0.527	-0.048 (-1.645,1.549)	0.953
Method 2 (Ref = M 4)	0.615 (-0.775,2.006)	0.385	-0.179 (-1.307,0.949)	0.755	-0.538 (-2.135,1.059)	0.508
Method 3 (Ref = M 4)	-0.080 (-1.471,1.311)	0.909	-0.501 (-1.630,0.626)	0.382	-0.230 (-1.828,1.366)	0.776
Patient (Ref=control)	0.426 (-0.063,0.917)	0.088	-0.057 (-0.458,0.344)	0.780	-0.395 (-0.947,0.156)	0.159
Patient∗ Method 1	-0.014 (-0.397,0.367)	0.939	0.262 (-0.046,0.571)	0.095	0.333 (-0.111,0.776)	0.141
Patient∗ Method 2	-0.145 (-0.527,0.236)	0.455	0.408 (0.101,0.717)	**0.009**	0.505 (0.062,0.948)	**0.025**
Patient∗ Method 3	0.0222 (-0.359,0.404)	0.909	0.144 (-0.163,0.453)	0.356	0.164 (-0.279,0.607)	0.468
Age	-0.020 (-0.052,0.011)	0.200	-0.023 (-0.048,0.001)	0.062	0.003 (-0.032,0.038)	0.867
Age∗ Method 1	-0.001 (-0.025,0.024)	0.968	-0.001 (-0.021,0.017)	0.845	-0.004 (-0.032,0.024)	0.778
Age∗ Method 2	-0.014 (-0.038,0.011)	0.268	-0.010 (-0.030,0.008)	0.270	-0.002 (-0.030,0.026)	0.902
Age∗ Method 3	-0.003 (-0.027,0.022)	0.829	0.0020 (-0.017,0.021)	0.838	0.001 (-0.027,0.029)	0.933

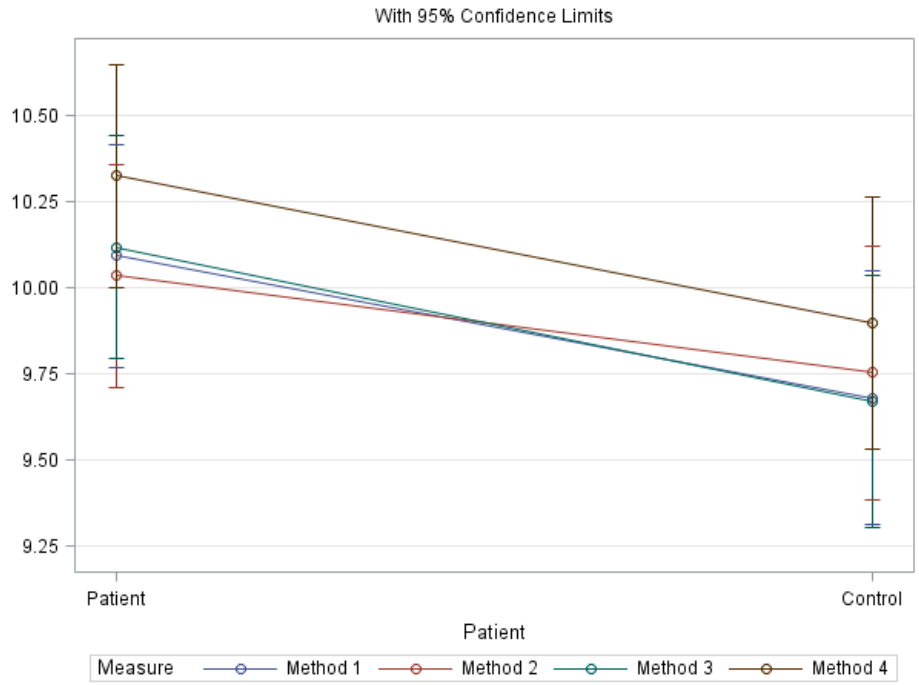

Figure 5.9: The mean CRVE of patients and controls at Visit 1.

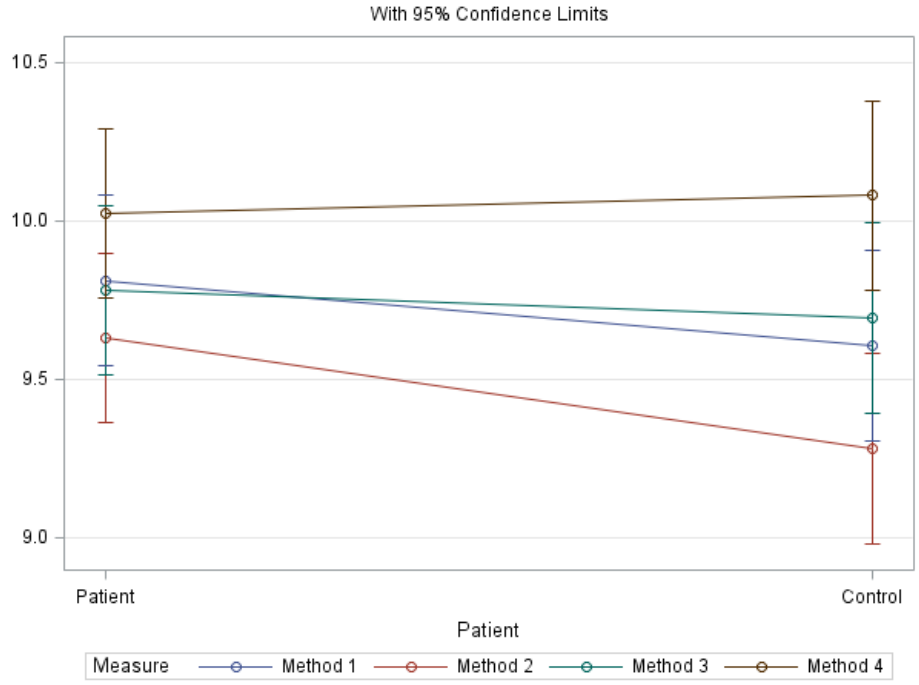

Figure 5.10: The mean CRVE of patients and controls at Visit 2.

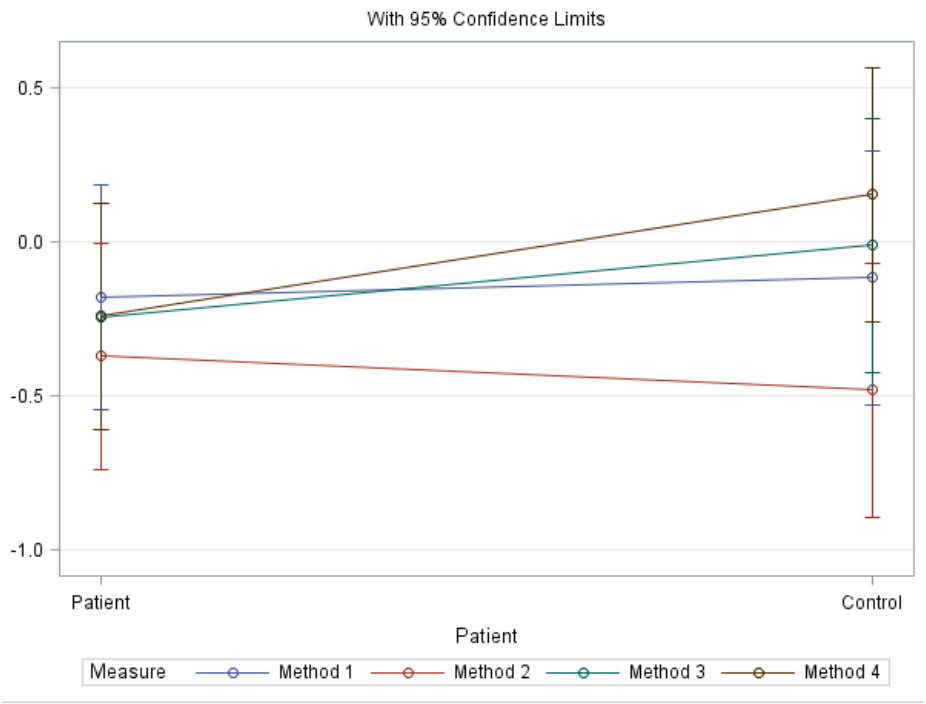

Figure 5.11: The difference of CRVE between V 2 and V 1 for patients and controls.

show that patients have larger decrease in CRVE between V1 and V2, compared to controls. Method 2 shows the contrary trend. This can be observed on figure 5.11 too. However, none of these trends reach significance. Age is still a negative factor of CRVE at both visits, but not significantly. At Visit 2, the effect of age is very close to significance (P-value of 0.062). Among four methods, Method 2 indicates the age factor best, but not significantly (P-value of 0.268 at Visit 1 and P-value of 0.270 at Visit 2).

The fixed effects of GLMMs for AVR at two visits and the difference between them are summarized in Table 5.5. AVR of patients and controls measured by these four methods at V1, V2 and V2-V1 are in Figures 5.12, 5.13 and 5.14.

Table 5.5: Fixed effects of three linear mixed effect models on AVR at visit 1, visit 2, and the difference between the two visits (Method 1 = the root-based method, Method 2 = the tree-based, Method 3 (M 3) = the conventional method on automatic A/V trees and Method 4 (M 4) = the conventional method on manual A/V trees)

	Visit 1		Visit 2		Visit 2 - Visit 1	
	Estimate (95% CI)	P-value	Estimate (95% CI)	P-value	Estimate (95% CI)	P-value
Intercept	0.787 (0.652,0.923)	< .0001	0.763 (0.650,0.877)	< .0001	-0.018 (-0.172,0.135)	0.8115
Method 1 (Ref = M 4)	0.039 (-0.084,0.164)	0.530	0.053 (-0.059,0.167)	0.353	0.027 (-0.134,0.189)	0.738
Method 2 (Ref = M 4)	0.001 (-0.123,0.125)	0.984	0.043 (-0.069,0.157)	0.449	0.024 (-0.136,0.186)	0.762
Method 3 (Ref = M 4)	-0.003 (-0.127,0.121)	0.961	0.093 (-0.020,0.207)	0.107	0.102 (-0.059,0.263)	0.213
Patient (Ref=control)	-0.009 (-0.046,0.028)	0.628	-0.001 (-0.032,0.029)	0.934	0.004 (-0.037,0.047)	0.819
Patient∗ Method 1	-0.023 (-0.057,0.011)	0.188	-0.028 (-0.059,0.003)	0.075	-0.011 (-0.055,0.033)	0.625
Patient∗ Method 2	-0.003 (-0.037,0.031)	0.840	-0.002 (-0.033,0.029)	0.886	0.005 (-0.039,0.050)	0.819
Patient∗ Method 3	-0.024 (-0.058,0.010)	0.168	-0.029 (-0.060,0.002)	0.064	-0.012 (-0.056,0.033)	0.604
Age	-0.001 (-0.004,0.001)	0.286	-0.001 (-0.003,0.001)	0.256	0.000 (-0.003,0.003)	0.944
Age∗ Method 1	0.000 (-0.002,0.002)	0.885	0.000 (-0.002,0.002)	0.734	0.000 (-0.003,0.002)	0.777
Age∗ Method 2	0.000 (-0.002,0.002)	0.899	-0.001 (-0.003,0.001)	0.456	-0.001 (-0.004,0.002)	0.644
Age∗ Method 3	0.001 (-0.001,0.003)	0.546	0.001 (-0.003,0.001)	0.336	-0.002 (-0.005,0.001)	0.234

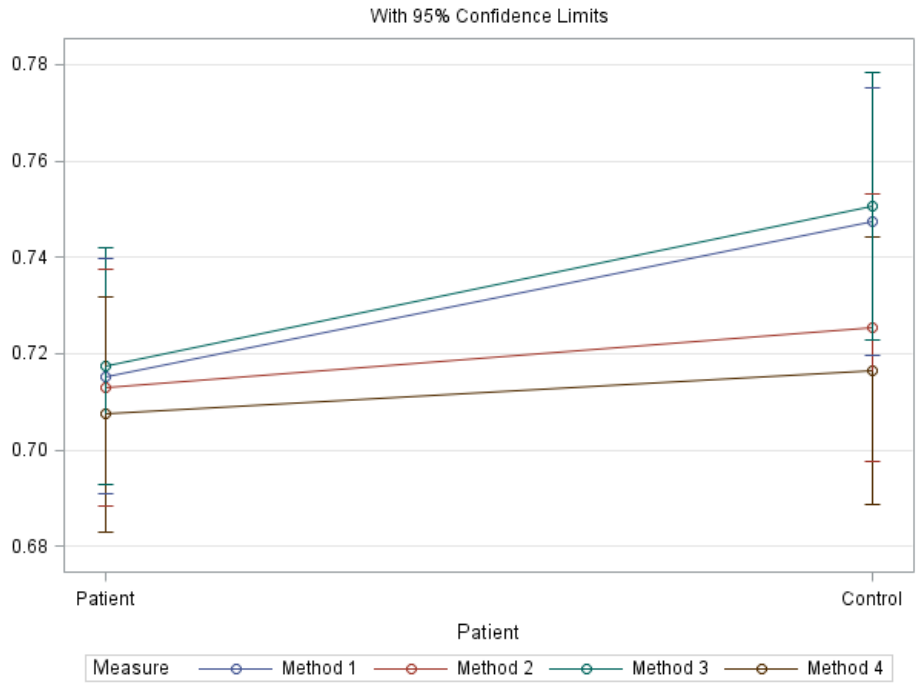

Figure 5.12: The mean AVR of patients and controls at Visit 1.

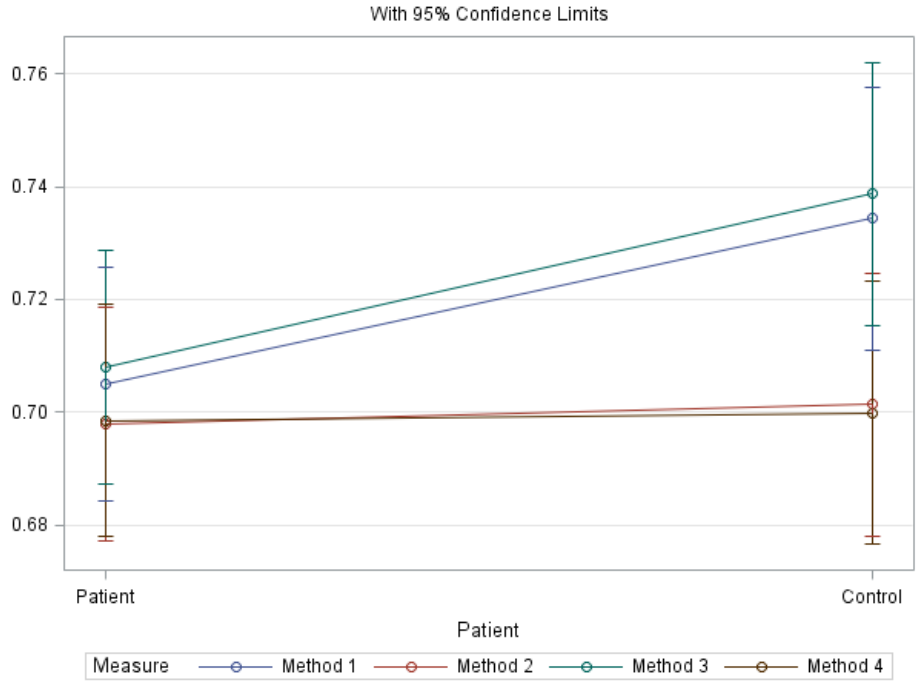

Figure 5.13: The mean AVR of patients and controls at Visit 2.

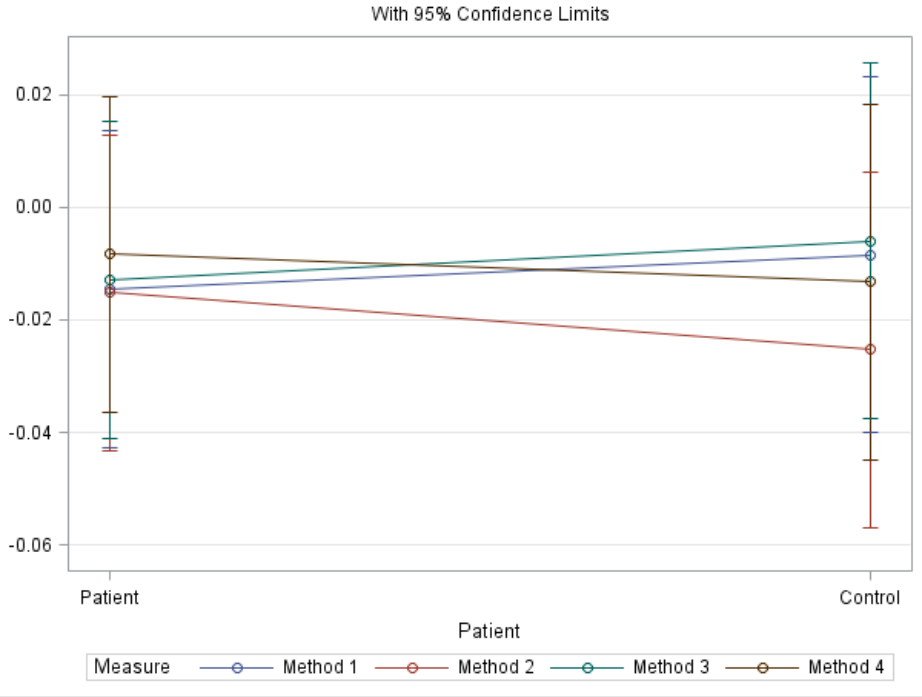

Figure 5.14: The difference of AVR between V 2 and V 1 for patients and controls.

Table 5.5 shows that with adjustment for AVR there is no difference between patients and controls at Visit 1, Visit 2, as well as the changes between the two visits. These four methods also shows consistence on this observation. The only exception is for Method 3, patients have smaller AVR than controls at Visit 2. However this observation does not reach significance (P-value of 0.064).The age have not effects on the changes of AVR for patients neither, which is observed by measurements from all four methods.

5.6 Discussion

From the results, we can see that in general, these four methods show very similar conclusions about the vessel widths of HIV-infected patients with HAART

treatment. Specifically, the results from Method 3 and Method 4 are very similar. This indicates that the conventional CRAE/CRVE method measuring on the automatic A/V trees has the same performance as measuring it on manually corrected A/V trees. This indicates that the conventional method can be measured using the A/V trees automatically built using the developed method in Chapter 4.

However, compared to the conventional method, the new methods reveal some different trends. Particularly, regarding CRAE, Method 2 or the tree-based method shows that controls have a larger decrease from Visit 1 to Visit 2, yet the other three methods shows the contrary trend. Both sides of conclusion however do not reach significance. This inclusive observations are consistent with some previous studies. Previous studies [58, 59] indicates that CRAE in patients decrease more rapidly than controls, possibly due to the effect of HAART treatment. However the study in [60] does not find this trend. In study [60] authors argue that this inconclusive opinions might due to the lengths of the treatments. In the studies of [58] and [59], the mean treatment length are 6.1 years and 58 months, and the median treatment length in the study of [60] is 7 months. Considering the treatment is two years in our dataset, it might be inconclusive whether CRAE of patients decrease more rapidly than controls.

The clear merit of the tree-based method comes from the strong indication of the effect of age. Previous studies [58, 59] show that CRAE decreases as age increases. This is confirmed by these four measurements. However the tree-based method shows the strongest effect of age, followed by the root-based method. We assume that the tree-based method is good at capturing this trend is because it

considers the widths of small vessels and vessels that are far from the OD, which are missed by the conventional method. These small vessels decrease the noise in the measurement of changes about the retinal vasculature.

Regarding CRVE, the tree-based method and the root-based method are very consistent with the conventional method. None of them find that there is a difference among the patients and the controls at visit 1. This is an inconclusive point since one previous study [59] finds that male patients have smaller CRVE than male controls, yet another previous study [60] (94.1% patients are males) finds that there is no difference in CRVE between patients and controls. The advantages of the tree-based method over the conventional method is that it shows larger CRVE at Visit 2 compared to controls. This is consistent with previous studies [58, 59] which claim that the higher viral load that comes with the HAART is associated with wider venular diameter. Another strength of the tree-based method is that it shows the strong effect of age on CRVE. Previous finding [58] indicates that the age is related to the decrease of CRVE. This trend is not significant in the four methods. However, the tree-based method shows the largest negative effect of age compared to other methods.

Regarding AVR, all four methods are very consistent with the changes of patients and controls between Visit 1 and Visit 2. There is no relation between age and AVR, which fits the fact that both CRAE and CRVE decreases as age increases. None of these methods find there is a difference between patients and controls at Visit 2, which is inconsistent with previous study [60] which claims that the HIV RNA viral loads are significantly associated with decreased AVR.

5.7 Conclusion

In summary, two novel methods to calculate CRAE/CRVE based on the automated constructed A/V trees are presented. One is a root-based method and another is a tree-based method. These two methods utilize the topological information from the A/V trees to transfer vessel widths into CRAE/CRVE. The two proposed methods are compared with a conventional method that calculates CRAE/CRVE based on the manually corrected A/V trees. Four methods are applied on a cohort study of HIV-infected patient who are receiving HAART treatment. Statistical analysis shows that the results from four methods are very similar and the conclusions drawn from them are mostly consistent. The tree-based method is better at indicating some important factors like age that influence the changes of retinal vessel widths, than the other three methods. Besides, one of the most important merits is that the tree-based method is totally automatic and thus it can be applied on large-scale data analysis.

CHAPTER 6
DISCUSSION

In this work, a novel method to automatically construct retinal arterial and venous trees on 2D fundus images is developed and evaluated. An application of the method in clinical data which is to measure and analyze the retinal vessel widths in HIV-infected patients is presented as well.

This work begins with a preliminary study to automatically localize and detect branches/bifurcations of the vasculature, which is presented in Chapter 3. As one of the most important structures in the retinal vasculature, bifurcations are the key of the construction of the vasculature since they determine the connections between vessels and thus the topology of the vasculature. The special shape of the bifurcation inspires us to use a machine learning approach to detect them by extracting the intensity and shape information and classifying them. A vision-machine method is used to extract the pixel information as the features and a kNN classifier is used for the classification task. The satisfying result shows the potential application of this methodology on other targets. However, the drawback of this method is that it only extracts local information to detect the bifurcations, yet the local information might be inaccurate or inadequate sometimes. As a result, this method would miss some small bifurcations and also mis-classify some crossing points whose shapes are similar to those of bifurcations.

To overcome the problem of limitation due to the local information, a novel and global method is developed to construct A/V trees automatically by taking ad-

vantages of topological and geometrical information of the retinal vasculature, which is presented in Chapter 4. Taking a vessel segmentation as the input, this method generates a vessel potential connectivity map (VPCM) first to over-connect nearby vessels. Then this over-connected vessel network is separated into binary overlapping trees that corresponds to arterial and venous trees. These binary overlapping trees, as well as independent trees which are not connected to any vessels, are classified into arterial and venous trees using a machine-learning approach.

The advantage of this method over existing approaches in the literature is that it uses more global information like the topology and geometry of the vasculature, combined with the local information like the intensity and vessel width and orientation to solve this problem. All of these information is combined together to make the decision by using a graph-based meta-heuristic algorithm. With the graph model, each bifurcation or crossing points are not determined solely by its nearby pixels, but also by the nearby bifurcations and crossing points, or all other bifurcations.

Another advantage is that this method is developed as a framework consisting of three main separated stages, the construction of the VPCM, the separation of the VPCM and the classification of trees. Each stage is a standalone process and thus can be further improved separately.

This framework is tested on multiple datasets on multiple experiments. It is tested on both manual vessel segmentation and various automatic vessel segmentation and the results shows its robustness with various of input, especially automatic vessel segmentation. The result is also compared with another method and it shows that the

developed method is slightly better in regarding of accuracy. In summary, experiments indicates its potential applicability on large datasets.

To demonstrate the application of this method and the constructed A/V trees, it is used to analyze the vessel widths of HIV-infected patients under treatment, which is presented in Chapter 5. To facilitate automation of the measurement, new methods to quantify the vessel widths are developed based on the A/V trees generated by taking the advantages of the topological information carried by the constructed A/V trees. New methods of quantifying vessel widths are compared with a conventional method. Statistical analysis reveals that the results generated by these methods are similar and consistent with previous studies. The conforming with previous studies indicates that the applicability of this new method of quantifying vessel widths. Meanwhile it shows that the automatic method of constructing A/V trees has great applicability for analyzing the retinal vasculature.

However, due to the limit of time, there are some limitations of this work and some aspects of it can be improved and further studied. The limitations will be discussed in the following text and the future work will be presented.

6.1 Limitations

The limitations of this work mainly comes from the limitations of the core part of this work: the automated approach to construct A/V trees.

The first limitation of this method is that the whole process of automatic constructing A/V trees from an fundus image is not scale-free. For the experiments in

this work, images are inspected before and are resized into a proper scale for further processing. This scale-correction prevents the real fully automatic construction of A/V trees and further analysis. The scale-invariance is not realized in this procedure for several reasons.

The first reason is that the automatic vessel segmentation is not scale-free. Most of vessel segmentation algorithms only yield good results under a specific scale or a range of scales, and good vessel segmentation (not largely over-segmented or largely under-segmented) is an important factor for the algorithm to generate a good result.

The second reason is that the developed algorithm is not fully scale-invariant. Specifically among the three stages of this framework, the construction of VPCM is not scale-invariant. During the construction of a VPCM, for each end point of vessel, a search effort is made to find its potential neighbors in order to build proper neighborhoods. The search effort is realized in the form of the search region, and its size is not scale-free. If the search region is too small, it might fail to find potential neighbors, which would also happen for largely under-segmented images. If the search region is too large, it might find too many neighbors which could generate many invalid cycles, which would also happen for largely over-segmented images. The second part is the localization of the OD and the detection of the fovea. The method used is a machine-learning method with a template matching strategy. Since the template has only a single scale, and the training stage only includes one dataset with a single scale, the machine-learning method is not multi-scale. If the size of the OD is too

small or too large, the accuracy might be decreased dramatically.

The second limitation of the method is that the overlapping of two parallel vessels (an arteriole and a venule) is not yet solved. The case often happens at regions close to the OD and there would be a large overlapping between vessels of two types. In this developed method, this large overlapping vessel is replaced by a large neighborhood, thus the overlapping part is similar to a black box that does not have effect on the final solution of the A/V trees. So the label of the overlapping part is assigned randomly by the developed algorithm. However, in reality, especially for the analysis of the A/V trees, for example the vessel width or the angles of bifurcations, there is a need to determine the connectivity and types of vessels for the overlapping part.

6.2 Future Work

Some parts of this work can be further extended and studied, which are roughly separated into two aspects. One is to improve the performance of the automatic construction of A/V trees. Another is to further apply the result of A/V tree for retinal vasculature analysis.

6.2.1 Improvement of the A/V Tree Construction Framework

The first part is to increase the scale-invariance of this framework. One possible solution is to use some outstanding target in the fundus image, usually the OD as the reference to determine the scale for the image. Then the scale is passed to the approach so that the parameters in the approach could be properly scaled.

The second part is to use a more advanced method to calculate the costs of configurations of each neighborhood (landmark). Specifically, currently multiple types of local information are used together to calculate the costs (probabilities) of configurations in the developed method. However this local information is modeled with hand-designed methods and parameters are hand-tuned. Some of these models might be better built using machine-learning methods. For example, the intensity information can be used to build a local classifier to assign a probability for each vessel within a neighborhood to be artery or vein. And this probability can be integrated into the cost function for the configurations of the neighborhood.

Another part of future work could be focused on working on determining vessels within large neighborhoods. As explained previously in the limitations, overlapping vessels within a neighborhood is not determined by the proposed algorithm. This information might be useful sometimes for the retinal vasculature analysis. To determine the types of vessels within a neighborhood, the vessels connected by this neighborhood can be used as reference to determine them. The intensity information can be used as a reference to classify the vessels within. Besides, the smoothness of boundaries between connected vessels can be used as a criteria too.

6.2.2 Application of the A/V Tree Construction Framework

Based on the A/V trees constructed using the developed method, more analysis of the retinal vasculature can be conducted besides the vessel widths. The calculation of a few biomarkers in clinics could benefit from the A/V trees constructed, such as

the tortuosity, the branching angle and the branch coefficient. Tortuosity measures how twisted a vessel is. A larger tortuosity value indicates a more twisted vessel. The branching angle is defined as the first angle subtended between two daughter vessels at each bifurcation. The branch coefficient is the ratio of the square of the width of parent vessels and the sum of squares of the widths of children vessels at each bifurcation. Moreover, with constructed A/V trees, some of these measurements which currently are only obtained on general vessel level would be able to be gathered on arterial and venous trees separately.

Another potential application of this method is to help with the detection of isolated abnormalities that have a similar appearance to vessels on the retina. For example, some abnormalities, such as hemorrhages, share similar intensity with vessels and they might be difficult to differentiate from vessels if they have similar vessel-like shape or are connected to vessels, using solely machine-learning methods. Using our method to detect the A/V trees, these isolated abnormalities might be detected with higher accuracy.

CHAPTER 7
CONCLUSION

To summarize, a thorough study of the construction of A/V trees on fundus photographs is conducted as specific aims proposed in the beginning of the work, as recalled as the following:

- Aim 1: To develop and evaluate an automatic approach for the detection and localization of retinal vessel branches using a vision-machine approach.
- Aim 2: To develop and formulate a framework to solve the binary overlapping trees problem using a graph-based model, and to apply it to construct A/V trees in fundus photographs.
- Aim 3: Based on Aim 2, given the constructed A/V trees in fundus photographs, to develop metrics to measure and analyze the width of A/V trees in clinics.

Chapter 3 introduces a machine learning method to detect and localize an important type of landmarks in the retinal vasculature, bifurcations on fundus images. It is evaluated on a dataset and the result is good, but not outstanding, thus indicating the need of a more global method to construct the retinal vasculature using both local and global information.

Chapter 4 introduces a novel and global framework to construct A/V trees on fundus images. In order to solve this problem, a novel algorithm to separate binary overlapping trees is developed. Then a framework that integrates the vessel segmentation, the OD and the fovea detection, and the local neighborhood cost calculation,

and this developed algorithm, and vessel classification is developed to construct A/V trees on fundus images. A benchmark is constructed to evaluate the method and is published for open comparison. The comparison with another method indicates its better performance.

Chapter 5 introduces a novel metric to analyze the width of the retinal vasculature based on A/V trees constructed by the framework in Chapter 4. The novel metric is used to analyze a cohort study of HIV-infected patients with HAART treatment. It compares the new metric with the conventional one and the comparison shows the consistency thus indicates the applicability of the new metric and the framework in Chapter 4.

In summary, the aims of this thesis are fulfilled. The developed method has a good performance and a wide applicability on clinical data.

APPENDIX A
THE GENERATION OF VESSEL SEGMENTS

This appendix describes the methods to separate vessel skeleton into disconnected vessel segments.

First of all, the vessel skeleton is pruned such that spurs (branches shorter than 3 pixels) are removed. Besides, in case that different skeletonization algorithms have different results, to unify the skeletonization generated from different algorithms, we remove some special vessel pixels if there is any in the vessel skeleton. For a vessel pixel, if there are two vessel pixels within its 3×3 neighborhood and the two pixels are distributed in any examples of Figure A.1, the vessel pixel is removed.

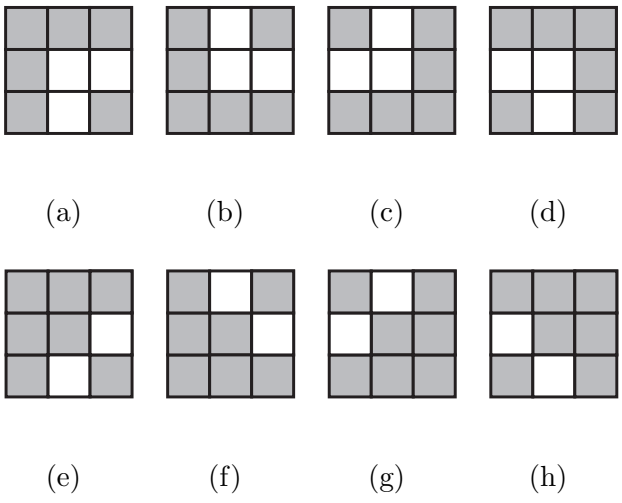

Figure A.1: The complete cases of special vessel points which are removed.

Then we find every vessel segment by finding the two ends as described in the following steps. The first step is to find normal vessel points and critical points and to categorize critical points according to the number of vessel pixels n within the 3 $\times$ 3 neighborhood. Denote n as the number vessel pixels in the 3×3 neighborhood. Vessel points are vessel pixels with $n = 2$. Other vessel pixels are considered as critical points. If $n = 1$, they are defined as vertex points. If $n = 3$, they are defined as red points. If $n = 4$, they are defined as green points. If $n = 5$, they are defined as blue points.

For any vertex points, they are considered as an endpoint of one vessel segment.

For a red point, if it has 3 vessel points within the 3×3 neighborhood, it is considered as endpoints for three vessel segments (See Figure A.2(a)); if it has 2 vessel points, it is considered as endpoints for two vessel segments (see Figure A.2(b)); if it has 1 vessel point, it is considered as an endpoint of one vessel segment (see Figure A.2(c)); if it has 0 vessel points, it is ignored and deleted (see Figure A.2(b)).

For a green point, if it has 4 vessel points within $3\times$ 3 neighborhood, it is considered as endpoints for four vessel segments (See Figture A.3(a)); if it has 3 vessel points, it is considered as endpoints for three vessel segments (see Figure A.3(b)); if it has 2 vessel points, it is considered as endpoints for two vessel segments (see Figure A.3(c)); if it has 1 vessel point, it is considered as an endpoint for one vessel segments (see Figure A.3(c)); if it has 0 vessel points, it is ignored and deleted (see Figure A.3(d)).

For a blue point, it is impossible to have more than 2 vessel points in a 3×3

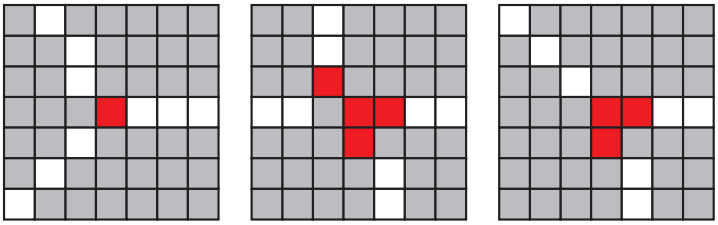

(a) (b) (c)

Figure A.2: Different cases of red critical points. (a) A red point with three vessel points. (b) The upper-left red point which is with two vessel points, and the center red point which is with 0 vessel points. (c) Three red points with one vessel point.

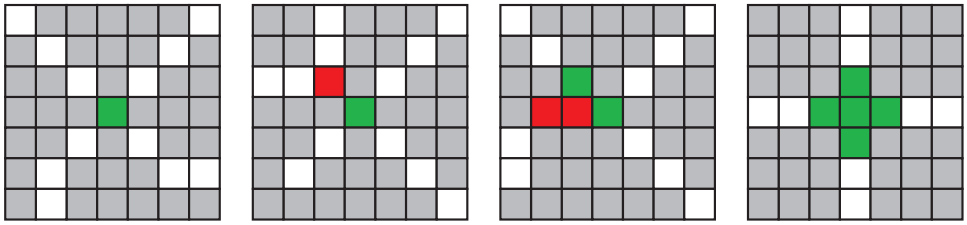

(a) (b) (c) (d)

Figure A.3: Different cases of green critical points. (a) A green point with four vessel points. (b) A green point with three vessel point. (c) The center green point which is with two vessel points, and the upper-left green point which is with one vessel point. (d) The center green point which is with zero vessel points, and four green points with one vessel point shown around it.

neighborhood. If it has 2 vessel points, it is considered as endpoints for two vessel segments (see Figure A.4(a)); If it has 1 vessel point, it is considered as an endpoint for one vessel segment (see Figure A.4(c)); If it has 0 vessel points, it is ignored and deleted (see Figure A.4(b)).

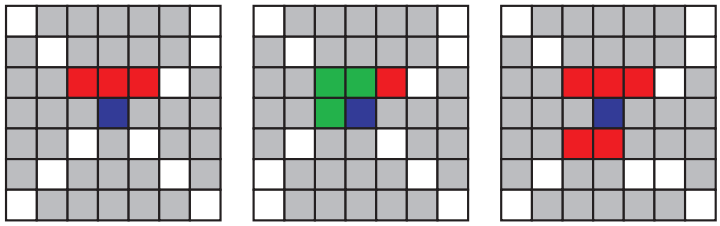

(a) (b) (c)

Figure A.4: Different cases of blue critical pints. (a) A blue point with two vessel points. (b) A blue point with one vessel point. (c) A blue point with zero vessel points.

After finding normal vessel points and critical points, we transfer critical points into end points of vessel segments. A critical point is transferred into the number of end points as the number vessel points in the 3×3 neighborhood. After collecting all the end points and vessel points, we start from an arbitrary end point and iteratively find the next vessel point in the 3×3 neighborhood to build a vessel segment, until we find another end point. After a vessel segment is built, its two end points are removed from the set of end points. The construction of vessel segments ends when

there is no end point. The example of segments with end points built from Figure A.3 is shown in Figure A.5.

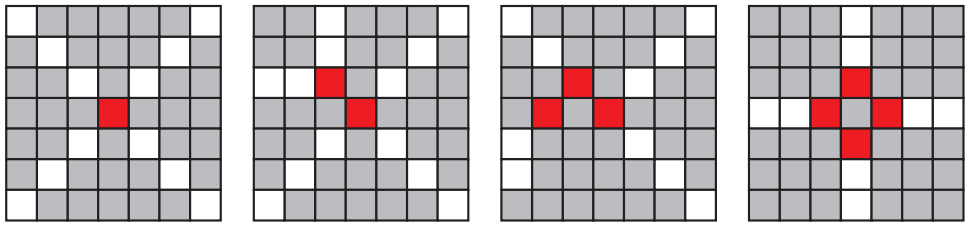

(a) (b) (c) (d)

Figure A.5: Examples of end points shown in red, built from critical points in Figure A.3.

Because some of segments share the same end point, to uniquely identify vessel segments with their two end points, we remove the end points from segments that overlaps at the end point. The method is to for vessels sharing the end point, only the vessel with the shortest length keeps the end point, and the common end point is deleted from other segments. An example of segments with the end point modification from cases in Figure A.5 is shown in Figure A.6.

After vessel segments are built, we have a set of segments such that each segment v_i is uniquely associated with its two end points ep_{2i} and ep_{2i+1}. Then the next step is to find neighbors for each segment, which ultimately builds the vessel potential connectivity map (VPCM).

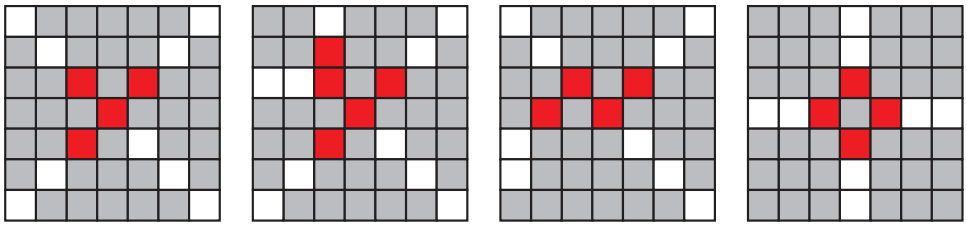

(a) (b) (c) (d)

Figure A.6: Examples of end points shown in red, after the removal of overlapping end points, built from examples in Figure A.5.

APPENDIX B
THE DETERMINATION OF VESSEL ORIENTATION

This appendix describes the methods to determine the vessel dominant orientations for segments, which are determined using multiple models together.

The first model is to use the root and leaf property. First of all, two special types of segments in a VPCM are introduced, the root segment, from which the trees start and the leaf segment, at which the trees end. There usually are multiple roots and leaves in a complex VPCM. For roots, their tails have no neighbors. For leaves, their heads have no neighbors. So we first find out all segments that have one end point without neighbors, then we classify them into roots and leaves using their distances to the OD. Roots are the ones closer to the OD, and leaves are the ones farther away from it. After we determine roots and leaves, we extend their labels to other segments using the following method. For a root or leaf, if its end point with neighbors has only one neighbor not already labeled as the same type, then the neighboring segment is also labeled as a root or leaf respectively. By this rule, we obtain a set of segments labeled as roots and leaves. When a segment is labeled as root or leaf, the dominant orientation is determined simultaneously, so as the labels of h and t for this segment. Figure B.1(b) shows root segments in red and leaf segments in yellow, for the fundus image in Figure B.1(a). Segments with dominant orientations determined with this model are shown in Figure B.1(c). Segments with dominant orientations determined are in green, and the head part is in red and the tail part is in yellow.

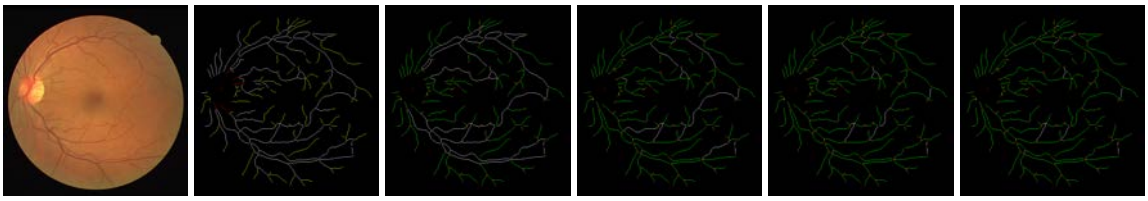

(a) (b) (c) (d) (e) (f)

Figure B.1: An example of determining dominant orientations. (a) A fundus image. (b) Vessel roots shown in red, and leaves shown in yellow. (c) Dominant orientations determined after using the root and leaf property. (d) Dominant orientations determined after using the second model. (e) Dominant orientations determined after using the parallel rule. (f) Dominant orientations determined after using the neighborhood connectivity.

The second model is to use the radial distribution of segments with respect to the OD. For a segment v_i, we calculate the displacement of its two end points as a unit vector denoted as $\mathbf{O_i}$. We also calculate the displacement of its center pixel to the OD as a unit vector $\mathbf{D_i}$. If the angle of $\mathbf{O_i}$ and $\mathbf{D_i}$ is smaller than a degree d, then the dominant orientation for v_i is determined and the endpoint near to the OD is t, and the other one is h. Figure B.1(d) shows the segments with dominant orientations determined after using this model.

The third model is the parallel model, which is only applied when there is a fovea in the image. The displacement of the fovea to the OD center is calculated as a unit vector, denoted as $\mathbf{D_{of}}$. For a segment v_i, if the angle between $\mathbf{O_i}$ and $\mathbf{D_{of}}$

is smaller than a degree d_{para}, the dominant orientation is determined, and the end point near to the OD is t, and the other one is h. Vessel segments with dominant orientation determined using this model are shown in Fig. B.1(e).

The fourth model is the rules of neighborhood connectivity, which are applied on the neighborhood level. Specifically we apply the rules mentioned at the end of section 4.2.4.1 for neighborhoods with size of 3, 4, 5 and 6. For neighborhoods with size of 3 and 4, there must be at least 1 h, or at most 2 h. For neighborhoods with size of 5 and 6, there must be 2 h and the rest are t. With these rules, we could label some u as h or t for some neighborhoods, thus determining the dominant orientation of the corresponding segments. Also we could rectify some possible errors made by previous models if there are more h in a neighborhood than these rules limit. The basic algorithm to determine a u to be a h or t is based on the direction information. We assume that in a neighborhood all heads are aligned together, and all tails are aligned in the opposite direction. For a u, if its associated end point direction is more aligned with other h, and more on the opposite direction of other t, then it is labeled as h; otherwise it is labeled as t. The same rule is applied to choose the extra h that should be changed to t. When there are three h in a neighborhood, one h (the h that deviates the most with other two h and is aligned the most with all other t) is changed to t. There are special cases that these rules cannot apply so we design different strategies or just leave them without any process. For example, when all end points are h or t, we break the neighborhood and disconnect every end point. For neighborhood of size 3, when there is one h, one t and one u, we do nothing.

For neighborhood of size 4, when there is one h, one t and two u, we do nothing. Fig. B.1(f) shows segments with dominant orientation determined after using these rules.

REFERENCES

[1] R. Doe. (2009, Jun.) Human Eye Anatomy. [Online]. Available: http://www.eyesandeyesight.com/2009/02/anatomy-of-the-eye/

[2] Wikipedia. (2003) Visual system: Light path. [Online]. Available: http://en.wikipedia.org/wiki/File:Eye-diagram.png

[3] Topcon. (2015) TRC-NW8F, fundus camera, topcon. [Online]. Available: http://www.topcon-medical.eu/eu/products/33-trc-nw8f-non-mydriatic-fundus-camera.html#images

[4] M. Niemeijer, J. Staal, B. van Ginneken, M. Loog, and M. D. Abràmoff, "Comparative study of retinal vessel segmentation methods on a new publicly available database," in *SPIE Medical Imaging*, vol. 5370, 2004, pp. 648–656.

[5] R. S. Snell, M. A. Lemp, and I. Grunther, *Clinical Anatomy of the Eye*. Blackwell Science, 1998.

[6] C. W. Oyster, *The Human Eye: Structure and Function*. Sinauer Associates, 1999.

[7] A. J. Bron, "Wolff's Anatomy of the Eye and Orbit," 1997.

[8] L. Sherwood, *Human Physiology: from Cells to Systems*. Thomson Brooks/Cole, 2012.

[9] M. D. Abràmoff, M. K. Garvin, and M. Sonka, "Retinal imaging and image analysis," *Biomedical Engineering, IEEE Reviews in*, vol. 3, pp. 169–208, 2010.

[10] A. C. Trigt, "Dissertatio ophthalmologica inauguralis de speculo oculi ejusque usu observation: comprobato," Ph.D. dissertation, PW van de Weijer, 1853.

[11] O. Gerloff, "Ueber die photographie des augenhintergrundes," *Klin Monatsblätter Augenheilkd*, vol. 29, pp. 397–403, 1891.

[12] A. Gullstrand, "Neue methoden der reflexlosen ophthalmoskopie," *Ber. Dtsch. Ophth. Ges*, vol. 36, p. 75, 1910.

[13] M. D. Abràmoff, J. C. Folk, D. P. Han, J. D. Walker, D. F. Williams, S. R. Russell, P. Massin, B. Cochener, P. Gain, L. Tang *et al.*, "Automated analysis of retinal images for detection of referable diabetic retinopathy," *JAMA Ophthalmology*, vol. 131, no. 3, pp. 351–357, 2013.

[14] W. H. O. Definition, "Diagnosis of diabetes mellitus and intermediate hyperglycemia: report of a WHO/IDF consultation," *Geneva: World Health Organization*, 2006.

[15] Centers for Disease Control and Prevention, *National diabetes fact sheet: national estimates and general information on diabetes and prediabetes in the United States, 2011.* Department of Health and Human Services, Centers for Disease Control and Prevention Atlanta, 2011.

[16] P. J. Kertes and T. M. Johnson, *Evidence-based Eye Care.* Lippincott Williams & Wilkins, 2006.

[17] T. A. Ciulla, A. G. Amador, and B. Zinman, "Diabetic retinopathy and diabetic macular edema pathophysiology, screening, and novel therapies," *Diabetes Care*, vol. 26, no. 9, pp. 2653–2664, 2003.

[18] D. C. Klonoff and D. M. Schwartz, "An economic analysis of interventions for diabetes." *Diabetes Care*, vol. 23, no. 3, pp. 390–404, 2000.

[19] R. J. Tapp, J. E. Shaw, C. A. Harper, M. P. de Courten, B. Balkau, D. J. McCarty, H. R. Taylor, T. A. Welborn, and P. Z. Zimmet, "The prevalence of and factors associated with diabetic retinopathy in the australian population," *Diabetes Care*, vol. 26, no. 6, pp. 1731–1737, 2003.

[20] R. Klein, B. E. Klein, S. E. Moss, and K. J. Cruickshanks, "The Wisconsin epidemiologic study of diabetic retinopathy: XVII: The 14-year incidence and progression of diabetic retinopathy and associated risk factors in type 1 diabetes," *Ophthalmology*, vol. 105, no. 10, pp. 1801–1815, 1998.

[21] R. Klein, B. E. Klein, and S. E. Moss, "How many steps of progression of diabetic retinopathy are meaningful?: The Wisconsin epidemiologic study of diabetic retinopathy," *Archives of Ophthalmology*, vol. 119, no. 4, pp. 547–553, 2001.

[22] Early Treatment Diabetic Retinopathy Study Research Group and others, "Grading diabetic retinopathy from stereoscopic color fundus photographsan extension of the modified airlie house classification: Etdrs report number 10," *Ophthalmology*, vol. 98, no. 5, pp. 786–806, 1991.

[23] T. T. Nguyen, J. J. Wang, and T. Y. Wong, "Retinal vascular changes in pre-diabetes and prehypertension new findings and their research and clinical implications," *Diabetes Care*, vol. 30, no. 10, pp. 2708–2715, 2007.

[24] C. D. Saudek, W. H. Herman, D. B. Sacks, R. M. Bergenstal, D. Edelman, and M. B. Davidson, "A new look at screening and diagnosing diabetes mellitus," *The Journal of Clinical Endocrinology & Metabolism*, vol. 93, no. 7, pp. 2447–2453, 2008.

[25] T. Y. Wong, R. Klein, A. R. Sharrett, M. I. Schmidt, J. S. Pankow, D. J. Couper, B. E. Klein, L. D. Hubbard, B. B. Duncan, ARIC Investigators *et al.*, "Retinal arteriolar narrowing and risk of diabetes mellitus in middle-aged persons," *JAMA*, vol. 287, no. 19, pp. 2528–2533, 2002.

[26] T. Y. Wong, A. Shankar, R. Klein, B. E. Klein, and L. D. Hubbard, "Retinal arteriolar narrowing, hypertension, and subsequent risk of diabetes mellitus," *Archives of Internal Medicine*, vol. 165, no. 9, pp. 1060–1065, 2005.

[27] M. K. Ikram, J. A. Janssen, A. M. Roos, I. Rietveld, J. C. Witteman, M. M. Breteler, A. Hofman, C. M. Van Duijn, and P. T. de Jong, "Retinal vessel diameters and risk of impaired fasting glucose or diabetes the Rotterdam Study," *Diabetes*, vol. 55, no. 2, pp. 506–510, 2006.

[28] S. Mendis, P. Puska, B. Norrving *et al.*, *Global Atlas on Cardiovascular Disease Prevention and Control*. World Health Organization, 2011.

[29] V. L. Roger, A. S. Go, D. M. Lloyd-Jones, E. J. Benjamin, J. D. Berry, W. B. Borden, D. M. Bravata, S. Dai, E. S. Ford, C. S. Fox *et al.*, "Heart disease and stroke statistics 2012 update a report from the american heart association," *Circulation*, vol. 125, no. 1, pp. e2–e220, 2012.

[30] T. Y. Wong, R. Klein, D. J. Couper, L. S. Cooper, E. Shahar, L. D. Hubbard, M. R. Wofford, A. R. Sharrett *et al.*, "Retinal microvascular abnormalities and incident stroke: the atherosclerosis risk in communities study," *Lancet*, vol. 358, no. 9288, pp. 1134–1140, 2001.

[31] T. Y. Wong, R. Klein, A. R. Sharrett, B. B. Duncan, D. J. Couper, J. M. Tielsch, B. E. Klein, and L. D. Hubbard, "Retinal arteriolar narrowing and risk of coronary heart disease in men and women," *JAMA: the Journal of the American Medical Association*, vol. 287, no. 9, pp. 1153–1159, 2002.

[32] T. Y. Wong, F. A. Islam, R. Klein, B. E. Klein, M. F. Cotch, C. Castro, A. R. Sharrett, and E. Shahar, "Retinal vascular caliber, cardiovascular risk factors, and inflammation: the multi-ethnic study of atherosclerosis (MESA)," *Investigative Ophthalmology & Visual Science*, vol. 47, no. 6, pp. 2341–2350, 2006.

[33] R. Klein, B. E. Klein, S. E. Moss, and Q. Wang, "Hypertension and retinopathy, arteriolar narrowing, and arteriovenous nicking in a population," *Archives of Ophthalmology*, vol. 112, no. 1, p. 92, 1994.

[34] R. Klein, B. E. Klein, and S. E. Moss, "The relation of systemic hypertension to changes in the retinal vasculature: the Beaver Dam Eye Study." *Transactions of the American Ophthalmological Society*, vol. 95, p. 329, 1997.

[35] M. Ikram, F. De Jong, M. Bos, J. Vingerling, A. Hofman, P. Koudstaal, P. De Jong, and M. Breteler, "Retinal vessel diameters and risk of stroke the Rotterdam Study," *Neurology*, vol. 66, no. 9, pp. 1339–1343, 2006.

[36] T. Y. Wong, A. Kamineni, R. Klein, A. R. Sharrett, B. E. Klein, D. S. Siscovick, M. Cushman, and B. B. Duncan, "Quantitative retinal venular caliber and risk of cardiovascular disease in older persons: the cardiovascular health study," *Archives of Internal Medicine*, vol. 166, no. 21, pp. 2388–2394, 2006.

[37] T. Y. Wong, A. Shankar, R. Klein, B. E. Klein, and L. D. Hubbard, "Prospective cohort study of retinal vessel diameters and risk of hypertension," *BMJ*, vol. 329, no. 7457, p. 79, 2004.

[38] L. D. Hubbard, R. J. Brothers, W. N. King, L. X. Clegg, R. Klein, L. S. Cooper, A. R. Sharrett, M. D. Davis, and J. Cai, "Methods for evaluation of retinal microvascular abnormalities associated with hypertension/sclerosis in the atherosclerosis risk in communities study," *Ophthalmology*, vol. 106, no. 12, pp. 2269–2280, 1999.

[39] M. K. Ikram, F. J. de Jong, J. R. Vingerling, J. C. Witteman, A. Hofman, M. M. Breteler, and P. T. de Jong, "Are retinal arteriolar or venular diameters associated with markers for cardiovascular disorders? the Rotterdam Study," *Investigative Ophthalmology & Visual Science*, vol. 45, no. 7, pp. 2129–2134, 2004.

[40] W. Smith, J. J. Wang, T. Y. Wong, E. Rochtchina, R. Klein, S. R. Leeder, and P. Mitchell, "Retinal arteriolar narrowing is associated with 5-year incident severe hypertension the blue mountains eye study," *Hypertension*, vol. 44, no. 4, pp. 442–447, 2004.

[41] T. T. Nguyen and T. Y. Wong, "Retinal vascular manifestations of metabolic disorders," *Trends in Endocrinology & Metabolism*, vol. 17, no. 7, pp. 262–268, 2006.

[42] M. K. Ikram, J. C. Witteman, J. R. Vingerling, M. M. Breteler, A. Hofman, and P. T. de Jong, "Retinal vessel diameters and risk of hypertension the Rotterdam Study," *Hypertension*, vol. 47, no. 2, pp. 189–194, 2006.

[43] A. D. Hughes, E. Martinez-Perez, A.-S. Jabbar, A. Hassan, N. W. Witt, P. D. Mistry, N. Chapman, A. V. Stanton, G. Beevers, R. Pedrinelli *et al.*, "Quantification of topological changes in retinal vascular architecture in essential and malignant hypertension," *Journal of Hypertension*, vol. 24, no. 5, pp. 889–894, 2006.

[44] L. King, A. Stanton, P. Sever, S. Thom, and A. Hughes, "Arteriolar length–diameter (l: D) ratio: a geometric parameter of the retinal vasculature diagnostic of hypertension," *Journal of Human Hypertension*, vol. 10, no. 6, pp. 417–418, 1996.

[45] A. V. Stanton, B. Wasan, A. Cerutti, S. Ford, R. Marsh, P. P. Sever, S. A. Thom, and A. D. Hughes, "Vascular network changes in the retina with age and hypertension." *Journal of Hypertension*, vol. 13, no. 12 Pt 2, p. 1724, 1995.

[46] P. Kutschbach, S. Wolf, M. Sieveking, T. H. Ittel, K. Schulte, and M. Reim, "Retinal capillary density in patients with arterial hypertension: 2-year follow-up," *Graefe's Archive for Clinical and Experimental Ophthalmology*, vol. 236, no. 6, pp. 410–414, 1998.

[47] C. Sun, J. J. Wang, D. A. Mackey, and T. Y. Wong, "Retinal vascular caliber: systemic, environmental, and genetic associations," *Survey of Ophthalmology*, vol. 54, no. 1, pp. 74–95, 2009.

[48] Joint United Nations Programme on HIV/AIDS (UNAIDS) and others, "Global report: UNAIDS report on the global AIDS epidemic 2013. geneva: UNAIDS, 2013," vol. 21, pp. 22–000, 2015.

[49] World Health Organization, "Global update on HIV treatment 2013: results, impact and opportunities," 2013. [Online]. Available: http://apps.who.int/iris/handle/10665/85326

[50] S. G. Deeks, S. R. Lewin, and D. V. Havlir, "The end of AIDS: HIV infection as a chronic disease," *The Lancet*, vol. 382, no. 9903, pp. 1525–1533, 2013.

[51] N. Friis-Møller, R. Weber, P. Reiss, R. Thiébaut, O. Kirk, A. d. Monforte, C. Pradier, L. Morfeldt, S. Mateu, M. Law *et al.*, "Cardiovascular disease risk factors in HIV patients–association with antiretroviral therapy. results from the DAD study," *AIDS*, vol. 17, no. 8, pp. 1179–1193, 2003.

[52] M. S. Freiberg, C.-C. H. Chang, L. H. Kuller, M. Skanderson, E. Lowy, K. L. Kraemer, A. A. Butt, M. B. Goetz, D. Leaf, K. A. Oursler *et al.*, "HIV infection and the risk of acute myocardial infarction," *JAMA Internal Medicine*, vol. 173, no. 8, pp. 614–622, 2013.

[53] R. Scherzer, M. Estrella, L. Yongmei, S. G. Deeks, C. Grunfeld, and M. G. Shlipak, "Association of tenofovir exposure with kidney disease risk in HIV infection," *AIDS (London, England)*, vol. 26, no. 7, p. 867, 2012.

[54] L. Ryom, A. Mocroft, O. Kirk, S. W. Worm, D. A. Kamara, P. Reiss, M. Ross, C. A. Fux, P. Morlat, O. Moranne *et al.*, "Association between antiretroviral exposure and renal impairment among HIV-positive persons with normal baseline renal function: the D: A: D study," *Journal of Infectious Diseases*, vol. 207, no. 9, pp. 1359–1369, 2013.

[55] J. V. Baker, K. Brummel-Ziedins, J. Neuhaus, D. Duprez, N. Cummins, D. Dalmau, J. DeHovitz, C. Lehmann, A. Sullivan, I. Woolley *et al.*, "HIV replication alters the composition of extrinsic pathway coagulation factors and increases thrombin generation," *Journal of the American Heart Association*, vol. 2, no. 4, p. e000264, 2013.

[56] A. E. Grulich, M. T. van Leeuwen, M. O. Falster, and C. M. Vajdic, "Incidence of cancers in people with HIV/AIDS compared with immunosuppressed transplant recipients: a meta-analysis," *The Lancet*, vol. 370, no. 9581, pp. 59–67, 2007.

[57] J. V. Baker, G. Peng, J. Rapkin, D. I. Abrams, M. J. Silverberg, R. D. MacArthur, W. P. Cavert, W. K. Henry, and J. D. Neaton, "CD4+ count and risk of non-AIDS diseases following initial treatment for HIV infection," *AIDS (London, England)*, vol. 22, no. 7, p. 841, 2008.

[58] S. Gangaputra, P. S. Kalyani, A. A. Fawzi, M. L. Van Natta, L. D. Hubbard, R. P. Danis, J. E. Thorne, and G. N. Holland, "Retinal vessel caliber among people with acquired immunodeficiency syndrome: Relationships with disease-associated factors and mortality," *American Journal of Ophthalmology*, vol. 153, no. 3, pp. 434–444, 2012.

[59] S. Pathai, H. A. Weiss, S. D. Lawn, T. Peto, L. M. D'Costa, C. Cook, T. Y. Wong, and C. E. Gilbert, "Retinal Arterioles Narrow with Increasing Duration of Anti-Retroviral Therapy in HIV Infection: A Novel Estimator of Vascular Risk in HIV?" *PLoS ONE*, vol. 7, no. 12, pp. 1–8, 2012.

[60] P. B. Tan, O. K. Hee, C. Cheung, T. K. Yeo, R. Agrawal, J. Ng, T. H. Lim, T. Y. Wong, and S. C. Teoh, "Retinal vascular parameter variations in patients with human immunodeficiency virus." *Investigative Ophthalmology & Visual Science*, vol. 54, no. 13, pp. 7962–7, 2013.

[61] N. Demirkaya, S. Cohen, F. W. Wit, M. D. Abràmoff, R. O. Schlingemann, T. W. Kuijpers, P. Reiss, D. Pajkrt, and F. D. Verbraak, "Retinal structure and function in perinatally HIV-infected and cART-treated children: A matched case–control study," *Investigative Ophthalmology & Visual Science*, vol. 56, no. 6, pp. 3945–3954, 2015.

[62] A. Bhuiyan, B. Nath, J. Chua, and R. Kotagiri, "Blood vessel segmentation from color retinal images using unsupervised texture classification," in *Image Processing, 2007. ICIP 2007. IEEE International Conference on*, vol. 5, 2007, pp. V–521.

[63] B. Y. Lam and H. Yan, "A novel vessel segmentation algorithm for pathological retina images based on the divergence of vector fields," *Medical Imaging, IEEE Transactions on*, vol. 27, no. 2, pp. 237–246, 2008.

[64] G. G. Gardner, D. Keating, T. H. Williamson, and A. T. Elliott, "Automatic detection of diabetic retinopathy using an artificial neural network: a screening tool." *British Journal of Ophthalmology*, vol. 80, no. 11, pp. 940–944, 1996.

[65] C. Sinthanayothin, J. F. Boyce, H. L. Cook, and T. H. Williamson, "Automated localisation of the optic disc, fovea, and retinal blood vessels from digital colour fundus images," *British Journal of Ophthalmology*, vol. 83, no. 8, pp. 902–910, 1999.

[66] J. Staal, M. D. Abràmoff, M. Niemeijer, M. A. Viergever, and B. van Ginneken, "Ridge-based vessel segmentation in color images of the retina," *Medical Imaging, IEEE Transactions on*, vol. 23, no. 4, pp. 501–509, 2004.

[67] J. V. Soares, J. J. Leandro, R. M. Cesar Jr, H. F. Jelinek, and M. J. Cree, "Retinal vessel segmentation using the 2-D Gabor wavelet and supervised classification," *Medical Imaging, IEEE Transactions on*, vol. 25, no. 9, pp. 1214–1222, 2006.

[68] M. Sofka and C. V. Stewart, "Retinal vessel centerline extraction using multiscale matched filters, confidence and edge measures," *Medical Imaging, IEEE Transactions on*, vol. 25, no. 12, pp. 1531–1546, 2006.

[69] E. Ricci and R. Perfetti, "Retinal blood vessel segmentation using line operators and support vector classification," *Medical Imaging, IEEE Transactions on*, vol. 26, no. 10, pp. 1357–1365, 2007.

[70] C. A. Lupascu, D. Tegolo, and E. Trucco, "FABC: retinal vessel segmentation using AdaBoost," *Information Technology in Biomedicine, IEEE Transactions on*, vol. 14, no. 5, pp. 1267–1274, 2010.

[71] D. Marn, A. Aquino, M. E. Gegndez-Arias, and J. M. Bravo, "A new supervised method for blood vessel segmentation in retinal images by using gray-level and moment invariants-based features," *Medical Imaging, IEEE Transactions on*, vol. 30, no. 1, pp. 146–158, 2011.

[72] A. F. Frangi, W. J. Niessen, K. L. Vincken, and M. A. Viergever, "Multiscale vessel enhancement filtering," in *Medical Image Computing and Computer-Assisted Interventation-MICCAI 98*. Springer, 1998, pp. 130–137.

[73] T. Lindeberg, "Edge detection and ridge detection with automatic scale selection," *International Journal of Computer Vision*, vol. 30, no. 2, pp. 117–156, 1998.

[74] O. Chutatape, L. Zheng, and S. M. Krishnan, "Retinal blood vessel detection and tracking by matched Gaussian and Kalman filters," in *Engineering in Medicine and Biology Society, 1998. Proceedings of the 20th Annual International Conference of the IEEE*, vol. 6, 1998, pp. 3144–3149.

[75] Y. A. Tolias and S. M. Panas, "A fuzzy vessel tracking algorithm for retinal images based on fuzzy clustering," *Medical Imaging, IEEE Transactions on*, vol. 17, no. 2, pp. 263–273, 1998.

[76] A. Can, H. Shen, J. N. Turner, H. L. Tanenbaum, and B. Roysam, "Rapid automated tracing and feature extraction from retinal fundus images using direct exploratory algorithms," *Information Technology in Biomedicine, IEEE Transactions on*, vol. 3, no. 2, pp. 125–138, 1999.

[77] L. Gagnon, M. Lalonde, M. Beaulieu, and M.-C. Boucher, "Procedure to detect anatomical structures in optical fundus images," in *Medical Imaging 2001*, 2001, pp. 1218–1225.

[78] I. Liu and Y. Sun, "Recursive tracking of vascular networks in angiograms based on the detection-deletion scheme," *Medical Imaging, IEEE Transactions on*, vol. 12, no. 2, pp. 334–341, 1993.

[79] L. Zhou, M. S. Rzeszotarski, L. J. Singerman, and J. M. Chokreff, "The detection and quantification of retinopathy using digital angiograms," *Medical Imaging, IEEE Transactions on*, vol. 13, no. 4, pp. 619–626, 1994.

[80] T. Walter and J.-C. Klein, "Segmentation of color fundus images of the human retina: Detection of the optic disc and the vascular tree using morphological techniques," *Medical Data Analysis*, pp. 282–287, 2001.

[81] F. Zana and J.-C. Klein, "Segmentation of vessel-like patterns using mathematical morphology and curvature evaluation," *Image Processing, IEEE Transactions on*, vol. 10, no. 7, pp. 1010–1019, 2001.

[82] A. M. Mendonca and A. Campilho, "Segmentation of retinal blood vessels by combining the detection of centerlines and morphological reconstruction," *Medical Imaging, IEEE Transactions on*, vol. 25, no. 9, pp. 1200–1213, 2006.

[83] S. Chaudhuri, S. Chatterjee, N. Katz, M. Nelson, and M. Goldbaum, "Detection of blood vessels in retinal images using two-dimensional matched filters," *Medical Imaging, IEEE Transactions on*, vol. 8, no. 3, pp. 263–269, 1989.

[84] A. D. Hoover, V. Kouznetsova, and M. Goldbaum, "Locating blood vessels in retinal images by piecewise threshold probing of a matched filter response," *Medical Imaging, IEEE Transactions on*, vol. 19, no. 3, pp. 203–210, 2000.

[85] L. Gang, O. Chutatape, and S. M. Krishnan, "Detection and measurement of retinal vessels in fundus images using amplitude modified second-order gaussian filter," *Biomedical Engineering, IEEE Transactions on*, vol. 49, no. 2, pp. 168–172, 2002.

[86] M. Al-Rawi and H. Karajeh, "Genetic algorithm matched filter optimization for automated detection of blood vessels from digital retinal images," *Computer Methods and Programs in Biomedicine*, vol. 87, no. 3, pp. 248–253, 2007.

[87] M. Al-Rawi, M. Qutaishat, and M. Arrar, "An improved matched filter for blood vessel detection of digital retinal images," *Computers in Biology and Medicine*, vol. 37, no. 2, pp. 262–267, 2007.

[88] M. G. Cinsdikici and D. Aydın, "Detection of blood vessels in ophthalmoscope images using MF/ant (matched filter/ant colony) algorithm," *Computer Methods and Programs in Biomedicine*, vol. 96, no. 2, pp. 85–95, 2009.

[89] X. Jiang and D. Mojon, "Adaptive local thresholding by verification-based multithreshold probing with application to vessel detection in retinal images," *Pattern Analysis and Machine Intelligence, IEEE Transactions on*, vol. 25, no. 1, pp. 131–137, 2003.

[90] B. Al-Diri, A. Hunter, and D. Steel, "An active contour model for segmenting and measuring retinal vessels," *Medical Imaging, IEEE Transactions on*, vol. 28, no. 9, pp. 1488–1497, 2009.

[91] L. Espona, M. Carreira, M. Ortega, and M. Penedo, "A snake for retinal vessel segmentation," *Pattern Recognition and Image Analysis*, pp. 178–185, 2007.

[92] M. E. Martinez-Perez, A. D. Hughes, S. A. Thom, A. A. Bharath, and K. H. Parker, "Segmentation of blood vessels from red-free and fluorescein retinal images." *Medical Image Analysis*, vol. 11, no. 1, p. 47, 2007.

[93] G. Coppini, M. Demi, R. Poli, and G. Valli, "An artificial vision system for x-ray images of human coronary trees," *Pattern Analysis and Machine Intelligence, IEEE Transactions on*, vol. 15, no. 2, pp. 156–162, 1993.

[94] P. Montesinos and L. Alquier, "Perceptual organization of thin networks with active contour functions applied to medical and aerial images," in *Pattern Recognition, 1996., Proceedings of the 13th International Conference on*, vol. 1, 1996, pp. 647–651.

[95] P. J. Yim, P. L. Choyke, and R. M. Summers, "Gray-scale skeletonization of small vessels in magnetic resonance angiography," *Medical Imaging, IEEE Transactions on*, vol. 19, no. 6, pp. 568–576, 2000.

[96] D. Selle, B. Preim, A. Schenk, and H. O. Peitgen, "Analysis of vasculature for liver surgical planning," *Medical Imaging, IEEE Transactions on*, vol. 21, no. 11, pp. 1344–1357, 2002.

[97] T. Deschamps and L. D. Cohen, "Grouping connected components using minimal path techniques," *Geometric Methods in Bio-Medical Image Processing*, pp. 91–106, 2002.

[98] J. Jomier, V. LeDigarcher, and S. Aylward, "Automatic vascular tree formation using the mahalanobis distance," *Medical Image Computing and Computer-Assisted Intervention–MICCAI 2005*, pp. 806–812, 2005.

[99] E. Bullitt, S. Aylward, A. Liu, J. Stone, S. Mukherji, C. Coffey, G. Gerig, and S. Pizer, "3D graph description of the intracerebral vasculature from segmented mra and tests of accuracy by comparison with x-ray angiograms," in *Information Processing in Medical Imaging*, 1999, pp. 308–321.

[100] H. Shen, B. Roysam, C. V. Stewart, J. N. Turner, and H. L. Tanenbaum, "Optimal scheduling of tracing computations for real-time vascular landmark extraction from retinal fundus images," *Information Technology in Biomedicine, IEEE Transactions on*, vol. 5, no. 1, pp. 77–91, 2001.

[101] E. Grisan, A. Pesce, A. Giani, M. Foracchia, and A. Ruggeri, "A new tracking system for the robust extraction of retinal vessel structure," in *Engineering in Medicine and Biology Society, 2004. IEMBS'04. 26th Annual International Conference of the IEEE*, vol. 1, 2004, pp. 1620–1623.

[102] M. E. Martinez-Perez, A. D. Highes, A. V. Stanton, S. A. Thorn, N. Chapman, A. A. Bharath, and K. H. Parker, "Retinal vascular tree morphology: a semi-automatic quantification," *Biomedical Engineering, IEEE Transactions on*, vol. 49, no. 8, pp. 912–917, 2002.

[103] V. Bevilacqua, S. Camb, L. Cariello, and G. Mastronardi, "A combined method to detect retinal fundus features," in *European Conference on Emergent Aspects in Clinical Data Analysis*, 2005, pp. 1–6.

[104] T. Chanwimaluang and G. Fan, "An efficient blood vessel detection algorithm for retinal images using local entropy thresholding," in *Circuits and Systems, 2003. ISCAS'03. Proceedings of the 2003 International Symposium on*, vol. 5, 2003, pp. V–21.

[105] E. Ardizzone, R. Pirrone, O. Gambino, and S. Radosta, "Blood vessels and feature points detection on retinal images," in *Engineering in Medicine and Biology Society, 2008. EMBS 2008. 30th Annual International Conference of the IEEE*, 2008, pp. 2246–2249.

[106] C. L. Tsai, C. V. Stewart, H. L. Tanenbaum, and B. Roysam, "Model-based method for improving the accuracy and repeatability of estimating vascular bifurcations and crossovers from retinal fundus images," *Information Technology in Biomedicine, IEEE Transactions on*, vol. 8, no. 2, pp. 122–130, 2004.

[107] E. Jung and K. Hong, "Automatic retinal vasculature structure tracing and vascular landmark extraction from human eye image," in *Hybrid Information Technology, 2006. ICHIT'06. International Conference on*, vol. 2, 2006, pp. 161–167.

[108] A. Bhuiyan, B. Nath, J. Chua, and K. Ramamohanarao, "Automatic detection of vascular bifurcations and crossovers from color retinal fundus images," in *Signal-Image Technologies and Internet-Based System, 2007. SITIS'07. Third International IEEE Conference on*, 2007, pp. 711–718.

[109] A. M. Aibinu, M. I. Iqbal, A. A. Shafie, M. J. E. Salami, and M. Nilsson, "Vascular intersection detection in retina fundus images using a new hybrid approach," *Computers in Biology and Medicine*, vol. 40, no. 1, pp. 81–89, 2010.

[110] D. Calvo, M. Ortega, M. G. Penedo, and J. Rouco, "Automatic detection and characterisation of retinal vessel tree bifurcations and crossovers in eye fundus images," *Computer Methods and Programs in Biomedicine*, vol. 103, no. 1, pp. 28–38, 2011.

[111] G. Azzopardi and N. Petkov, "Automatic detection of vascular bifurcations in segmented retinal images using trainable cosfire filters," *Pattern Recognition Letters*, vol. 34, no. 8, pp. 922–933, 2013.

[112] A. Fathi, A. R. Naghsh-Nilchi, and F. A. Mohammadi, "Automatic vessel network features quantification using local vessel pattern operator," *Computers in Biology and Medicine*, 2013.

[113] B. Al-Diri, A. Hunter, D. Steel, and M. Habib, "Automated analysis of retinal vascular network connectivity," *Computerized Medical Imaging and Graphics*, vol. 34, no. 6, pp. 462–470, 2010.

[114] K. S. Lin, C. L. Tsai, M. Sofka, C. H. Tsai, S. J. Chen, and W. Y. Lin, "Vascular tree construction with anatomical realism for retinal images," in *Bioinformatics and BioEngineering, 2009. BIBE'09. Ninth IEEE International Conference on*, 2009, pp. 313–318.

[115] K. S. Lin, P. Y. Yeh, C. L. Tsai, S. J. Chen, and W. Y. Lin, "Retinal vascular tree construction with multimodal fluorescein angiogram sequence," *Biomedical Engineering: Applications, Basis and Communications*, vol. 22, no. 02, pp. 101–110, 2010.

[116] K.-S. Lin, C.-L. Tsai, C.-H. Tsai, M. Sofka, S.-J. Chen, and W.-Y. Lin, "Retinal vascular tree reconstruction with anatomical realism," *Biomedical Engineering, IEEE Transactions on*, vol. 59, no. 12, pp. 3337–3347, 2012.

[117] K. Rothaus, P. Rhiem, and X. Jiang, "Separation of the retinal vascular graph in arteries and veins," *Graph-Based Representations in Pattern Recognition*, pp. 251–262, 2007.

[118] R. Estrada, M. J. Allingham, P. S. Mettu, S. W. Cousins, C. Tomasi, and S. Farsiu, "Retinal artery-vein classification via topology estimation," *Medical Imaging, IEEE Transactions on*, vol. 34, no. 12, pp. 2518–2534, 2015.

[119] E. Grisan and A. Ruggeri, "A divide et impera strategy for automatic classification of retinal vessels into arteries and veins," in *Engineering in Medicine and Biology Society, 2003. Proceedings of the 25th Annual International Conference of the IEEE*, vol. 1, 2003, pp. 890–893.

[120] L. Tramontan, E. Grisan, and A. Ruggeri, "An improved system for the automatic estimation of the arteriolar-to-venular diameter ratio (AVR) in retinal images," in *Engineering in Medicine and Biology Society, 2008. EMBS 2008. 30th Annual International Conference of the IEEE*, 2008, pp. 3550–3553.

[121] K. Rothaus, X. Jiang, and P. Rhiem, "Separation of the retinal vascular graph in arteries and veins based upon structural knowledge," *Image and Vision Computing*, vol. 27, no. 7, pp. 864–875, 2009.

[122] H.-S. Nam, J.-M. Hwang, H. Chung, and J.-M. Seo, "Automated measurement of retinal vessel diameters on digital fundus photographs," in *World Congress on Medical Physics and Biomedical Engineering, September 7-12, 2009, Munich, Germany*, 2009, pp. 277–280.

[123] L. Tramontan and A. Ruggeri, "Computer estimation of the AVR parameter in diabetic retinopathy," in *World Congress on Medical Physics and Biomedical Engineering, September 7-12, 2009, Munich, Germany*, 2009, pp. 141–144.

[124] V. S. Joshi, M. K. Garvin, J. M. Reinhardt, and M. D. Abràmoff, "Automated artery-venous classification of retinal blood vessels based on structural mapping method," in *Proceedings of SPIE*, vol. 8315, 2012, p. 83151C.

[125] M. Niemeijer, B. van Ginneken, and M. D. Abràmoff, "Automatic classification of retinal vessels into arteries and veins," *Medical imaging*, pp. 72 601F–72 601F, 2009.

[126] ——, "Automatic determination of the artery vein ratio in retinal images," in *SPIE Medical Imaging*. International Society for Optics and Photonics, 2010, pp. 76 240I–76 240I.

[127] C. Muramatsu, Y. Hatanaka, T. Iwase, T. Haraa, and H. Fujita, "Automated detection and classification of major retinal vessels for determination of diameter ratio of arteries and veins," in *Proc SPIE. San Diego, CA, USA*, vol. 7624, 2010, pp. 76 240J–1.

[128] C. Muramatsu, Y. Hatanaka, T. Iwase, T. Hara, and H. Fujita, "Automated selection of major arteries and veins for measurement of arteriolar-to-venular diameter ratio on retinal fundus images," *Computerized Medical Imaging and Graphics*, vol. 35, no. 6, pp. 472–480, 2011.

[129] D. K. Wallace, J. A. Kylstra, and D. A. Chesnutt, "Prognostic significance of vascular dilation and tortuosity insufficient for plus disease in retinopathy of prematurity," *Journal of American Association for Pediatric Ophthalmology and Strabismus*, vol. 4, no. 4, pp. 224–229, 2000.

[130] J. S. Wolffsohn, G. A. Napper, S.-M. Ho, A. Jaworski, and T. L. Pollard, "Improving the description of the retinal vasculature and patient history taking for monitoring systemic hypertension," *Ophthalmic and Physiological Optics*, vol. 21, no. 6, pp. 441–449, 2001.

[131] C. Heneghan, J. Flynn, M. OKeefe, and M. Cahill, "Characterization of changes in blood vessel width and tortuosity in retinopathy of prematurity using image analysis," *Medical Image Analysis*, vol. 6, no. 4, pp. 407–429, 2002.

[132] F. K. Sutter and H. Helbig, "Familial retinal arteriolar tortuosity: a review," *Survey of ophthalmology*, vol. 48, no. 3, pp. 245–255, 2003.

[133] B. Dhillonb, R. H. Eikelboomf, K. Yogesana, and I. J. Constablea, "Retinal image analysis: concepts, applications and potential," *Progress in Retinal and Rye Research*, vol. 25, pp. 99–127, 2006.

[134] J. Parr and G. Spears, "Mathematic relationships between the width of a retinal artery and the widths of its branches," *American Journal of Ophthalmology*, vol. 77, no. 4, pp. 478–483, 1974.

[135] ——, "General caliber of the retinal arteries expressed as the equivalent width of the central retinal artery," *American Journal of Ophthalmology*, vol. 77, no. 4, pp. 472–477, 1974.

[136] C. D. Murray, "The physiological principle of minimum work I. The vascular system and the cost of blood volume," *Proceedings of the National Academy of Sciences*, vol. 12, no. 3, pp. 207–214, 1926.

[137] T. Y. Wong, M. D. Knudtson, R. Klein, B. E. Klein, S. M. Meuer, and L. D. Hubbard, "Computer-assisted measurement of retinal vessel diameters in the Beaver Dam Eye Study: methodology, correlation between eyes, and effect of refractive errors," *Ophthalmology*, vol. 111, no. 6, pp. 1183–1190, 2004.

[138] M. D. Knudtson, K. E. Lee, L. D. Hubbard, T. Y. Wong, R. Klein, and B. E. Klein, "Revised formulas for summarizing retinal vessel diameters," *Current Eye Research*, vol. 27, no. 3, pp. 143–149, 2003.

[139] M. Niemeijer, X. Xu, A. V. Dumitrescu, P. Gupta, B. Van Ginneken, J. C. Folk, and M. D. Abràmoff, "Automated measurement of the arteriolar-to-venular width ratio in digital color fundus photographs," *Medical Imaging, IEEE Transactions on*, vol. 30, no. 11, pp. 1941–1950, 2011.

[140] G. Quellec, S. R. Russell, and M. D. Abràmoff, "Optimal filter framework for automated, instantaneous detection of lesions in retinal images," *Medical Imaging, IEEE Transactions on*, vol. 30, no. 2, pp. 523–533, 2011.

[141] Q. Hu, M. K. Garvin, M. A. Christopher, X. Xu, T. E. Scheetz, and M. D. Abràmoff, "Optimal filter approach for the detection of vessel bifurcations in color fundus images," in *SPIE Medical Imaging*, 2013, p. 866920C866920.

[142] I. Jolliffe, *Principal Component Analysis*. Wiley Online Library, 2002.

[143] A. W. Whitney, "A direct method of nonparametric measurement selection," *Computers, IEEE Transactions on*, vol. 100, no. 9, pp. 1100–1103, 1971.

[144] S. Lee, J. M. Reinhardt, P. C. Cattin, and M. D. Abràmoff, "Objective and expert-independent validation of retinal image registration algorithms by a projective imaging distortion model," *Medical Image Analysis*, vol. 14, no. 4, pp. 539–549, 2010.

[145] D. M. Mount and S. Arya, "ANN: a library for approximate nearest neighbor searching," in *CGC 2nd Annual Fall Workshop on Computational Geometry*, 1997.

[146] Q. Hu, M. D. Abràmoff, and M. K. Garvin, "Automated separation of binary overlapping trees in low-contrast color retinal images," in *Medical Image Computing and Computer-Assisted Intervention–MICCAI 2013*. Springer, 2013, pp. 436–443.

[147] ——, "Automated construction of arterial and venous trees in retinal images," *Journal of Medical Imaging*, vol. 2, no. 4, pp. 044 001–044 001, 2015.

[148] L. Lam, S.-W. Lee, and C. Y. Suen, "Thinning methodologies-a comprehensive survey," *Pattern Analysis and Machine Intelligence, IEEE Transactions on*, vol. 14, no. 9, pp. 869–885, 1992.

[149] M. Niemeijer, M. Abràmoff, and B. Van Ginneken, "Automated localization of the optic disc and the fovea," in *Engineering in Medicine and Biology Society, 2008. EMBS 2008. 30th Annual International Conference of the IEEE*. IEEE, 2008, pp. 3538–3541.

[150] V. Joshi, J. M. Reinhardt, and M. D. Abràmoff, "Automated measurement of retinal blood vessel tortuosity," in *Proc SPIE Medical Imaging*, vol. 7624, 2010, p. 76243A.

[151] T. Kavitha, C. Liebchen, K. Mehlhorn, D. Michail, R. Rizzi, T. Ueckerdt, and K. A. Zweig, "Cycle bases in graphs characterization, algorithms, complexity, and applications," *Computer Science Review*, vol. 3, no. 4, pp. 199–243, 2009.

[152] X. Xu, M. Niemeijer, Q. Song, M. Sonka, M. K. Garvin, J. M. Reinhardt, and M. D. Abràmoff, "Vessel boundary delineation on fundus images using graph-based approach," *Medical Imaging, IEEE Transactions on*, vol. 30, no. 6, pp. 1184–1191, 2011.

[153] B. Dashtbozorg, A. M. Mendonça, and A. Campilho, "An automatic graph-based approach for artery/vein classification in retinal images," *Image Processing, IEEE Transactions on*, vol. 23, no. 3, pp. 1073–1083, 2014.

[154] J. Schouten, F. W. Wit, I. G. Stolte, N. Kootstra, M. van der Valk, S. G. Geerlings, M. Prins, P. Reiss, P. Reiss, F. Wit *et al.*, "Cross-sectional comparison of the prevalence of age-associated comorbidities and their risk factors between HIV-infected and uninfected individuals: the AGEhIV cohort study," *Clinical Infectious Diseases*, p. ciu701, 2014.